Die approbierte Originalversion dieser Diplom-/Masterarbeit ist in der Hauptbibliothek der Technischen Universität Wien aufgestellt und zugänglich.
http://www.ub.tuwien.ac.at

The approved original version of this diploma or master thesis is available at the main library of the Vienna University of Technology.
http://www.ub.tuwien.ac.at/eng

TECHNISCHE UNIVERSITÄT WIEN
Vienna University of Technology

Diplomarbeit

Optics Design and Performance Aspects of the HE-LHC

ausgeführt am
Atominstitut der TU Wien

in Zusammenarbeit mit
CERN

unter Betreuung von
Privatdoz. Dipl.Ing. Dr.techn. Michael Benedikt

und
Dr. Rogelio Tomás (CERN)

durch
Jacqueline Keintzel, BSc
Matr. Num.: 01325138
Sportplatzstrasse 9
A-2151 Asparn an der Zaya

Wien, August 2018

Declaration

I declare that I have developed and written this thesis completely by myself, and have not used sources or means without declaration in the text. Any thoughts from others or literal quotations are clearly marked. This thesis was not used, in whole or in part, to achieve an academic degree.

Vienna, August 2018

Jacqueline Keintzel

Abstract

The optics design of the High Energy Large Hadron Collider (HE-LHC), a possible successor of the High Luminosity Large Hadron Collider (HL-LHC) which aims to reach a centre of mass energy of about 27 TeV, requires a trade off between energy reach, beam stay clear and geometry. In this thesis various designs are studied for the two counter rotating proton beams in order to fulfill best the requirements. Aperture bottlenecks are identified and solutions are proposed.
Quadrupole errors present in the arc dipoles and their effect at collision energy are studied. At injection energy combined function arc dipoles and their effect on the beam stay clear is explored.
First estimates regarding HE-LHC performance during collision are given. Operational scenarios using different β^* levelling techniques are used in order to keep the pile-up constant are proposed and compared. A scenario with a constant divergence is proposed.

Kurzfassung

Der High Energy Large Hadron Collider (HE-LHC), welcher eine Schwerpunktsenergie von ungefähr 27 TeV anstrebt, ist ein möglicher Nachfolger des Large Hadron Colliders (LHC). Das Design dieses Zukunftsbeschleunigers stellt einen Kompromiss aus erreichbarer Energie, Apertur sowie Geometrie dar. Sowohl die Optik als auch die Apertur für die zwei entgegengesetzt rotierenden Protonenstrahlen werdens in dieser Arbeit diskutiert. Des Weiteren werden die Schwachstellen der Apertur aufgezeigt und Maßnahmen zur Verbesserung vorgeschlagen.
Der Effekt unvermeidbarer Quadrupolfehler in den Dipolen bei Kollisionsenergie wird behandelt. Auch die Verwendung von Dipolen mit integrierten Quadrupolfeldern und deren Effekt auf die Apertur bei Injektionsenergie werden thematisiert. Resultate erster Simulationen des Kollisionsbetriebes werden analysiert. Mehrere alternative β^*-levelling Szenarien werden vorgestellt und verglichen. Außerdem wird ein Szenario mit konstanter Divergenz analysiert.

Acknowledgements

Since high school it has always been my dream to get the chance to work in the field of accelerator physics at CERN. Today I want to thank those, who accompanied me on my journey to make my dream come true.

At the beginning I would really like to thank my university supervisor, Michael Benedikt. Thank you for your support and for establishing the contact with my CERN supervisor and therefore, making this thesis possible.

Particular thanks deserves my CERN supervisor Rogelio Tomás. Thank you for sharing your great knowledge with me and for always answering my questions, even though your daily schedule is busy. I really appreciate your help for all the intriguing challenges you impose on me.

Moreover, I have the great pleasure to work with my fellows and friends, Michael Hofer and Leon van Riesen-Haupt. Thank you for your immediate support, especially during my first weeks. I could not fight the war against MAD-X without you.

I fell in love with physics in high school, due to a great teacher. Therefore, not negligible impact on my professional career and personal development had my former teachers, Martin Sommer and Claudia Hermann. Thank you for your ongoing support. Martin, you can now tell your students: Es geht auch nach vier.

Besonderer Dank gebührt noch meinen Freunden und meiner Familie, die mich stets begleitet und unterstützt haben. Insbesondere bedanke ich mich bei meinen Eltern, sowie Großeltern, die immer für mich da sind. Obwohl uns seit Monaten einige hundert Kilometer trennen, müsst ihr wissen dass ich stets an euch denke und ich weiß, ihr auch an mich. Vielen Dank für alles!

Abschließend möchte ich mich noch bei meinem Freund Michael Bacak bedanken. Danke für deine Unterstützung und dein Verständnis, während der vergangenen Wochen. Danke, dass du die Nerven behalten hast, als ich sie schon längst weg geworfen habe. Vielen Dank!

Abbreviations

ALGEA Automatic Lattice Generation Application

ALICE A Large Ion Collide Experiment

ATLAS A Toroidal LHC Apparatus

ATS Achromatic Telescopic Squeezing

BSC Beam Stay Clear

CERN European Organisation for Nuclear Research

CMS Compact Muon Solenoid

C.O.M. Centre Of Mass

DS Dispersion Suppressor

FCC Future Circular Collider

FCC-ee Lepton Future Circular Collider

FCC-hh Hadron Future Circular Collider

FCC-he Hadron-Lepton Future Circular Collider

FODO Structure of Focusing and Defocusing Quadrupole

HE-LHC High Energy Large Hadron Collider

HL-LHC High Luminosity Large Hadron Collider

IBS Intrabeam Scattering

IP Interaction Point

IR Interaction Region

KEK High Energy Accelerator Research Organisation

LEP Large Electron Positron Collidier

LHC Large Hadron Collider

LHCb Large Hadron Collider Beauty Experiment

MAD-X Methodical Accelerator Design Version 10

MB Dipole Magnet

MCB Dipole Corrector

MCD Decapole Field Corrector

MCO Octupole Field Corrector

MCS Sextupole Field Corrector

MO Octupole Magnet

MQ Quadrupole Magnet

MQT Trim Quadrupole Magnet

MS Sextupole Magnet

PS Proton Synchrotron

RF Radio Frequency

RMS Root Mean Square

SPS Super Proton Synchrotron

"Make it work. Make it right. Make it fast."

Kent Beck

Contents

1 Motivation **1**

2 Introduction **3**
2.1 High Energy Physics Status . . . 3
2.2 Future Circular Collider Study . . . 4
2.2.1 HE-LHC . . . 4
2.2.2 FCC-hh . . . 5
2.2.3 FCC-he . . . 5
2.2.4 FCC-ee . . . 5

3 Theory **7**
3.1 Introduction to Accelerator Physics . . . 7
3.1.1 Coordinate System . . . 8
3.1.2 Basic Structures . . . 8
3.1.3 Formalism . . . 11
3.1.4 Transverse Dynamics . . . 13
3.1.5 Longitudinal Dynamics . . . 17
3.2 Performance Aspects . . . 19
3.3 Aperture . . . 25
3.4 Lattice Structures . . . 27
3.4.1 FODO Cells . . . 27
3.4.2 Arcs . . . 27
3.4.3 Insertions . . . 27
3.4.4 Dispersion Suppressor . . . 27
3.5 The LHC . . . 29
3.5.1 LHC FODO Cell . . . 30
3.5.2 LHC Arcs . . . 30
3.5.3 LHC Insertions . . . 31
3.5.4 LHC Dispersion Suppressor . . . 31
3.5.5 LHC Parameters . . . 32
3.6 Main Dipole Errors . . . 33
3.7 MAD-X . . . 34

4 ALGEA **37**
4.1 Motivation . . . 37
4.2 Constraints and Parameters . . . 37

4.3 Dispersion Suppressor Options 39
4.4 Survey Fitting 42
4.5 Output 44

5 HE-LHC Design **45**
5.1 Lattice Options 45
5.1.1 Aperture 46
5.1.2 Energy Reach 47
5.1.3 Geometry 47
5.2 Baseline Lattices 49

6 Studies at Injection Energy **55**
6.1 Aperture of the Ring 55
6.2 Aperture Dependence on Phase Advance 58
6.3 Combined Function Dipoles 60
6.4 Combined Function Dipoles at Optimal Phase Advance 62

7 Studies at Collision Energy **65**
7.1 Effect of Quadrupole Errors 65
7.2 Correction of Quadrupole Errors 67

8 Performance **69**
8.1 Baseline 69
8.2 β^* Levelling 71
8.2.1 Dependence on Levelling Step 74
8.2.2 Dependence on Penalty Step 75
8.3 β^* Levelling using ATS 76
8.4 Constant Divergence 78

9 Conclusion **81**

A Interaction Region Optics **83**

List of Figures **89**

List of Tables **91**

Bibliography **93**

Chapter 1

Motivation

In the field of high energy physics the Large Hadron Collider (LHC) [1] at CERN (European Organisation for Nuclear Research) [2] is the leading particle accelerator regarding energy reach and rate of hadron particle collisions in the world. It will be followed by the High Luminosity LHC (HL-LHC) [3], an approved upgrade of the LHC, which achieves a 5 times higher instantaneous luminosity compared to the LHC.

Studies of possible future linear [4, 5] or circular [6] accelerators are ongoing. One possible future circular collider is the High Energy LHC (HE-LHC). As it is the case in the LHC, the HE-LHC has two counter rotating and colliding proton beams. Moreover, this synchrotron would be built in the already existing tunnel after the decommissioning of the HL-LHC. The possible commissioning of the HE-LHC is scheduled around 2040 [7]. As the HE-LHC achieves an approximately 2 times higher centre of mass energy, as well as a 3 times higher instantaneous luminosity than the HL-LHC, this future accelerator has the potential to explore new physics at an unprecedented energy frontier [8].

Even though the HE-LHC layout is similar to the LHC [9, 10] it is not possible to simply rescale the LHC as for example, the HE-LHC achieves its target energy only with stronger dipoles (16 T instead of 8.3 T) which require longer separation distances between them. Therefore different HE-LHC arc and dispersion suppressor designs are explored while taking into account constraints like the tunnel geometry, magnet fields, separation distances and reachable energy. New interaction regions are also designed to meet the HE-LHC requirements, which are then integrated into the lattice. The arcs, and especially the dispersion suppressor, need to be designed in order to integrate the interaction region optics.

In addition to the minimum separation distance between the dipoles, a specific beam screen design is required for the HE-LHC. This beam screen then has an effect on the beam stay clear. Studies to reach sufficient beam stay clear while considering all element contraints are indispensable to a stable beam and are therefore presented in this thesis. Aperture bottlenecks for both beams need to be identified.

Unavoidable magnet errors in the arc dipoles also need to be considered, as they affect the performance. For example, quadrupole errors are mainly present at collision energy, which can lead to a decreased centre of mass energy.

The performance of two proposed HE-LHC lattices are studied. In addition, alternative scenarios are tested in order to ensure constant luminosity or divergence during the physics fill by reducing the β^*.

The chapters have the following contents:

2 An introduction to the LHC and the FCC study is given.

3 An introduction to accelerator and beam physics is given.

4 In order to eficiently explore different lattice options a new tool named *ALGEA*[1] (Automatic Lattice GEneration Application) is developed and presented.

5 Different arc cell and dispersion suppressor options are presented, before concluding on two baseline lattices.

6 The effect of phase advance on the beam stay clear is given. Moreover, the use of combined function dipoles is analysed.

7 The effects of no-negligible quadrupole errors in the arc dipoles at collision energy are studied.

8 First estimations on a variety of performance aspects are given for the baseline operation scenario as well as for alternative scenarios, where the instantaneous luminosity or the divergence is constant.

9 This thesis closes with a summary of the results and mentions future perspectives.

[1] In greek mythology the Algea were the personified spirits (daimones) of pain and suffering body and mind, grief, sorrow and distress. They were the bringers of weeping and tears [11].

Chapter 2

Introduction

A brief overview of the LHC is given. Then, the ongoing study about future circular accelerators is introduced.

2.1 High Energy Physics Status

CERN is the largest research centre for particle physics in the world, where hadrons, predominantly protons, are accelerated and collided in order to understand the structure of the universe. In Figure 2.1 the accelerator complex at CERN is shown schematically. The protons are accelerated by a chain of accelerators where the final energy is reached in the LHC. The proton beams are injected into the LHC synchrotron from the Super Proton Synchrotron (SPS) [13] with 450 GeV per beam. The beams are then accelerated up to 6.5 TeV per beam [14]. At top energy the two

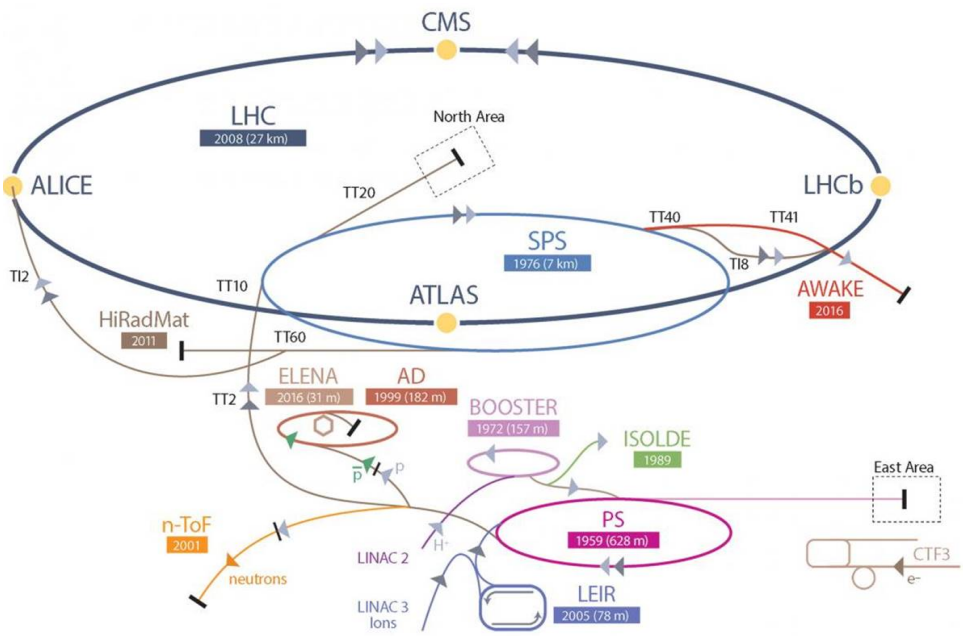

FIGURE 2.1: CERN complex and accelerator chain, adapted from [12].

counter rotating beams collide at four points. The instantaneous luminosity, an indicator for the number particle of collisions, reaches above $1 \times 10^{34}\,\mathrm{cm}^{-2}\mathrm{s}^{-1}$, which is unique for hadron colliders. However, the lepton collider SUPERKEKB [15] at KEK [16] is designed to achieve an instantaneous luminosity of about 1 to $5 \times 10^{34}\,\mathrm{cm}^{-2}\mathrm{s}^{-1}$ [17].

2.2 Future Circular Collider Study

Possible Future Circular Colliders (FCC) are explored in an ongoing study [6] under the leadership of CERN. Three approaches are considered, namely to collide two lepton beams (FCC-ee), two hadron beams (FCC-hh or HE-LHC) or one hadron and one lepton beam (FCC-he). The last option can be performed simultaneously with one of the hadron options.

In Figure 2.2 a schematic plot of the FCC tunnel as well as the (HE-)LHC tunnel is given. The tunnel for the FCC will be 80 km to 100 km long. In the following the different colliders are explained. The latest FCC-hh, HE-LHC parameters are summarised in Table 2.1.

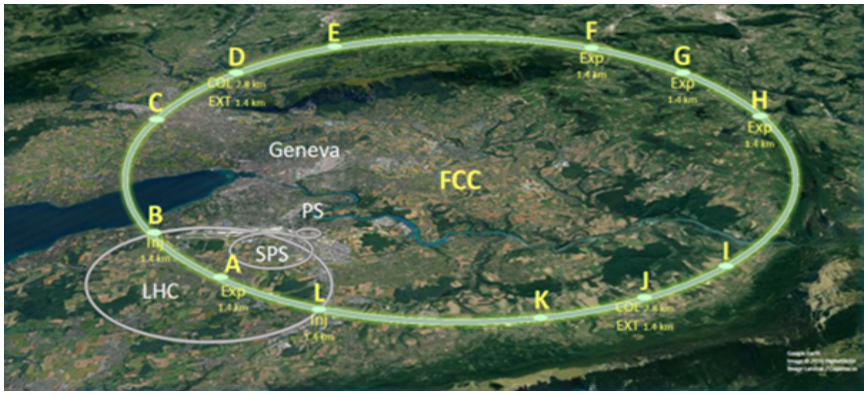

FIGURE 2.2: Schematic drawing of the HE-LHC and FCC [18].

2.2.1 HE-LHC

The HE-LHC collides two counter rotating proton beams in the existing tunnel which already hosted the Large Electron Positron (LEP) collider as well as the LHC [19, 20]. Building this collider in the existing tunnel does not foresee any major civil engineering work which is a big advantage. Moreover a new 16 T dipole design, required to meet the target energy of about 27 TeV are specially designed for the FCC-hh are used for the HE-LHC as well.

2.2.2 FCC-hh

The current FCC-hh design foresees a circumference of about 100 km. It would be the largest and the most powerful particle accelerator ever built. To accelerate two counter rotating proton beams up to 50 TeV per beam 16 T dipoles are used. The conceptual design is shown in Figure 2.3. The main experiments are located in interaction regions (IR) A and IRG [21]. In IRB and IRL the two counter rotating hadron beams are injected. The beam dump is located in IRD [22]. Collimation takes place in IRF and IRJ [23, 24].

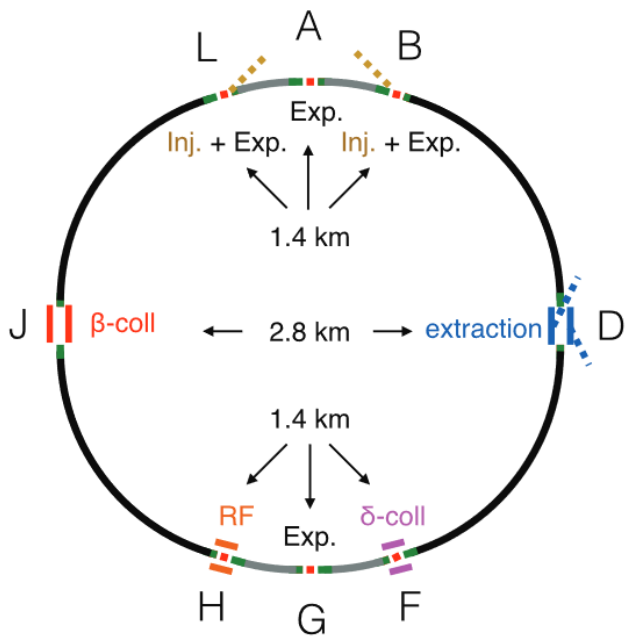

FIGURE 2.3: Schematic layout of the FCC-hh [25].

2.2.3 FCC-he

One of the interaction regions of the FCC-hh could be used to perform proton electron collisions (FCC-he). In this interaction region one proton beam with about 50 TeV can be collided with a 60 GeV electron beam coming from a linear accelerator [29].

2.2.4 FCC-ee

The FCC-ee collides two lepton beams. Lepton circular acceleratos have a smaller centre of mass energy compared to hadrons due to energy losses for synchrotron radiation. Nevertheless this lepton collider can perform experiments with high precision. Moreover the FCC-ee tunnel is designed to be compatible with the FCC-hh as a successor in it.

Parameter	Unit	FCC-hh	HE-LHC	(HL-)LHC
Centre of Mass Energy	TeV	100	27	14
Arc Dipole Field	T	16	16	8.3
Circumference	km	97.8	26.7	26.7
Number of IPs	–	2+2	2+2	2+2
Bunch Population	10^{11}	1.0	2.2	(2.2) 1.15
RF Voltage	MV	24	16	16
Bunch Length	mm	80	75.5	75.5
Momentum Spread	10^{-4}	0.3	0.85	1.129
Longitudinal Emittance	eVs	5	4.2	2.5
Bunch Spacing	ns	25	25	25
Normalised Emittance	µm	2.2	2.5	(2.5) 3.75
β^*	m	0.3	0.45	(0.15) 0.55
Half Crossing Angle	µrad	70	165	(250) 150
Peak Luminosity	$10^{34}\,\mathrm{cm}^{-2}\,\mathrm{s}^{-1}$	30	15	(5, levelled) 1
Luminosity per Year	fb^{-1}	1000	500	(262) 55
Total Cross Section	mb	153	126	111
Inelastic Cross Section	mb	108	91	85
Pile-Up	–	1000	430	(135) 27
Optimum Run Time	h	3.6	5.3	(11.7) 14.2
Turn Around Time	h	4.0	5.0	(4.0) 5.0
Accelerator Availability	%	70	75	(52) 71

TABLE 2.1: FCC-hh, HE-LHC, HL-LHC and LHC key parameters at collision energy [26, 27, 28].

Chapter 3

Theory

The theoretical background relevant for this thesis is introduced in this chapter, starting with accelerator and beam physics. The different structures of an accelerator like the HE-LHC are then explained. Moreover relevant performance aspects are discussed. Lastly arc dipole errors and their sources are explained.

3.1 Introduction to Accelerator Physics

Since accelerator science started in the 20th century, various types of particle accelerators have been developed. The underlying principle is the interaction between charged particles and electromagnetic fields via the Lorentz force $\vec{F}$

$$\vec{F} \;=\; \frac{d\vec{p}}{dt} \;=\; q\,(\vec{E} + \vec{v} \times \vec{B})\,, \tag{3.1}$$

where $\vec{p}$ is the particle momentum, q the particle charge, $\vec{E}$ the electrical field, $\vec{v}$ the particle velocity and $\vec{B}$ the magnetic flux density.

The magnetic field guides the charged particle onto circular paths. In case of circular accelerator the magnetic flux density is perpendicular to the velocity and one can define the *beam rigidity* $B\rho$

$$B\rho\,[\mathrm{Tm}] \;=\; \frac{p}{|q|} \;=\; \frac{A}{Z} \times 3.33564 \times p\,[\mathrm{GeV/c/u}]\,, \tag{3.2}$$

where A is the atomic mass number, Z the nuclear charge number, c the velocity of light, q the particle charge and p the particle momentum which is measured in units of GeV/c per atomic unit u.

The electric field is responsible for accelerating the beam. The energy gain or loss is the path integral of the Lorentz force and can be therefore calculated using

$$\Delta E \;=\; \int_{s_1}^{s_2} \vec{F}\,\mathrm{d}\vec{s} \;=\; \int_{s_1}^{s_2} q\,(\vec{E} + \vec{v} \times \vec{B})\,\mathrm{d}\vec{s} \;=\; \int_{s_1}^{s_2} q\,\vec{E}\,\mathrm{d}\vec{s}\,. \tag{3.3}$$

The integral over the vector product is zero as the path element $d\vec{s}$ is parallel to the velocity and is therefore not usable for acceleration.

3.1.1 Coordinate System

In sychrotrons the orthogonal Frenet-Serret coordinate system [30] is taken as a reference. It is illustrated in Figure 3.1. It travels along with the particle and has the coordinates (x, y, s), where s is tangential to the reference orbit. x is defined in the horizontal plane and y in the vertical plane.

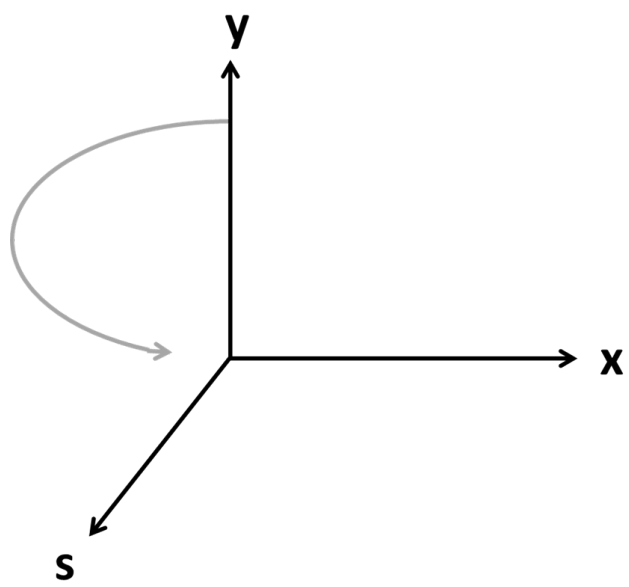

FIGURE 3.1: Transverse coordinate system for linear optics.

3.1.2 Basic Structures

Guiding and focusing structures make up the majority of a synchrotron like the HE-LHC. These structures are basically magnets of different multipole order which work as magnetic lenses and therefore can be associated with an optics. This will be explained in detail later in this section. Dipoles and quadrupoles are linear elements. Higher order magnets are non-linear.

LATTICE

The term *lattice* describes the arrangement of all used elements in an accelerator. A linear lattice is an arrangement of linear elements only. Dipoles and quadrupoles are linear elements.

Drift Space

Particles in an accelerator do not always travel from one element directly to another one continuously. In a lattice there are empty spaces in between elements which are named *drift spaces*. These drift spaces are ideally field free.

Dipole

Dipoles are used to guide the particles along a desired orbit, mostly in the horizontal plane. As they bend the beam they are also named *bending magnets* with the abbreviation *MB*. All dipoles which are not located in the interaction region (see Section 3.4.3) are named *main dipoles*. An ideal dipole field is illustrated in the left plot of Figure 3.2. The bending angle θ of one dipole in a circular collider can be calculated as

$$\theta = \frac{2\pi}{N_{MB}}, \tag{3.4}$$

where N_{MB} refers to the number of main dipoles in the whole accelerator, assuming identical main dipoles over the whole ring. Moreover the dipoles define the reachable centre of mass (c.o.m.) energy, expressed through

$$B\rho = \frac{B\,L}{\theta}, \qquad B\rho = \frac{p}{q}, \tag{3.5}$$

with the magnetic rigidity $B\rho$, dipole length L, the magnetic field B, provided by one dipole, the bending radius per dipole ρ, the particle momentum p and the particle charge q.

Although dipoles are mainly used as guiding elements they have a focusing effect

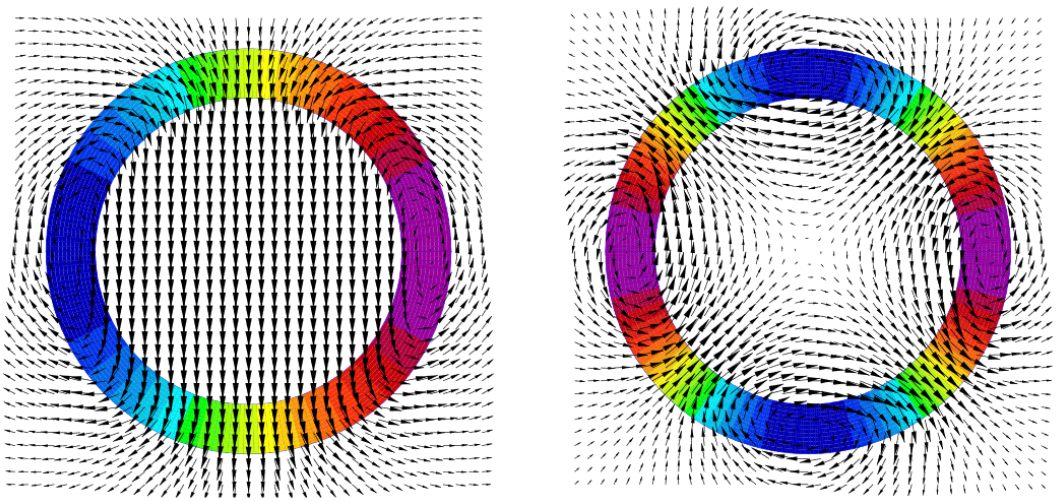

FIGURE 3.2: Visualisation of an ideal dipole (left) and quadrupole (right) field [31].

as well. For example, in betatrons [32] the particles are focused using only a dipole field. Machines which rely only on dipoles as focusing structures are named *weak focusing* machines. Even though the effect of weak focusing is quite small in synchrotrons like the (HE-)LHC it is still present.

QUADRUPOLE

A *quadrupole* is constructed of four symmetric aligned poles to generate a field illustrated in the right plot of Figure 3.2. The abbreviation *MQ* refers to *main quadrupole*, located in the arcs. The magnetic field of an ideal quadrupole is given by

$$\vec{B} = B_1(y\hat{x} + x\hat{y}) , \tag{3.6}$$

where B_1 is

$$B_1 = \frac{\partial B_y}{\partial x} . \tag{3.7}$$

The centre of a quadrupole is field free, therefore a particle passing through the desired orbit located exactly in the middle of the quadrupole is not affected by the quadrupole at all. Particles travelling away from this reference orbit however, are focused transversely by quadrupoles.

A quadrupole is used as a focusing structure in an accelerator. Due to the symmetric alignment of the poles it is either focusing horizontally or vertically, while defocusing in the perpendicular transverse plane. A *focusing quadrupole* always referes to a horizontally focusing quadrupole. Synchrotrons are made of an alternating focusing and defocusing quadrupoles scheme. An accelerator which uses quadrupoles for focusing is named an *alternating gradient* or *strong focusing* machine. This alternating gradient scheme induces oscillations in the transverse planes, which strongly depend on the quadrupole distribution. The number of oscillations over the whole ring is named *tune (Q)*.

Particles cannot only be off-orbit but off-momentum too. Higher momentum particles feature a larger focal length, and so the focusing effect is weaker with respect to particles with lower momentum.

SEXTUPOLE

Particles with a higher momentum than the reference particle are focused by a quadrupole with a longer focal length. A *sextupole MS* corrects this chromatic effects. The sextupole field can be described with [33]

$$B_y = \frac{B_2}{2}(x^2 - y^2) , \qquad B_x = B_2 xy , \tag{3.8}$$

where B_2 is

$$B_2 = \frac{\partial^2 B_y}{\partial x^2} . \tag{3.9}$$

CORRECTOR

In a realistic accelerator lattice errors are present due to, for example, element misalignments or field errors. To operate a machine these errors have to be corrected. Different types of errors require different correctors. Therefore the term corrector refers more to an element family than to one specific element:

- MCBH (MCBV): These are horizontal (vertical) dipole corrector magnets. Using a dipolar field they kick the beam for orbit corrections. Orbit correctors are also used to induce orbit bumps [34].
- MCS: These sextupoles correct sextupolar field errors in the main dipoles.
- MCO (MCD): These octupoles (decapoles) correct octupolar (decapolar) field errors in the main dipoles.

3.1.3 Formalism

Even though a realistic accelerator is not a linear lattice it is usual to consider only ideal dipoles and quadrupoles as a first approximation. This leads to an uncoupled particle motion in the horizontal and vertical planes.

FIELD EXPANSION

The magnetic field close to the design orbit can be expanded as

$$\begin{aligned} \frac{q}{p} B_y(x) &= \frac{q}{p} \sum_{n=0}^{\infty} \frac{1}{n!} \frac{\mathrm{d}^{(n)} B_y}{\mathrm{d}x^n} x^n \\ &= \frac{q}{p} B_y + \frac{q}{p} \frac{\mathrm{d}B_y}{\mathrm{d}x} x + \frac{q}{p} \frac{1}{2!} \frac{\mathrm{d}^2 B_y}{\mathrm{d}x^2} x^2 + \ldots \\ &= \frac{1}{\rho} + k_1 x + \frac{1}{2!} k_2 x^2 + \ldots \end{aligned} \tag{3.10}$$

The first term $(1/\rho)$ refers to a dipolar field, the second $(k_1 x)$ to a quadrupolar field and the third $(k_2 x^2/2)$ to a sextupolar field.

HILL'S EQUATION

Transverse particle motion follows *betatron oscillations* and can be described using *Hill's differential equation*

$$z''(s) + K_z\, z(s) = 0 , \tag{3.11}$$

where z is a placeholder for the x or y coordinate of a given particle. Betatron oscillations are observed in the horizontal (x) as well as in the vertical (y) planes.

The focusing strength K is different for the two transverse planes as the effect of weak focusing is not present in the vertical plane:

$$\begin{aligned} K_x &= \left(\frac{1}{\rho^2} - k_1\right), \\ K_y &= k_1 . \end{aligned} \tag{3.12}$$

The different sign of the quadrupole strength k_1 reflects that if a quadrupole is focusing in one plane it is defocusing in the perpendicular tranverse plane.

A general solution of Hill's equation is given as

$$\begin{pmatrix} z \\ z' \end{pmatrix}_s = M \begin{pmatrix} z \\ z' \end{pmatrix}_0 , \quad \text{with} \quad M = \begin{pmatrix} C & S \\ C' & S' \end{pmatrix} , \tag{3.13}$$

where the index 0 refers to the initial conditions and the index s to the coordinates after passing through an element or drift space with length s. The transfer matrix M depends on the element itself. These transfer matrices for a focusing ($M_{focusingMQ}$) or defocusing ($M_{defocusingMQ}$) quadrupole, a dipole (M_{MB}) and a drift space (M_{drift}) are summarised here, where the bending angle θ and the bending radius ρ are correlated through

$$\theta = \frac{s}{\rho} , \tag{3.14}$$

$$M_{focusingMQ} = \begin{pmatrix} \cos(\sqrt{K}s) & \frac{1}{\sqrt{K}} \sin(\sqrt{K}s) \\ -\sqrt{K} \sin(\sqrt{K}s) & \cos(\sqrt{K}s) \end{pmatrix} , \tag{3.15}$$

$$M_{defocusingMQ} = \begin{pmatrix} \cosh(\sqrt{|K|}s) & \frac{1}{\sqrt{|K|}} \sinh(\sqrt{|K|}s) \\ \sqrt{|K|} \sinh(\sqrt{|K|}s) & \cosh(\sqrt{|K|}s) \end{pmatrix} , \tag{3.16}$$

$$M_{MB} = \begin{pmatrix} \cos(\theta) & \rho \sin(\theta) \\ -\frac{1}{\rho} \sin(\theta) & \cos(\theta) \end{pmatrix} , \tag{3.17}$$

$$M_{drift} = \begin{pmatrix} 1 & s \\ 0 & 1 \end{pmatrix} . \tag{3.18}$$

The particle motion through a linear lattice can be calculated analytically by multiplying the transfer matrices depending on the lattice structure.

COURANT-SNYDER PARAMETRISATION

For periodic lattices there is a convenient way to parameterise the particle trajectories, which was developed by Courant and Snyder [35]. In that case the transfer matrix can be expressed as:

$$M = \begin{pmatrix} \cos(\phi) + \alpha \sin(\phi) & \beta \sin(\phi) \\ -\gamma \sin(\phi) & \cos(\phi) - \alpha \sin(\phi) \end{pmatrix} . \tag{3.19}$$

The Courant-Snyder-parameters α, β and γ are functions of the coordinate s. They are also called *twiss parameters*. ϕ is referred as the *phase advance*. These parameters are defined for both the horizontal and the vertical plane. The parameters α, γ and ϕ are related to the β-function:

$$\alpha(s) = -\frac{1}{2}\beta'(s) , \qquad \gamma(s) = \frac{1+\alpha^2(s)}{\beta(s)} , \qquad \phi = \int_{s_1}^{s_2} \frac{ds}{\beta(s)} . \tag{3.20}$$

For a stable particle motion

$$|trace(M)| \leq 2 \tag{3.21}$$

has to be valid. The Courant-Snyder parameters transform from one point s_1 to another point s_2 through

$$\begin{pmatrix} \beta \\ \alpha \\ \gamma \end{pmatrix}_{s_2} = \begin{pmatrix} C^2 & -2SC & S^2 \\ -CC' & SC' + S'C & -SS' \\ C'^2 & -2S'C' & S'^2 \end{pmatrix} \begin{pmatrix} \beta \\ \alpha \\ \gamma \end{pmatrix}_{s_1} . \tag{3.22}$$

C, C', S and S' are the coefficients of the transport matrix M (see equation (3.13)).

3.1.4 Transverse Dynamics

In the previous subsections the main elements for particle guiding, focusing and correction, as well as the courant-snyder (or twiss) parameters are introduced. These parameters are optical functions used to describe particle motions in accelerators in both transverse planes.

Betatron Oscillations

Using the courant-snyder-parametrisation the solution of Hills' equation (3.11) can be expressed as follows:

$$\begin{aligned} z(s) &= \sqrt{\epsilon\beta(s)}\cos(\phi(s)-\delta)\,, \\ z'(s) &= -\sqrt{\frac{\epsilon}{\beta(s)}}\Big(\sin(\phi(s)-\delta)+\alpha(s)\cos(\phi(s)-\delta)\Big)\,. \end{aligned} \tag{3.23}$$

ϵ and δ are constants of the particle trajectory. The beta function $\beta(s)$ can be understood as the position dependent amplitude of the oscillation of a particle in the transverse planes (x and y) and has the dimension of metres. It is therefore named *amplitude function* as well. In a realistic accelerator the beta function has small deviaitons $\Delta\beta$ from the design value. This is named *beta beating* or $\frac{\Delta\beta}{\beta}$. The beta function at the collision point is named β^*.

Emittance

Combining equations (3.23) leads to

$$\gamma(s)z^2 + 2\alpha(s)zz' + \beta(s)z'^2 = \epsilon_{SP}\,, \tag{3.24}$$

which is also known as the *single particle emittance* (ϵ_{SP}). A schematic plot of the

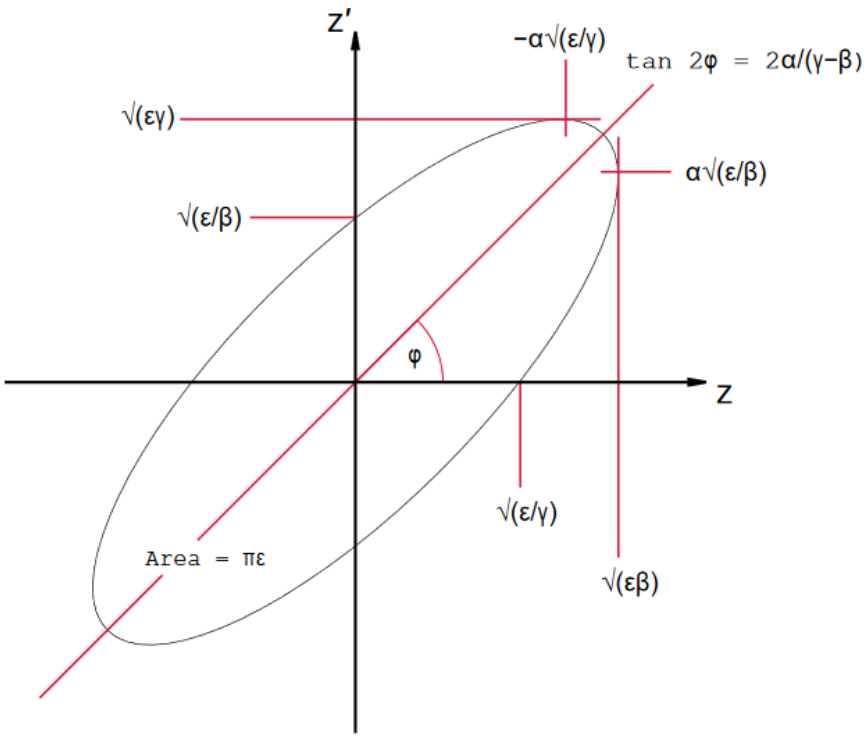

FIGURE 3.3: Phase space ellipse showing the emittance [36].

phase space ellipse is shown in Figure 3.3. The emittance defines the area of the phase space ellipse.

Liouville's theorem states that the phase space area remains constant along the beam line. However, this is only true for a closed system. Charged particles travelling on a curved path emit synchrotron radiation and therefore a storage ring is not a closed system.

One can define the *normalised emittance* ϵ_n

$$\epsilon_n = \beta_{rel}\gamma_{rel}\,\epsilon\,, \tag{3.25}$$

which remains constant during the acceleration and neglecting synchrotron radiation, where β_{rel} and γ_{rel} are the relativisitc Lorentz factors. The actual beam size, or root mean square (RMS) is defined as

$$\sigma = \sqrt{\epsilon\,\beta(s)}\,, \tag{3.26}$$

with the *beam emittance* ϵ. It is defined as the emittance corresponding to an amplitude of $1\,\sigma$ of the gaussian charge distribution.

Closed Orbit

Particles are designed to travel along the *design orbit*. In realistic accelerators however, particles follow not exact these orbit, but another closed path. This, the actual orbit, is named the *closed orbit*. In Figure 3.4 an illustration of the design and the closed orbit is shown.

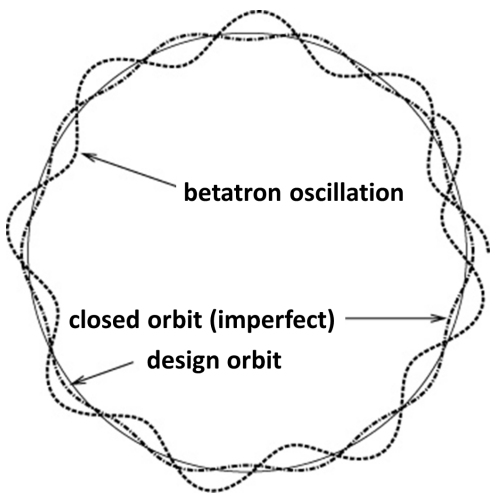

FIGURE 3.4: Schematic plot of the design orbit, closed orbit and betatron oscillation, adapted from [37].

Betatron Tune

Hill's differential equation (3.11) describes transverse particle oscillations which are named betatron oscillations. The *betatron tune*, or simply *tune* (Q) is the number of betatron oscillations over one revolution with circumference C and can be calculated using

$$Q = \frac{1}{2\pi} \int_0^C \frac{ds}{\beta(s)} \,. \tag{3.27}$$

A schematic plot of the ideal orbit, the closed orbit and the betatron oscillations is given in Figure 3.4.

As there is a horizontal tune (Q_x) and a vertical tune (Q_y), the *working point* of a machine can be defined as the pair (Q_x, Q_y). In circular accelerators particles pass through the same element every turn. Due to magnetic imperfections this can lead to a resonance effect and further to excitation of the beam. The working point has to be chosen in a way to avoid these resonances. The working point for LHC, HL-LHC, HE-LHC and FCC-hh at injection is (.28, .31) and (.31, .32) at collision [38]. It has to be noticed that only the fractional part of the working point is responsible for resonances.

Dispersion

To describe particles with a relative momentum-offset of $\frac{\Delta p}{p}$ equation (3.11) has to be extended which leads to

$$z(s) = z_{nom}(s) + D(s)\frac{\Delta p}{p} \,, \tag{3.28}$$

where z_{nom} is the path of an on-momentum particle and $D(s)$ the *dispersion function*. It can be seen that the position of off-momentum particles scales linear with dispersion. Therefore this offset is at its maximum, where the dispersion has its maxima.

Momentum Compaction

The circumference C of off-momentum particles varies from nominal particles through

$$\frac{\Delta C}{C} = \alpha_C \frac{\Delta p}{p} \,, \tag{3.29}$$

where α_C is the *momentum compaction factor*. This factor depends on the lattice geometry and focusing arrangement. In lattices with a positive momentum compaction the path of higher momentum particles is longer compared to nominal particles. In lattices designed with zero momentum compaction the path length is independent of the momentum offset up to first order. If a lattice has a negative momentum compaction particles with higher momentum have a shorter orbit.

CHROMATICITY

The quadrupole strength k_1 acting on a particle depends on the particle momentum. This can be described as a quadrupole field error Δk which leads to a tune shift ΔQ:

$$\Delta Q \approx -\frac{1}{4\pi}\frac{\Delta p}{p}\int \beta(s)k_1(s)ds \,. \tag{3.30}$$

The *chromaticity* Q' relates this tune shift ΔQ to the relative momentum offset $\Delta p/p$

$$Q' = \frac{\Delta Q}{\Delta p/p} \approx -\frac{1}{4\pi}\int \beta(s)k_1(s)ds \,. \tag{3.31}$$

3.1.5 Longitudinal Dynamics

Particles do not only move transversely as discussed above, but they also perform longitudinal oscillations with respect to the reference particle.

ENERGY GAIN OR LOSS

Electromagnetic fields are used to accelerate particles. In the case of synchrotrons *radio frequency (RF) cavities* are used to provide high longitudinal electric fields. The energy gain or loss ΔE for a particle with charge q per turn is

$$\Delta E = q\Delta V \,, \qquad \Delta V = V_0 \sin(\omega_{RF} t + \varphi) \,, \tag{3.32}$$

where ΔV is the gap voltage, V_0 the peak accelerating voltage, ω_{RF} the RF frequency and φ the phase angle. The accelerating voltage can be illustrated as shown in Figure 3.5.

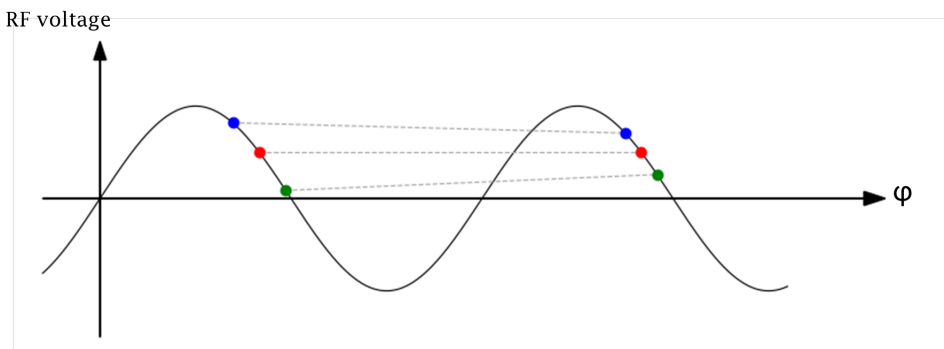

FIGURE 3.5: Illustration of the RF voltage.

The principle of *phase stability* in synchrotrons was discovered independently by McMillan [39] and Veksler [40]. The ideal, or *synchronous* phase φ_s depends on the

energy of the beam. If the revolution frequency is higher for particles with higher momentum, the synchronous phase is chosen as $0 < \varphi_s < \frac{\pi}{2}$. In the case that the revolution frequency is smaller for particles with higher momentum, the synchronous phase is $\frac{\pi}{2} < \varphi_s < \pi$, which is schematically illustrated in Figure 3.5, where the red particle is the ideal, or *synchronous particle*. The green particle has a higher momentum, arrives earlier in the acceleration gap and is therefore gaining less momentum. The blue particle with smaller momentum is stronger accelerated. In both cases, the off-momentum particles converge to the nominal momentum.

Transition Energy

As already mentioned above the synchronous phase depends on the revolution requency, which itself depends on the energy of the particles. The energy where the synchronous phase changes is named *transition energy*. At this energy the revolution frequency is independent of the particle energy. The transition energy is correlated with the momentum compaction factor α_C through

$$\alpha_C = \frac{1}{\gamma_T^2} . \tag{3.33}$$

The synchronous phase changes at transition energy. There, the synchronous phase is shifted by π as shown in Figure 3.6. This can be accomplished by a phase shift of $\pi - \varphi_s$ to the RF wave [33].

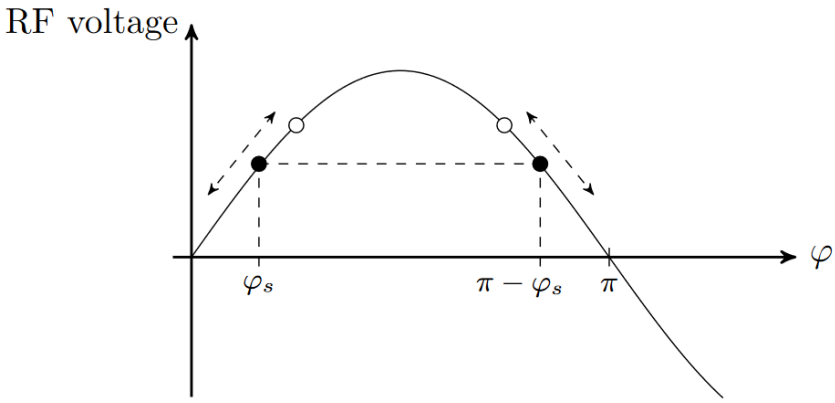

FIGURE 3.6: Visualisation of reference (synchronous) particle before and after transition energy [41].

Phase Slip Factor

The *phase slip factor* η is defined as

$$\eta = \frac{1}{\gamma^2} - \frac{1}{\gamma_T^2} , \tag{3.34}$$

where γ is the nominal particle energy and γ_T the transition energy.

HARMONIC NUMBER

The RF frequency f_{RF} has to be an integer of the revolution frequency f_{rev}, expressed through

$$f_{RF} = h\, f_{rev}\,, \tag{3.35}$$

where h is known as the *harmonic number*. This number defines the number of buckets. Each bucket can be filled with a proton bunch or can be empty.

SNYNCHROTRON MOTION

The acceleration of particles with RF cavities leads to oscillations in the longitudinal plane, similar to betatron oscillations in the transverse planes. These are called *synchrotron oscillations*. The *synchrotron tune* Q_s can be calculated using

$$Q_s = \sqrt{\frac{hqV|\eta \cos \varphi_s|}{2\pi\beta_{rel}^2 E}}\,, \tag{3.36}$$

where h is the harmonic number, q the particle charge, V the RF voltage, η the phase slip factor, φ_s the phase of the synchronous particle, β_{rel} the relativistic beta factor and E the nominal particle energy. It has to be noticed that $Q_s = 0$ at transition energy which leads to instabilities.

3.2 Performance Aspects

Collisions of the two beams start after the particle momentum reaches the desired collision energy. Relevant performance parameters are discussed in this section.

BUNCH POPULATION

The parameter *protons per bunch (ppb)* refers to the bunch population. Due to collisions the ppb decreases over time as the protons burn. Moreover the particles get lost due to scattering.

LUMINOSITY

There are different types of luminosity. First of all, the *instantaneous luminosity* $\mathcal{L}$ is the proportional factor between the number of events per second $\frac{\mathrm{d}R}{\mathrm{d}t}$ and the cross section σ [42],

$$\frac{\mathrm{d}R}{\mathrm{d}t} = \mathcal{L}\,\sigma\,. \tag{3.37}$$

It is given in units of $\mathrm{cm}^{-2}\mathrm{s}^{-1}$. Assuming two colliding gaussian beams the instantaneous luminosity becomes

$$\mathcal{L} = \frac{f_{rev} N_1 N_2}{4\pi\sigma_x\sigma_y} S \,, \tag{3.38}$$

where f_{rev} is the revolution frequency, N_1 and N_2 the number of particles of beam one and beam two and σ_x, σ_y the transverse beam size. S is the luminosity reduction factor which results from the bunches colliding under a non-zero crossing angle as shown in Figure 3.7. Assuming $\beta^* \gg \sigma_s$ the luminosity reduction factor is given as

$$S = \frac{1}{\sqrt{1 + \frac{\chi\sigma_s}{2\sigma_x}}} \,, \tag{3.39}$$

with the beta function at the interaction point β^*, the full crossing angle χ, the longitudinal beam size σ_s and the transverse beam size in the crossing plane σ_x.

The *integrated luminosity* $\mathcal{L}_{int}$ is defined as

$$\mathcal{L}_{int} = \int_{t_1}^{t_2} \mathcal{L}\, dt \,. \tag{3.40}$$

It is typically given in units of $\mathrm{fb}^{-1} = 10^{-39}\mathrm{cm}^{-2}$.

Luminous Region

An illustration of two colliding bunches is given in Figure 3.7. The *luminous region* is defined as the overlap of the bunches and has the dimension of a length.

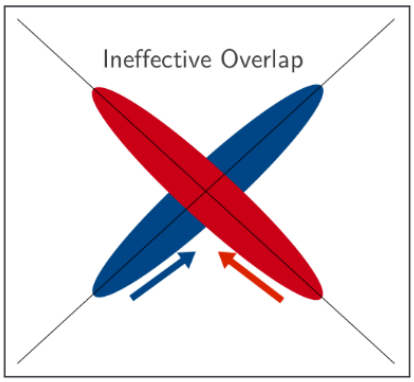

FIGURE 3.7: Illustration of the luminous region of two colliding bunches, adapted from [43].

Pile Up

The *pile-up* μ is the average number of events (collisions) per bunch crossing . It is correlated with the instantaneous luminosity $\mathcal{L}$ through [44]

$$\mu = \frac{\sigma \mathcal{L}}{f_{rev} n_b} , \tag{3.41}$$

where σ is the proton-proton inelastic cross section, f_{rev} the revolution frequency and n_b the number of colliding bunches.

Pile Up Density

The *pile-up density* $\varrho(s,t)$ describes the local distribution of events along s at time t [44]. Thus the pile up $\mu = \mu(t)$ is

$$\mu(t) = \int \varrho(s,t)\, ds . \tag{3.42}$$

The *peak pile-up density* is usually located at the interaction point. The *line pile-up density* refers to the longitudinal distribution of events and is given in units of mm^{-1}. This can be understood as events per mm. The *time pile-up density* refers to the time distribution of events and is given in units of ns^{-1}, which can be understood as events per ns.

Intrabeam Scattering

As already discussed particle perform betatron and synchrotron oscillations. Due to these oscillations particles within one bunch can collide as well. Multiple small angle scattering processes lead to an increase in beam emittance [45] which can limit the luminosity of a collider [46]. This effect is called *intrabeam scattering (IBS)* and is computed by MAD-X using the Bjorken-Mtingwa algorithm [47].

Beam Beam Long Range

Near the interaction point the two bunched beams share the same beam pipe, hence the beams interact electromagnetically with each other. These interactions are named *beam-beam long range interactions* and are illustrated in Figure 3.8.

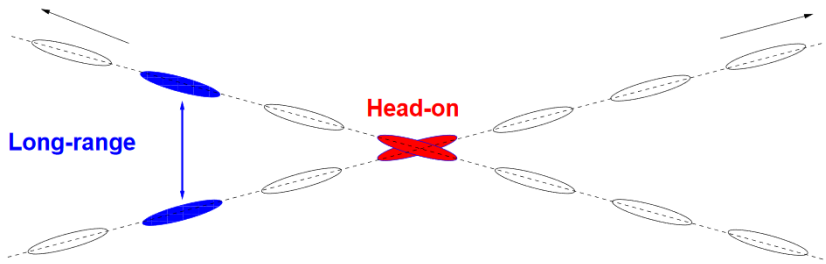

FIGURE 3.8: Schematic plot of two crossing beams with head-on collisions [48].

Head On

The beam-beam interaction is highly non-linear. Nevertheless one can define the linear *beam-beam parameter* ξ_{bb} as the magnitude of the linear tune shift, induced by the interaction between two *head-on* colliding beams, using [33]

$$\xi_{bb} = \frac{N_b r_0 \beta^*}{4\pi\gamma_{rel}\sigma^2} = \frac{N_b r_0}{4\pi\epsilon_n}, \tag{3.43}$$

with the number of protons per beam N_b, the beta function at the interaction point β^*, the relativistic γ_{rel} factor, the RMS beam size σ, the normalised emittance ϵ_n and the classical proton radius r_0 defined by

$$r_0 = \frac{q^2}{4\pi\epsilon_0 mc^2}, \tag{3.44}$$

with the particle charge q, the permittivity of free space ϵ_0, the particle mass m and the velocity of light c.

Levelling

As seen in equation (3.41) the instantaneous luminosity defines the number of events per crossing. The higher the pile-up is the more collisions take place. A detector has a manageable pile-up limit. Reasons are for example the delay time of a detector.

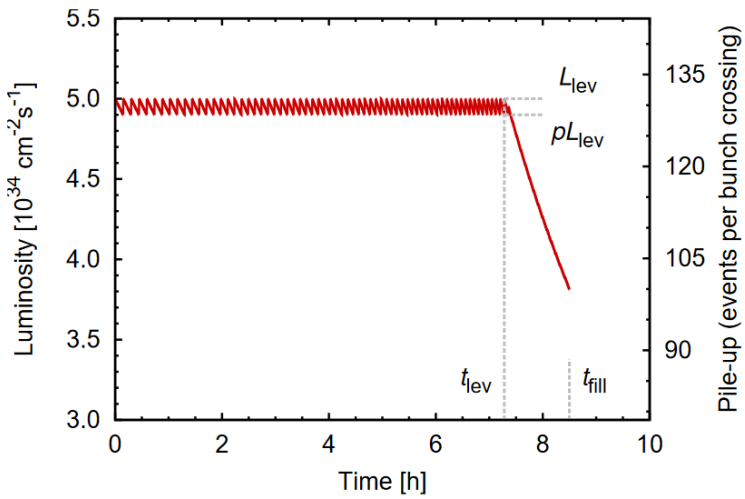

FIGURE 3.9: Example of levelled instantaneous luminosity and pile-up for the HL-LHC [44].

To keep the pile-up and the instantaneous luminosity at a certain level these parameters can be *levelled* [49]. The instantaneous luminosity $\mathcal{L}$ is proportional to

$$\mathcal{L} \propto \frac{1}{\beta^* \sqrt{1 + \frac{\chi^2 \sigma_s^2}{4\beta^* \epsilon}}} \tag{3.45}$$

with the beta function at the interaction point β^*, the full crossing angle χ, the longitudinal bunch length σ_s and the emittance ϵ. Through equation (3.45) it can be seen that three parameters are qualified to perform luminosity levelling, namely β^*, χ and σ_s. The emittance does not lend itself for levelling.

In the simulations for the HE-LHC β^* is used for levelling. At the beginning of levelling β^* is bigger than the smallest achievable value. With this initial configuration particles collide and therefore the protons burn off which leads to a decrease of the instantaneous luminosity and of the pile-up. When the luminosity or the pile-up are below a certain threshold, β^* is decreased which shifts the instantaneous luminosity and the pile-up to the initial value again.

As an example the levelling planned in the HL-LHC is plotted in Figure 3.9. The levelling time t_{lev} is the duration of the levelling process. After this duration the instantaneous luminosity as well as the pile-up decreases. After the fill time t_{fill} the beam gets dumped.

Turn Around Time

The *turn around time* is defined as the time needed to establish stable beams conditions after a beam dump has occurred [50].

Availability

The *availability* is the fraction of time where the accelerator runs as planned. Any disturbances lead to a decrease of the availability. In case of the HE-LHC, an availability of 75 % is assumed [27].

Time in Physics

The *time in physics* is defined as the fraction of time the accelerator spends in stable physics operation including turn around time. For example, in 2017 the time in physics of the LHC was 50 % of the availability [27].

Crab Cavities

Two colliding bunches do not overlap completely due to the crossing angle. To mitigate this problem the use of *crab cavities* is proposed, which were already used at the KEK-B collider in Japan [51, 52]. Crab cavities are radiofrequency cavities and similar to the RF cavities used for acceleration. The difference between these cavities

is that in case of the crab cavities the electromagnetic field is not used to accelerate the bunches but to induce a rotation. This leads to an increased overlap, luminous region, instantaneous luminosity and pile-up. However, in reality the rotation is not perfect due to the field provided by the crab cavities. The bunch shapes while using crab cavities is shown in Figure 3.10.

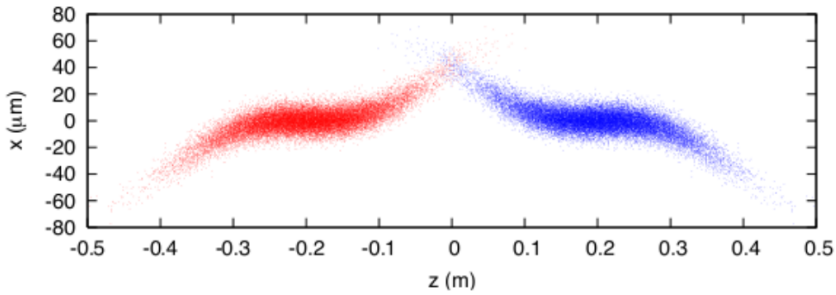

FIGURE 3.10: Two colliding bunches with crab cavities [43].

SYNCHROTRON DAMPING

Charged accelerated particles emit synchrotron radiation with an opening angle of $1/\gamma$, where γ is the relativistic Lorentz factor. Assuming ultra relativistic particles, which means $\gamma \gg 1$, the photons are emitted along the direction of motion which leads to a reduction of the beam momentum in the transverse planes, named *synchrotron damping*. As the particles are only accelerated longitudinally, the transverse momentum losses are not recovered by the cavity. This leads to a decay of the transverse emittance.

ADIABATIC DAMPING

With respect to equation (3.26), the emittance ϵ decreases with increasing energy. During acceleration only the longitudinal momentum of particles change while the transverse velocities remain unchanged. With increasing particle momentum the anglular divergence and therefore the transverse beam emittance becomes smaller. This effect called *adiabatic damping* is shown schematically in Figure 3.11.

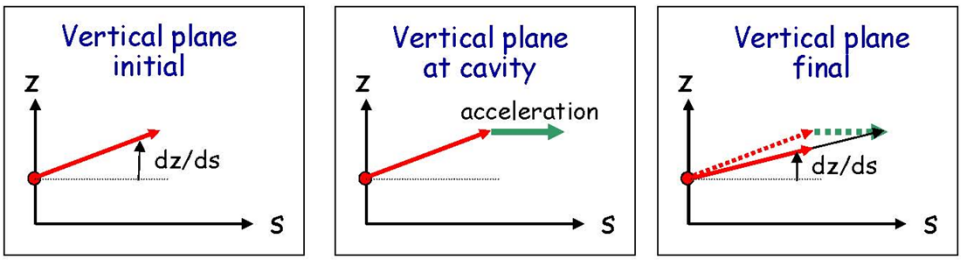

FIGURE 3.11: Adiabatic damping [53].

Achromatic Telescopic Squeezing

The *achromatic telescopic squeezing* scheme is a technique which allows to reach a 4 times smaller β^* than designed in the main experiments [54]. To reach this, the beta functions in the arcs neighbouring the main experiments and in the final focus triplet are higher compared to the nominal optics, which is shown in Figure 3.12.

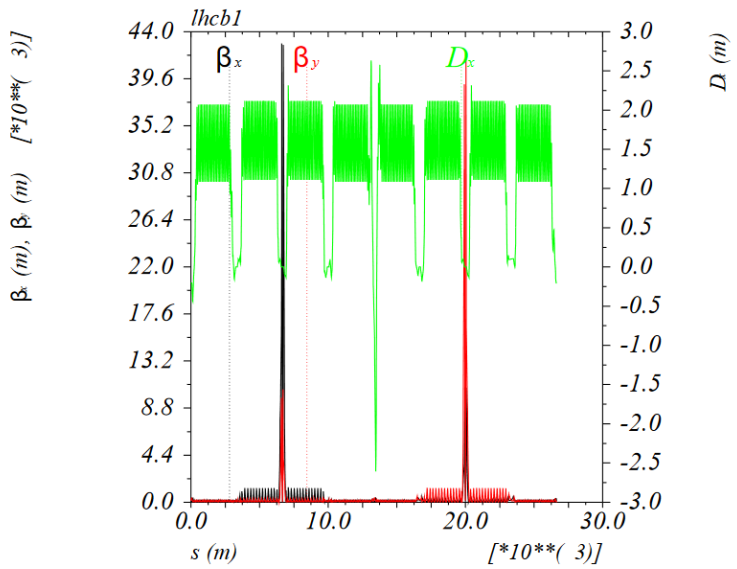

FIGURE 3.12: Achromatic telescopic squeezing for LHC beam 1 [54].

3.3 Aperture

In the context of accelerator physics the term *aperture* can have three different meanings. In the following these definitions are given.

The term *aperture* refers in most cases to the beam stay clear n. The beam stay clear describes how much space is available for the beam in the beam screen. It is given in units of the standard deviation of the gaussian beam (σ). The aperture in both transverse planes $n_{x,y}$ can be approximated using [55]

$$n_{x,y} = \frac{L_{x,y} - t_{x,y} - k_\beta D_{x,y,\delta_p}}{k_\beta \sigma} , \tag{3.46}$$

where $L_{x,y}$ are the horizontal and vertical dimensions of the half beam screen, $t_{x,y}$ refers to the misalignment tolerances, k_β to the beam size beating factor, $D_{x,y}$ to dispersion, δ_p to the relative momentum offset and σ to the RMS beam size. The beam size beating factor k_β and the relative momentum offset are defined as

$$k_\beta = \sqrt{1 + \frac{\Delta\beta}{\beta}} , \quad \delta_p = \frac{\Delta p}{p} . \tag{3.47}$$

The *physical aperture* is in general associated with the *beam screen* (BS). BS version 2018 is used for the HE-LHC studies, and is shown in Figure 3.13. In MAD-X the BS geometry is approximated by the orange line shown in Figure 3.13.

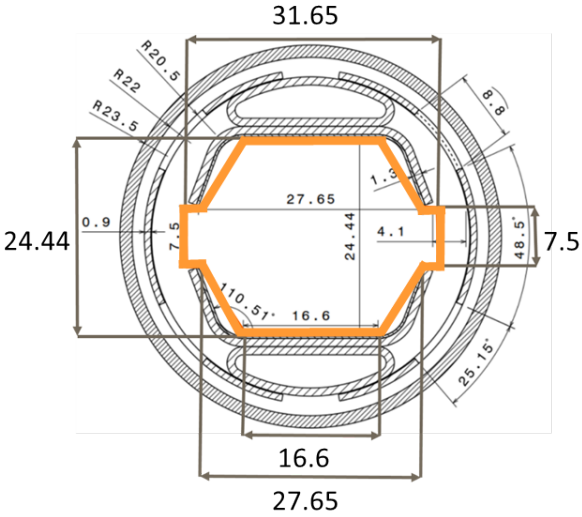

FIGURE 3.13: Beam screen 2018 [56].

In addition to the beam screen it is possible to define beam screen misalignment tolerances, which are shown in Figure 3.14.

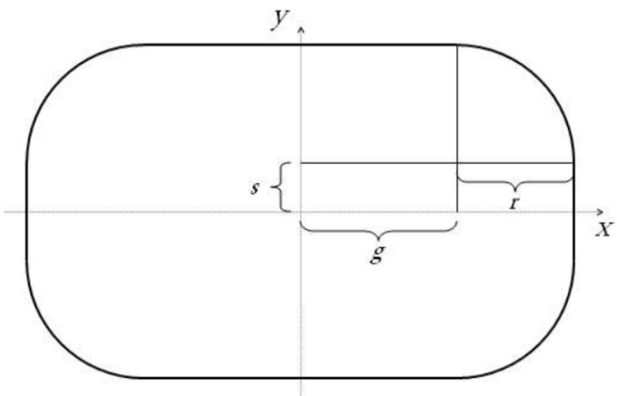

FIGURE 3.14: Beam screen misalignment tolerances [57].

The *dynamic aperture* is defined as the minimum amplitude in phase space where the particle motion is unstable. It can be computed using tracking codes like *Six-Track* [58].

3.4 Lattice Structures

3.4.1 FODO Cells

A *FODO* cell is a basic substructure consisting of one focusing (F) and one defocusing (D) quadrupole as well as drift spaces or dipoles (O) between. A schematic plot of a FODO cell is given in Figure 3.15. The quadrupoles focus the beam alternating in the horizontal and vertical plane.

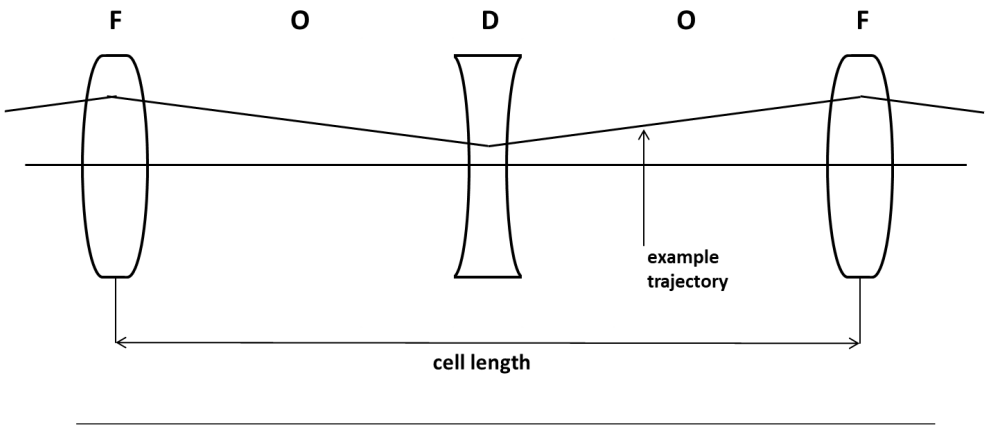

FIGURE 3.15: Schematic plot of a FODO cell.

3.4.2 Arcs

Combining multiple FODO cells leads to a larger bending structure, namely the *arc*. These parts of a synchrotron guide and focus the beam along the circumference.

3.4.3 Insertions

In circular machines the arcs connect the *insertions (also: insertion region, IR, long straight section, LSS)* where, for example the collision experiments take place. In contrast with the arcs, the IRs are long straight sections with various functionalities.

3.4.4 Dispersion Suppressor

In the IRs it is required to have a different dispersion than in the arcs, for example in an IR where an experiment is located the dispersion needs to be matched to zero at the collision point. Therefore a so-called *dispersion suppressor* (DS) connects the arcs with the IRs. The dispersion suppressor can be designed in a nearly infinite number of ways. Basic dispersion suppression concepts are given below.

Individual Quadrupoles

In principle it is possible to continue the same periodic FODO lattice in the DS. One difficulty, however is to fulfill the zero dispersion condition

$$D(s) \;=\; D'(s) \;=\; 0\,, \tag{3.48}$$

at the end of the DS [59] where s indicates the end of the DS. This means, that in the DS the dispersions decreases to zero while the beta and alpha function continue preferably periodically. In reality, the beta functions reach higher values than in the arc which impacts the beam stay clear negatively. One advantage of this scheme is that no specific lattice and magnet design is required. On the other hand, the matching to zero dispersion results in generally stronger quadrupoles compared to the arcs.

Half Bend

This scheme halves the number of dipoles in a DS cell compared to an arc FODO cell. This can be achieved by using either half the number of dipoles or by halving their bending angle. The bending angle can be halved by using shorter and weaker dipoles, which leads to a different dipole type in the DS than in the arcs. The general condition for vanishing dispersion is [59]

$$2\,\theta_{DS}\;\sin^2\left(\frac{n\,\mu}{2}\right) \;=\; \theta_{arc}\,, \tag{3.49}$$

where θ_{DS} and θ_{arc} are the bending strengths respectively in the dispersion suppressor and in an arc cell, μ the phase advance and $n \in \mathbb{N}$ cells in the DS. Assuming a half bend scheme, which means

$$\theta_{DS} \;=\; \frac{1}{2}\,\theta_{arc}\,, \tag{3.50}$$

leads to

$$\sin^2\left(\frac{n\,\mu}{2}\right) \;=\; 1 \quad \text{equivalent to} \quad \cos(n\,\mu) \;=\; -1\,. \tag{3.51}$$

Equation (3.51) is fulfilled for phase advances

$$n\,\mu \;=\; k\,\pi, \quad \text{with} \quad k \;=\; 1, 3, ... \tag{3.52}$$

Condition (3.52) is for example fulfilled for $\mu = 90^\circ$ phase advance with $n = 2$ dispersion suppression cells.

Missing Dipole

As the dispersion is mainly an effect induced by the dipoles it is possible to reduce the dispersion by removing dipoles in the DS cells. This freed space can be used to increase the filling ratio or to include new elements.

3.5 The LHC

The LHC has two counter rotating proton beams, crossing at four points where experiments take place, as shown in Figure 3.16. As the HE-LHC is designed to fit in the already existing tunnel, it shares the same conceptual design with the LHC [20, 26]. In the arcs the two beams travel in the same horizontal plane, but one is travelling in the inner aperture while the other beam travels in the outer aperture. The distance between two IPs is therefore not identical for the two beams over one arc. As both beams travel the same length in inner and outer apertures, after one revolution the path of the two beams are identical.

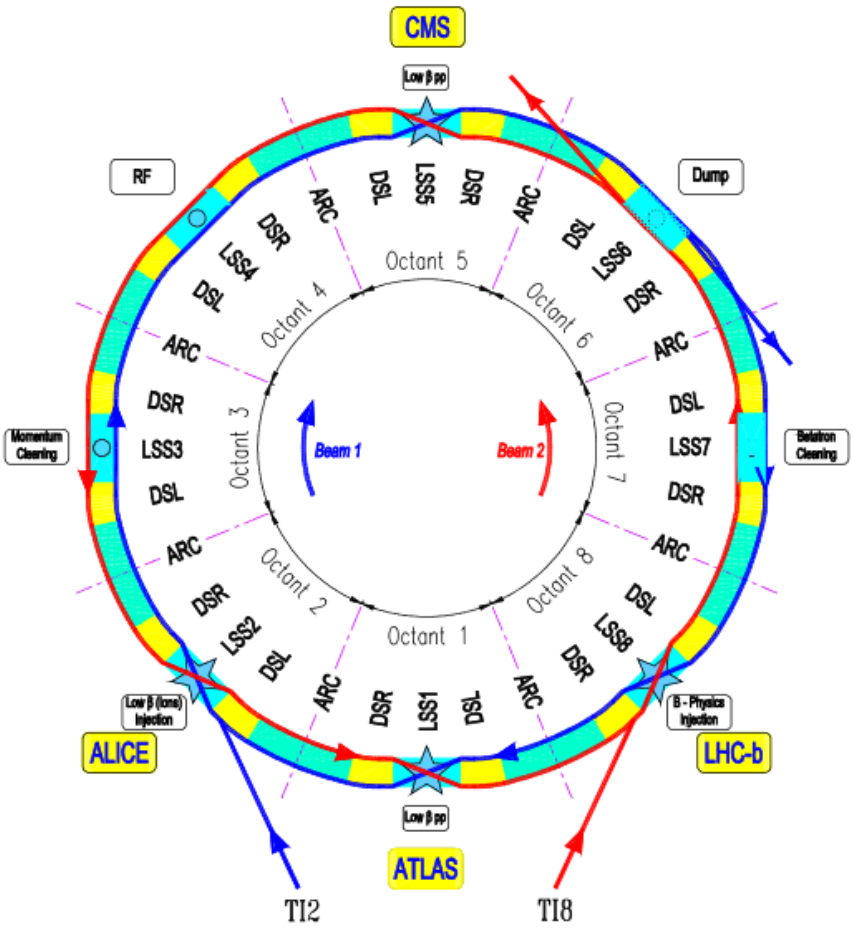

FIGURE 3.16: LHC ring layout [20].

3.5.1 LHC FODO Cell

In Figure 3.17 a schematic plot of a LHC FODO cell is given. The 106.9 m long cell starts with a decapole corrector (MCD) and octupole correcter (MCO) corrector followed by three dipoles where each is 14.3 m. In total three MCD and a MCO correctors can be found as they are located after every two dipoles. A sextupole corrector (MCS) is attached to every dipole. A trim quadrupole (MQT) is located before the quadrupoles. This quadrupole type matches the tune to the working point. This is true however, for the first four cells located nearest the IR. In all other cells an octupole magnet (MO) replaces the MQT. The first quadrupole is defocusing. This is illustrated as it is located negatively in an imaginary vertical axis. A sextupole (MS) and an vertical orbit corrector (MCBV) are located next to it. After another three dipoles a focusing quadrupole with attached MQT, MS and horizontal orbit corrector (MCBH) can be found.

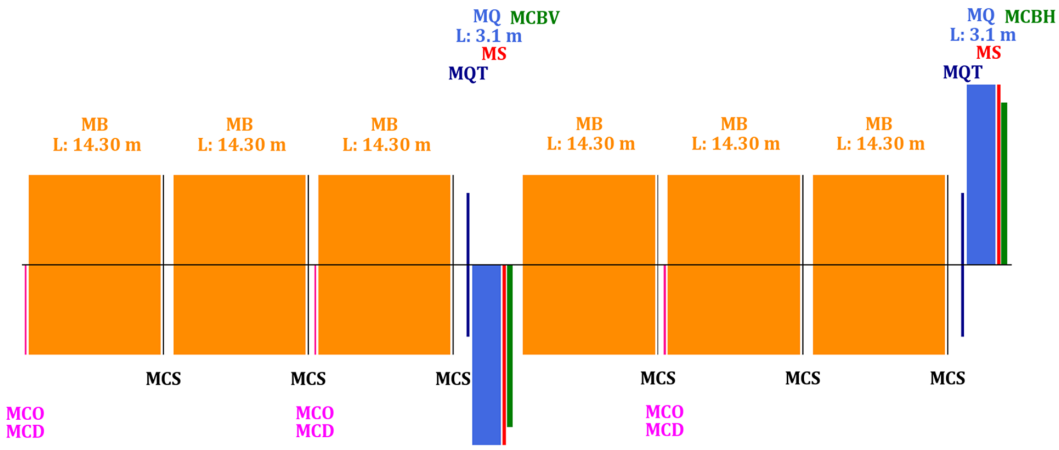

FIGURE 3.17: LHC FODO cell.

3.5.2 LHC Arcs

Each of the eight arcs in the LHC is 2.79 km long and is made of 23 FODO cells, where each is matched to a phase advance of 90° in both planes. Therefore the LHC arc has a *23x90* lattice, where 23 refers to the number of cells and 90 to the phase advance. This naming convention is taken for the HE-LHC as well. *Arc12* refers to the sector connecting IR1 and IR2. As shown in Figure 3.17 a MQT is located next to every quadrupole. Coming from the IR, the first regular arc cell is part of the DS.

The quadrupoles in each sector are powered in series for beam 1 and beam 2. Contrary, the correctors can be adjusted seperately for the two beams.

3.5.3 LHC Insertions

Each IR is 528 m long. As the HE-LHC shares a similar design with the LHC, the IRs share the same functionalities as well [20, 26]:

IR1 The first LHC main experiment *ATLAS* [60] is located in IR1.

IR2 Beam 1 is injected clockwise in IR2. Moreover the LHC hosts the *ALICE* [61] experiment here.

IR3 Momentum collimation takes place in IR3.

IR4 The RF cavities and beam instrumentation are located in IR4.

IR5 The second main experiment is located in IR5. In case of the LHC this experiment is *CMS* [62].

IR6 Both beams get dumped in IR6.

IR7 Transverse collimation takes place in IR7.

IR8 Beam 2 is injected counter clockwise in IR8. Currently the *LHCb* [63] experiment is integrated here.

3.5.4 LHC Dispersion Suppressor

The LHC DS is a combination of six individual powered quadrupoles, reduced number of bending magnets and a missing dipole scheme. It is a combination of an irregular part where the number of dipoles per cell is reduced with respect to a regular FODO cell and one regular FODO cell. These two regions are separated by a drift space which is about 13 m long.

A different DS scheme is integrated next to IR3 and IR7 compared to the other IRs. Both DS schemes, which are shown in Figure 3.18, are located right of the IR. In both designs, one half cell of the irregular part is made of two dipoles which are identical to the arc dipoles. The quadrupoles used in the DS are in general longer than in a regular arc cell and are powered individually in the DS which is next to IR1, IR2, IR4, IR5, IR6 and IR8. The quadrupoles used in the DS next to IR3 and IR7 have the same strengths as in the arcs. In this case, every quadrupole (MQ) is followed by one or two trim quadrupoles (MQTLI) used for matching. An orbit corrector (MCB) is located next to a quadrupole in each DS. The trim quadrupoles as well as the orbit correctors used in the irregular part of the DS are longer compared to the respective arc elements.

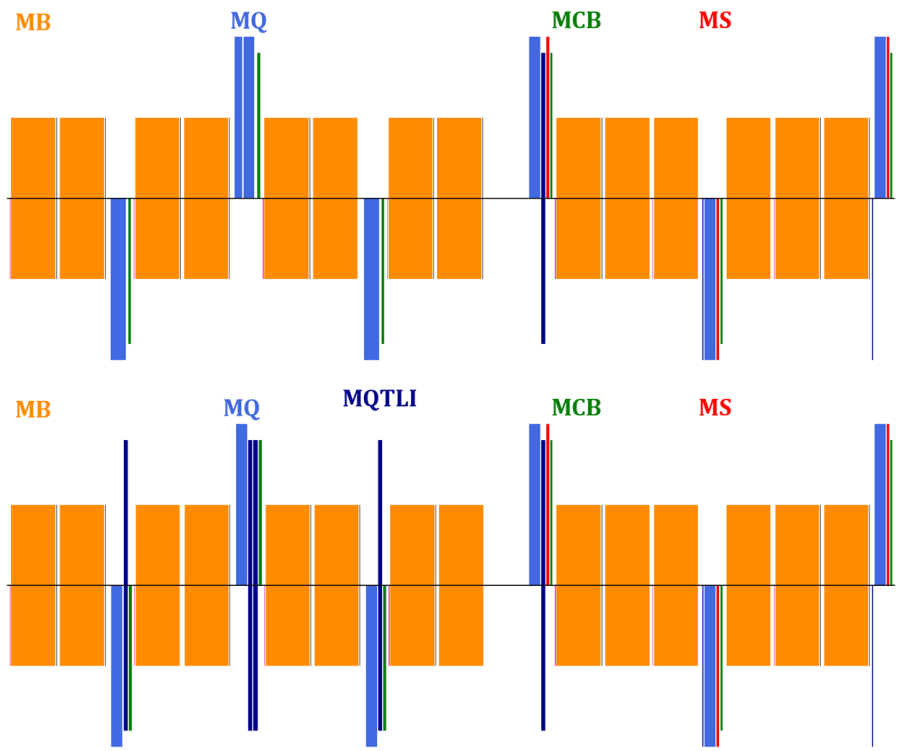

FIGURE 3.18: Schematic plot of the LHC dispersion suppressor. A regular arc cell is made of six dipoles. Top: Integrated dispersion suppressor located next to IR1, IR2, IR4, IR5, IR6 and IR8. Bottom: Integrated dispersion suppressor located next to IR3 and IR7.

3.5.5 LHC Parameters

The design cell parameters of the LHC are summarised in Table 3.1 [20, 64]. Each cell is matched to 90° phase advance horizontally and vertically and has a length of 106.9 m. Each of the six main dipoles is 14.3 m long and produces a field of 8.33 T at top energy of 3.5 TeV per beam [14]. The filling factor indicates how much space in

Cell Parameter	Unit	LHC
Phase Advance per Cell	°	90
Cell Length	m	106.9
Dipoles per Cell	–	6
Dipole Length	m	14.3
Bending Angle per Dipole	°	0.29
Dipole Field at 4 TeV Energy	T	8.33
Filling Factor	–	0.80
Quadrupole Length	m	3.1
β_{max}/β_{min}	m	177/32
D_{max}/D_{min}	m	2.20/1.10

TABLE 3.1: LHC cell design parameters.

Ring Parameter	Unit	LHC
Injection Energy	GeV	450
Collision Energy	TeV	13
Momentum Compaction	10^{-4}	3.21
Transition Energy	GeV	55.81
Horizontal Tune at Injection	–	64.28
Vertical Tune at Injection	–	59.31
Horizontal Tune at Collision	–	64.31
Vertical Tune at Collision	–	59.32
Longitudinal IBS Growth Time	h	63
Horizontal IBS Growth Time	h	105

TABLE 3.2: LHC ring design parameters.

a cell is filled with dipoles. In case of the LHC the filling factor is 0.8. The maximum and minimum of the beta function and the dispersion in a FODO cell are 177 m/32 m and 2.20 m/1.1 m respectively.

Important ring parameters summarised in Table 3.2 [20, 64]. A momentum compaction of 3.21×10^{-4} results in a transition energy of 55.81 GeV. The SPS injects 450 GeV beams in the LHC which is about 8 times higher than the transition energy. Therefore the synchronous phase remains constant. The tunes are matched to a working point of (.28, .31) at injection energy and (.31, .32) at collision energy. Intrabeam scattering (IBS) leads to an emittance blow up, with longitudinal and horizontal growth times of collision energy are 63 h and 105 h.

3.6 Main Dipole Errors

The magnetic field of the dipoles can be expanded as [65]

$$B_y + iB_x = B_{ref} \sum_{n=1}^{\infty} (b_n + ia_n) \left(\frac{x + iy}{R_{ref}} \right)^{n-1} , \tag{3.53}$$

where the terms a and b indicate skew and normal components and B_{ref} the magnetic field at the reference radius R_{ref}. The subscript $n = 1$ refers to a dipole, $n = 2$ to a quadrupole and so on. In this thesis the effect of systematic quadrupole errors (b_2 *errors*) in the arc dipoles are discussed.

The main dipoles for the LHC and HE-LHC have a 2-in-1-design, in which every arc dipole hosts the two beam pipes. The b_2 error has opposite sign between the inner and outer beam apertures. The systematic b_2 errors increase when the beam separation decreases. This means that reducing the b_2 errors is possible by enlarging the distance between the two beam pipes.

Errors are usually given in units of 10^{-4} relative to the main field at a reference radius. The current systematic HE-LHC quadrupole errors are estimated at a reference radius of 16.7 mm. At injection the systematic normal b_2 error is ± 2.23 units and at collision ± 46.84 units [66]. In case of the LHC main dipole magnets the b_2 error is about ± 1.4 units at injection and collision energy at a reference radius of 17 mm [65].

3.7 MAD-X

The 10th version of the Methodical Accelerator Design *MAD-X* [67] is described in its user manual [57] as

> *MAD-X is a general-purpose tool for charged-particle optics design and studies in alternating-gradient accelerators and beam lines. It can handle medium size to very large accelerators and solves various problems on such machines.*

All studied lattice designs and optics aspects as well as the performance estimations were performed using MAD-X. The used modules are briefly explained below.

SURVEY

The *SURVEY* module computes the coordinates of each element over the whole lattice in a global reference system. Optics parameters are not computed at this stage. These coordinates refer to the geometrical layout, which is shown in Figure 3.19,

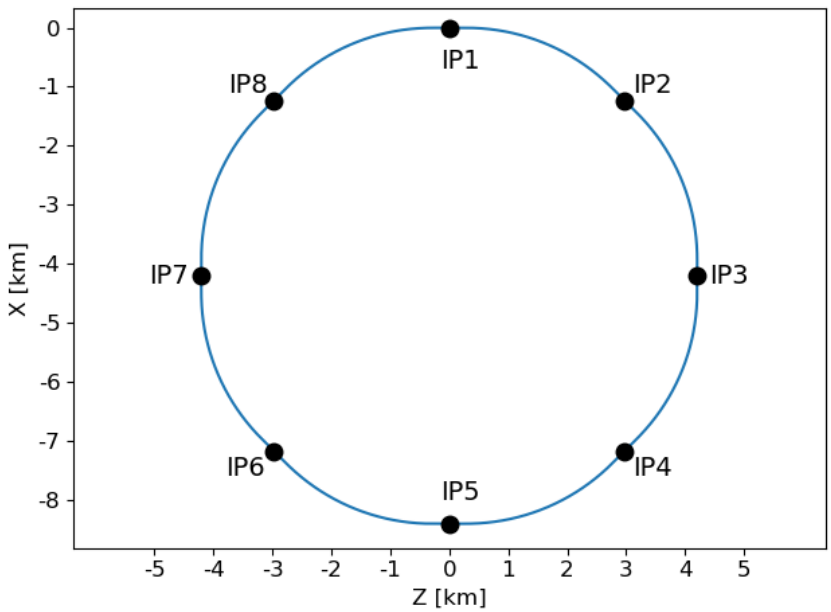

FIGURE 3.19: Survey of the ring with marked interaction points (IPs).

where the survey x and z coordinates of the LHC are plotted. IP1 is taken as a starting point, located at $z = 0$, $x = 0$.

TWISS

Optics functions are computed by the *TWISS* module. For this, a sequence and the optics are required.

MATCH

The term *matching* refers to the MAD-X internal process to find the most accurate magnet strengths for a set of constraints using different minimisation algorithms. Constraints can be maximum feasible strengths or optics functions.

APERTURE

The *APERTURE* module is used for calculation of the beam stay clear. This calculation requires the optics as well as a definition of the beam screen and the tolerances using *APERTURE* and *APERTOL*. Parameters used for all aperture calculations in this thesis are summarised in Table 3.3. Detailed explanations can be found in the MAD-X user guide [57].

MAD-X input	Description	Unit	Value
APERTOL	Aperture Tolerances	m	0.001, 0.001, 0.001
HALO	Halo Parameters	σ	6, 6, 6, 6
BBEAT	Beam Size Beating	–	1.05
DPARX	Frac. Hor. Paras. Disp.	–	0.14
DPARY	Frac. Ver. Paras. Disp.	–	0.14
COR	Closed Orbit Uncertainty	m	0.002
DP	Relative Momentum Offset	–	0.00086

TABLE 3.3: Input parameters for aperture calculation.

Chapter 4

ALGEA

4.1 Motivation

During the design of the HE-LHC it is essential to find the lattice which best meets all requirements like energy reach or geometry contraints. Generating, simulating and analysing lattices with different properties, like number of FODO cells and the used dispersion suppressor, is a major part of the development of a new accelerator. In order to simplify the arc and dispersion suppressor generation, a new tool named *ALGEA* (Automatic Lattice GEneration Application) [1] is developed. This tool enables easy integration of interaction region designs, which need to be developed separatly. In addition to generating the accelerator sequence, the magnet powering scheme is also defined by the code. Two extra files with the aperture and the aperture tolerance definitions are created. In the following the required parameters, the output as well as the features are explained.

4.2 Constraints and Parameters

The HE-LHC will be built in the existing LHC tunnel and therefore shares the same conceptual design. Thus the circumference is set to about 26.658 km. Moreover, the position of the IPs along the ring remain unchanged, where IP1 is taken as a reference point and is therefore located at $s = 0$ km and $s = 26.658$ km. The locations of all eight IPs are summarised in Table 4.1.

IP Number	Position [km]	IP Number	Position [km]
1	0 / 26.658	5	13.329
2	3.332	6	16.662
3	6.665	7	19.994
4	9.997	8	23.315

TABLE 4.1: Location of interaction points for the HE-LHC.

[1] In greek mythology the Algea were the personified spirits (daimones) of pain and suffering body and mind, grief, sorrow and distress. They were the bringers of weeping and tears [11].

Minimal drift spaces between elements are taken as a constraint. For the HE-LHC the required drift spaces are summarised in Table 4.2. The term *element* refers to any element in an arc except for a dipole.

Neighbouring Elements	Drift Space [m]
Dipole - Dipole	1.5
Dipole - Element	1.3
Element - Element	0.35

TABLE 4.2: Required drift spaces between elements.

The separation between beam 1 and beam 2 in the arcs is different compared to the separation in the IRs. In this thesis two different separations are taken into account. Even though the 2018 maget design respects a beam separation of 25.0 cm, the error studies are performed using the 20.4 cm beam separation of the 2017 magnet.

Region	Separation [cm]	
	2017	2018
Arc	20.4	25.0
IR4	42.0	42.0
IR3	22.4	28.0
IR7	22.4	28.0

TABLE 4.3: Beam separation for the 2017 and 2018 magnet design.

The length of the eight long straight sections is fixed by the tunnel geometry to 545 m. The IRs are located within these sections. Initially, the starts and ends of the dispersion suppressors, remain identical to the LHC. In a later step of the lattice generation, the start and end points of the dispersion suppressors are varied by ALGEA. It is only possible however, to set these markers further way from the IPs, as otherwise elements of the DS and the IR would overlap.

In addition to the parameters above, information concerning the arcs need to be defined at the beginning of a generation using ALGEA. The number of cells per arc and the number of dipoles per cell need to be fixed. The dipole length is then calculated by ALGEA. For this, the lengths of all elements located in a cell need to be defined first. Moreover the integrated DS type needs to be fixed so the bending angle per dipole can be calculated.

4.3 Dispersion Suppressor Options

Depending on the number of dipoles per FODO cell a different DS scheme is used. Lattices with the same number of cells per arc but with different DS schemes have been studied as well.

The integrated HE-LHC DS optics are similar to the DS design used in the LHC. Therefore a DS is made of a regular part and an irregular part. The regular part of the DS is the first FODO cell of the arc, with the difference that in this cell the quadrupole strength varies from the arc. The irregular part of the DS is made of two cells with a reduced number of dipoles per cell, compared to a FODO cell. A drift space of about 10 m to 20 m connects these two parts. Starting from the IR the beam travels first through the irregular part and then through the regular part. In the following discussion the integrated DS types for lattices with six dipoles per FODO cell are shown and the irregular part is explained in detail. All plots show the DS located right from the IR. All DS options implemented in the possible HE-LHC lattices are summarised below.

DS1

The irregular part of the DS is made of eight dipoles. One half cell of the irregular part is made of two dipoles which are identical to the arc dipoles. The quadrupoles used in the DS are in general longer than in a regular arc cell and are powered individually. Using this scheme, three different DS layouts are chosen, depending on the IR.

In the DS next to IR3 and IR7, which is shown in the middle of Figure 4.1 every quadrupole (MQ) is followed by one or two trim quadrupoles (MQTLI). Both quadrupole types are used for matching. An orbit corrector (MCB) is located next to every quadrupole. The trim quadrupoles as well as the orbit correctors used in the irregular part of the DS are longer compared to the respective arc elements. Next to IR1 and IR5 longer quadrupoles with 6 m are needed to ensure sufficient matching flexibility [68], which is shown in the top plot of Figure 4.1. In the bottom plot of Figure 4.1 the DS integrated next to IR2, IR4, IR6 and IR8 is shown.

This DS type, which consists of three DS designs, depending on the IR, is used in lattices with six or eight dipoles per arc cell in HE-LHC lattices. In case of a lattice with eight dipoles per arc cell this represents to a half bend DS scheme. In general, the half bend DS scheme is found to be a very effective DS scheme. which is found to be a very effective DS scheme. In the following work this DS scheme is named *DS1*.

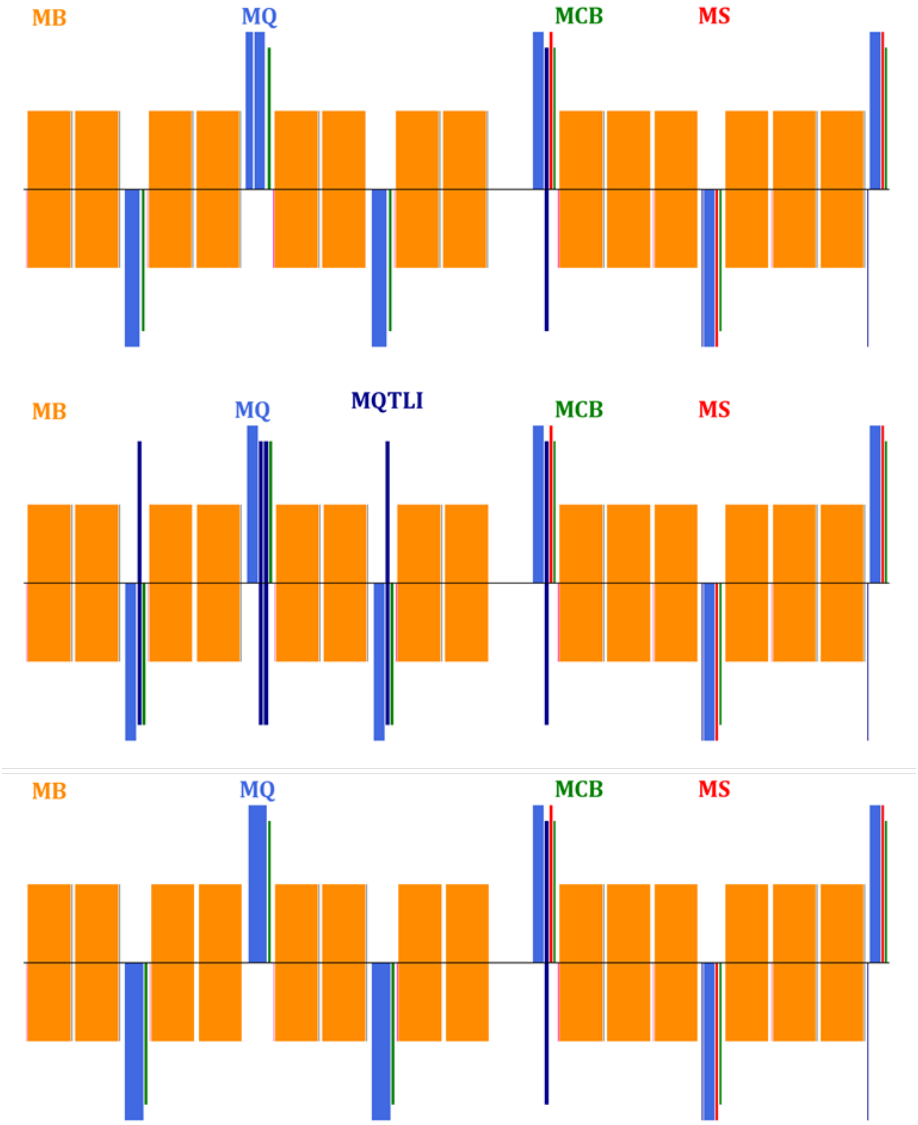

FIGURE 4.1: Schematic plot of the HE-LHC DS1. A regular arc cell is made of six dipoles. Top: Integrated dispersion suppressor located next to IR2, IR4, IR6 and IR8. Middle: Integrated dispersion suppressor located next to IR3 and IR7. Bottom: Integrated dispersion suppressor located next to IR1 and IR5.

DS2

In contrast to DS1, in the DS2 design each half cell contains only one dipole which is identical to an arc dipole as shown in Figure 4.2. Moreover the same DS is integrated next to all IRs. Except for the number of used dipoles this DS is identical to the DS1 located next to IR2, IR4, IR6 and IR8. All quadrupoles are powered individually. This DS scheme is used in lattices with two or three dipoles per half cell. In lattices with two dipoles per half cell this scheme refers to a half bend DS scheme. In the following work this DS scheme is named *DS2*.

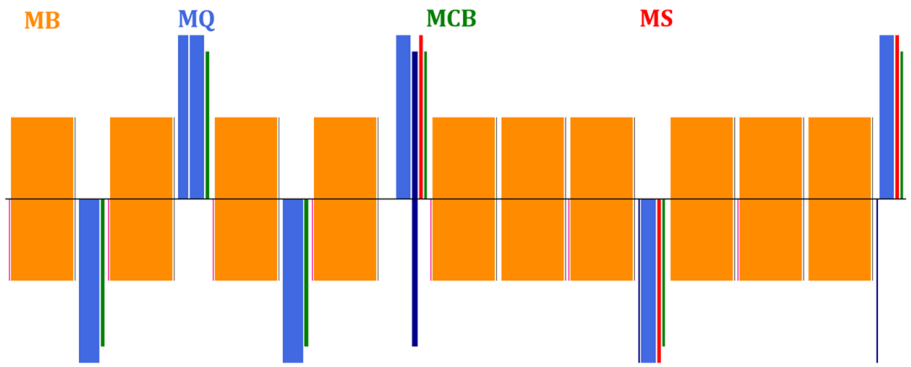

FIGURE 4.2: Schematic plot of the HE-LHC DS2. The irregular part contains one dipole per half cell. In this example, a regular arc half cell is made of three dipoles.

DS3

This DS scheme, which is shown in Figure 4.3, is specially designed for lattices with three dipoles per half cell, where no half bend scheme can be integrated using the same dipole type as in the arc. To generate a half bend scheme this DS requires different dipoles in the irregular part of the DS compared to the arc. The length and the angle of a dipole in the irregular part are 3/4 of the dipole length and bending angle obtained in a regular arc cell. The quadrupoles are powerd individually. This DS is located next to all IRs, if used in a HE-LHC lattice. In the following work this DS scheme is named *DS3*.

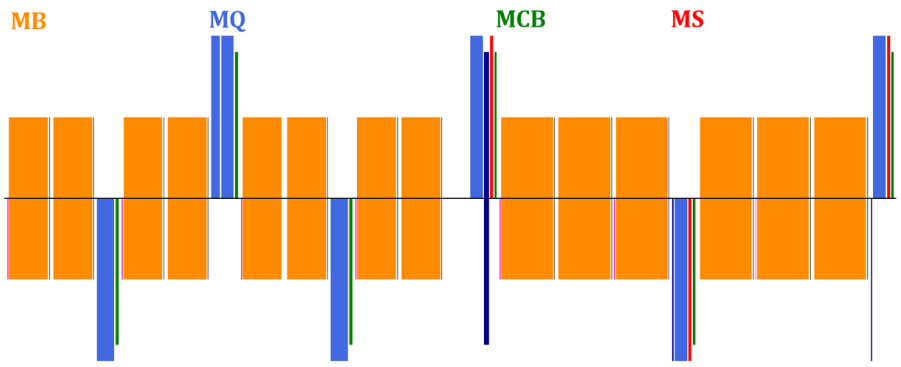

FIGURE 4.3: Schematic plot of the HE-LHC DS3, where two dipole types are required. The dipoles in the irregular part are shorter and weaker compared to an arc dipole. A regular half FODO cell is made of three dipoles.

4.4 Survey Fitting

One of the main constraints for the studied HE-LHC lattice design is the tunnel geometry. To solve this problem an automatic survey fitting feature is part of ALGEA.

A schematic plot of the dispersion suppressors and the arc between two IRs is shown in Figure 4.4. The DS as well as an arc are illustrated as blue bars and the IPs are marked as red stars. The start of the irregular parts of the DS are marked with *Start DS*. *Start Arc* refers to the start of the first regular arc cell, which is part of the DS. Between these structures a long drift space is located. The generated HE-LHC lattice gets fit to the geometry in so far as the offset between the LHC and the HE-LHC is minimised. This is performed by varying the start positions and therefore the length of the drift spaces between the irregular and regular parts of the DS, as well as varying the drift spaces between the dipoles and the quadrupoles in the irregular part of the DS, which is illustrated by blue arrows in Figure 4.4.

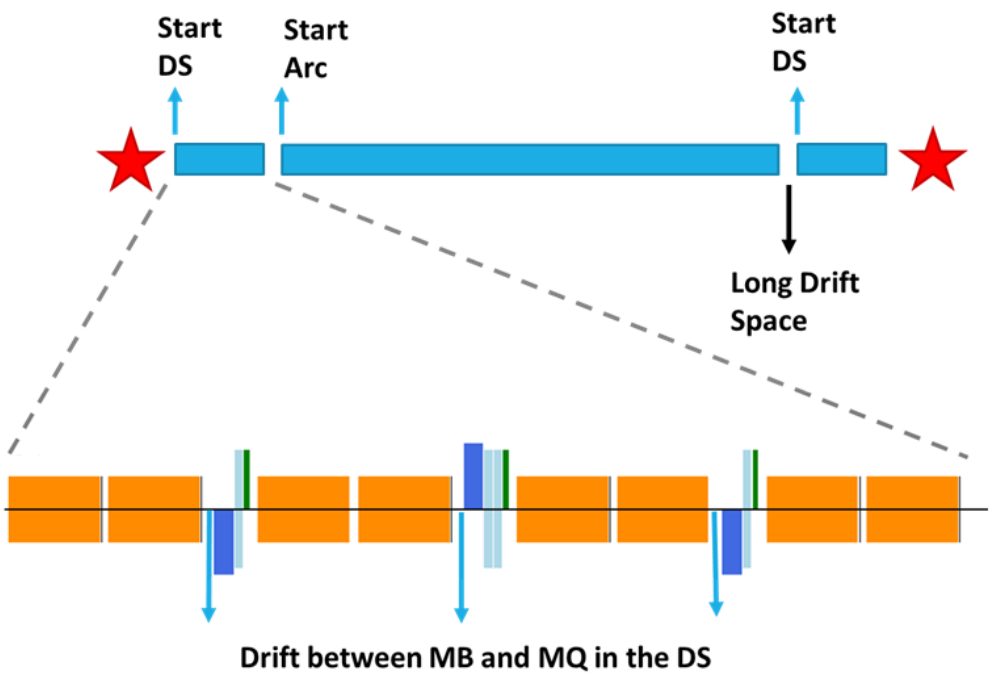

FIGURE 4.4: Illustration of the parameters for survey fitting between two interaction regions. The interaction points are marked as red stars. The dispersion suppressors as well as an arc is illustrated as blue bars.

The following starting positions and lengths are varied:

- **Start DS**: The start of the irregular part of the DS
- **Start Arc**: The start of the first regular arc cell
- **Start of Quadrupoles**: The drift spaces between a dipole and the next quadrupole in the irregular part of the DS
- **Cell Length**: The cell length, if varying the above mentioned drift spaces is not sufficient
- **Dipole Length**: The dipole length, if the cell length is varied

The importance of the survey fitting algorithm is demonstrated in Figure 4.5. In this example an 18 cells design with the integrated LHC dispersion suppressor is fit to the LHC survey using the survey fitting algorithm above. Without this algorithm the offset between this HE-LHC lattice and the LHC is asymmetric and is up to about 35 cm as shown in Figure 4.5a. By using this algorithm the maximum offset reduces to about 10 cm, which is shown in Figure 4.5b. Moreover the offset is distributed symmetrically about the middle of the arc, where the minima are located. In addition to the 3 times larger arc offset, the difference between $IP5_{LHC}$ and $IP5_{HE\text{-}LHC}$ is about 0.1 m in the survey z-axis and about 11 m in the survey x-axis before the survey fit. Afterwards, both offsets are reduced below 0.01 m.

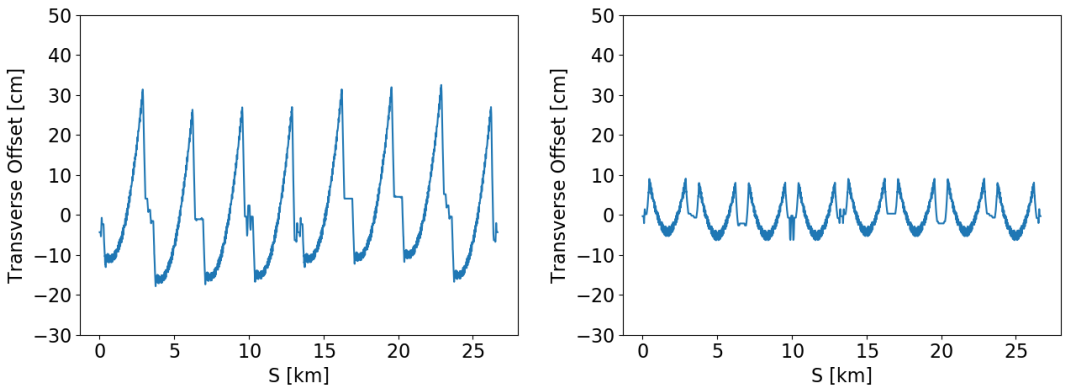

(A) Without survey fitting (B) With survey fitting

FIGURE 4.5: Difference between the LHC and the HE-LHC layout before (left) and after (right) the survey fitting algorithm.

4.5 Output

While respecting all constraints, the survey fitting feature and a naming convention, the output file contains the sequence for beam 1 and beam 2 as well as the powering. An example of the naming convention is shown in Figure 4.6.

```
  MCS.C34R1.B1:MCS,                  at= 1662.33155+(77-IP1OFS.B1)*DS,         from= IP1;
  BPM.34R1.B1:BPM,                   at= 1662.8777+(77-IP1OFS.B1)*DS,          from= IP1;
  MO.34R1.B1:MO,                     at= 1663.3877+(77-IP1OFS.B1)*DS,          from= IP1;
MQ.34R1.B1:MQ,                       at= 1665.6477+(77-IP1OFS.B1)*DS,          from= IP1;
  MS.34L2.B1:MS,                     at= -1664.1947+(77-IP2OFS.B1)*DS,         from= IP2;
  MCBV.34L2.B1:MCBV,                 at= -1663.1032+(77-IP2OFS.B1)*DS,         from= IP2;
  MB.C34L2.B1:MB,                    at= -1654.56353+(77.5-IP2OFS.B1)*DS,      from= IP2;
```

FIGURE 4.6: Sequence output of ALGEA.

This example is taken from a 23 cells per arc design for beam 1 in the middle of the arc between IP1 and IP2. It can be seen that the element positions are referred to the nearest IP. For example, *MQ.34R1.B1:MQ* means that this quadrupole (*MQ*) is the 34th quadrupole right from IP1 (*R1*) of beam 1 (*B1*). After this element, the elements are counted left from IP2 (*L2*). The term *(77-IP1OFS.B1)*DS* specifies the path difference induced by the dipoles for beam 1 and beam 2, as explained in Section 3.5, where *DS* refers to the path difference per dipole. As the path difference equals zero after one revolution, IP1 is chosen as a reference. From this IP beam 1 travels clockwise, starting in the outer aperture and passing through the main dipoles. Each passed dipole of a particle travelling in an outer aperture is counted as a positive path difference due to the longer path. For the beam travelling in the inner aperture, the dipoles passed are counted negatively. In the example shown in Figure 4.6, *77* is the number of dipoles passed starting from IP1. The term *IP1OFS.B1* is identical to the number of dipoles passed at IP1. This means that the offset in the LSS are zero as there the two beams travel in parallel.

In addition to the file which contains the sequence and the powering, two further files are generated where the aperture and the aperture tolerances are defined for every element. To simplify, all elements in the DS and the arcs have a *RECTELLIPSE* beam screen [57]. The outputted beam screen and aperture tolerances are defined as:

APERTYPE=RECTELLIPSE, APERTURE={ 0.015, 0.0132, 0.015, 0.015};

APER_TOL={ 0.0, 0.001, 0.001 };

Chapter 5

HE-LHC Design

Before concluding on two HE-LHC baseline lattices, different arc cell and dispersion suppressor options are discussed. Afterwards the merit of each design is explored.

As the focuses of this thesis are the arc and the DS design, the IRs are not explained in detail. Nevertheless, the current IR optics designs for both beams can be found in Appendix A.

5.1 Lattice Options

Major constraints on the HE-LHC are the target energy of 27 TeV and the minimum beam stay clear of $10\,\sigma$ [69] at 450 GeV injection energy. To fulfill both requirements eight different arc cell options are studied, where one cell is made of four to eight dipoles [70]. In order to obtain results for a realistic accelerator, the studied arc cell options are integrated simultaneously with a dispersion suppressor and the IRs. The lattices are studied regarding aperture, energy reach and geometry. A summary of all arc cell options is given in Tables 5.1 and 5.2. For all these lattices the beam separation of 2017 is chosen (see Table 4.3).

The number of dipoles per cell is chosen to keep the lengths between 13 m to 20 m. Below 13 m the required dipole field exceeds its limit [71] of 16 T dramatically. On

Parameter	Unit	18x90	20x90	23x90	23x90	23x90
DS Type	–	LHC	LHC	DS 2	DS 3	LHC
Cell Length	m	137.27	120.93	113.10	109.92	106.90
Dipoles per Cell	–	8	6	6	6	6
Dipole Length	m	13.95	16.17	14.86	14.34	13.83
Quad. Length	m	2.8	3.5	3.5	3.5	3.5
Quad. Strength for 13.5 TeV	T/m	336	306	328	328	348
Required field for 13.5 TeV	T	15.83	16.07	16.29	16.42	16.59
C.O.M. Energy with 16 T	TeV	27.28	26.86	26.50	26.30	26.01
Aperture at 450 GeV	σ	7.51	8.24	8.52	8.67	8.78

TABLE 5.1: Arc cell options for the HE-LHC, 18 cells - 23 cells.

Parameter	Unit	24x90	25x90	26x90	28x90	32x90
DS Type	–	DS 3	DS 3	DS 3	DS 3	DS 3
Cell Length	m	105.73	101.81	98.18	91.66	80.90
Dipoles per Cell	–	4	4	4	4	4
Dipole Length	m	21.19	20.22	19.31	17.68	14.99
Quad. Length	m	3.5	3.5	3.5	3.5	3.5
Quad. Strength for 13.5 TeV	T/m	351	365	379	407	463
Required field for 13.5 TeV	T	16.04	16.18	16.50	16.66	17.34
C.O.M. Energy with 16 T	TeV	26.90	26.60	26.28	25.91	24.90
Aperture at 450 GeV	σ	8.83	9.01	9.18	9.52	10.15

TABLE 5.2: Arc cell options for the HE-LHC, 24 cells - 32 cells.

the other hand, elements longer than about 20 m will cause transportation problems. During the design of the LHC the maximal transportable length was set to 15 m [72]. At the moment however, the maximal possible length is unclear and needs to be investigated.

5.1.1 Aperture

The aperture is calculated at 450 GeV using the existing beam screen version and misalignment tolerances, described in Section 3.3. 450 GeV refers to the injection energy provided by the SPS for the LHC, and which is targeted for the HE-LHC injection as well. Higher injection energies would require an upgrade of the SPS. Longer FODO cells have a negative impact on the beam stay clear, which is shown

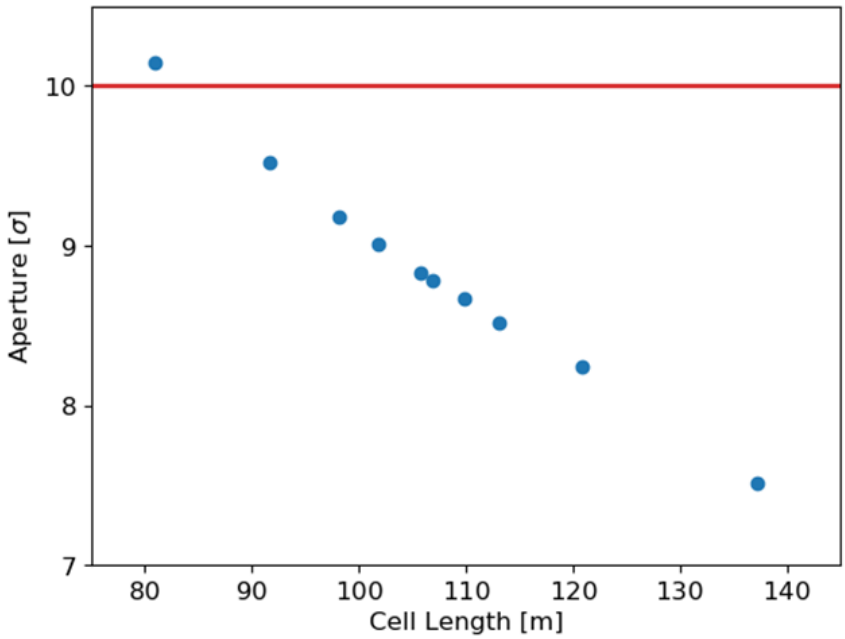

FIGURE 5.1: Aperture dependence on cell length at 450 GeV.

in Figure 5.1. Therefore the smallest aperture is located in the 18x90 lattice, with a value of 7.51 σ. It is possible to meet the target of 10 σ [69] beam stay clear by injecting at higher energy , enlarging the beam screen or choosing a design with 32 cells per arc [70]. The used beam screen design used in these studies is designed for the FCC-hh and therefore a new design could also be considered which fits the HE-LHC requirements.

These aperture results refer to the minimum beam stay clear in a FODO cell. The aperture bottlenecks are located where the optics functions have their maxima. In general, these peaks are located in the DS.

5.1.2 Energy Reach

The required dipole field for 13.5 TeV per beam, as well as the energy reach, are strongly correlated as described through equation (3.2). The highest energy reach of 27.28 TeV is achieved with the 18x90 HE-LHC design using a 15.83 T dipole field. Only this lattice meets the target of 27 TeV. The lowest energy reach of 24.90 TeV is reached using a 32x90 design. The energy reach of the lattice options in decreasing order are: 18x90, 24x90, 25x90, 20x90, 23x90 (DS 2), 23x90 (DS 3), 26x90, 23x90 (DS 1), 28x90 and 32x90 cells options.

With respect to a 23x90 arc design it can be seen that the integrated DS has a non-negligible impact on the energy reach. The smallest energy reach of 26 TeV is reached for a 23x90 design with integrated LHC DS. The highest centre of mass energy can be reached if the shortest DS, which is DS 2, is integrated.

The limit for the quadrupole gradient is currently 360 T/m [71]. This is exceeded in lattices with at least 25 cells per arc. In order to correct for these high gradients, the quadrupole lengths need to be increased. As the cell length cannot be made significanty longer, the extra space to correct the quadrupole gradients leads to a shortening of the dipoles, which in turn leads to a reduced centre of mass energy.

5.1.3 Geometry

Before studying the baseline lattices in detail, the main constraint, which is the tunnel geometry, has to be taken into account. The survey of every possible lattice design is generated and compared with the LHC. The LHC survey is taken as a representation of the tunnel geometry as the real tunnel data is not available. The transverse offset between the LHC and the HE-LHC lattices is calculated and plotted over the ring. This is shown in Figures 5.2 and 5.3.

The transverse offsets for the 20x90, 24x90 and 25x90 lattices are shown in the left plot of Figure 5.2. Using a 20x90 design leads to a maximal transverse offset of about 14 cm. The 24x90 and the 25x90 lattices have both a maximal offset of about 26 cm. In the right plot of Figure 5.2 the offset between the LHC and the 26x90, 28x90 and 32x90 HE-LHC lattices are shown, where the maximal offsets are 26 cm, 32 cm and 35 cm respectively.

In Figure 5.3 the transverse offsets between the LHC and the 18x90 lattice and the 23x90 lattices are shown. It can be seen that the integrated DS in the case of the 23x90 lattices, has a huge impact on the position of the elements and therefore on the offset to the LHC. These maximal transverse offsets vary from about 1 cm if the LHC DS is used, and above 40 cm if DS 2 is used. Using DS 3 the maximal transverse offset is approximately 28 cm. As the 23x90 design with LHC DS is the closest design compared to the LHC, this lattice option has as expected the least offset to the LHC. The 18x90 lattice has a maximal transverse offset of about 9 cm. The problem with large transverse offsets relative the LHC is that these lattices will not fit into the existing tunnel.

The maximal offset with respect to the LHC is located in the first regular cell which is part of the DS, independent of the lattice, as shown in Figure 5.3, where the lattice structure and the survey offset is shown simultaneously for the 18x90 and the 23x90 with integrated LHC DS. The dipoles and quadrupoles of the lattice are illustrated as orange and blue bars respectively. One possible mitigation attempt is to add one extra dipole in the drift space of the DS. These additional 16 dipoles can be of different type than the arc dipoles. Moreover it is possible to relax the constraint on the difference between all $\mathrm{IPs}_{\mathrm{HE\text{-}LHC}}$ and $\mathrm{IPs}_{\mathrm{LHC}}$, which is currently set below 1 cm. Relaxing the offset in the IPs is a possible solution to reduce the offset in the DS.

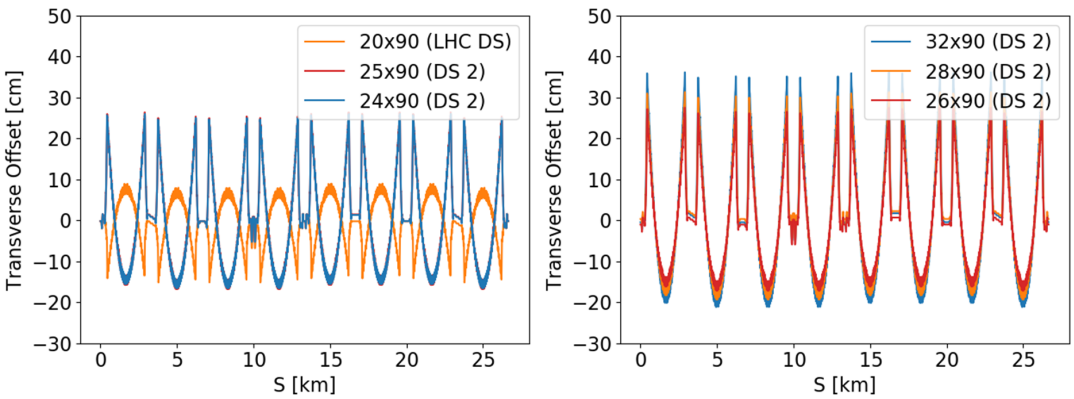

FIGURE 5.2: Transverse offset between LHC and the 20x90, 24x90, 25x90, 26x90, 28x90 and 32x90 HE-LHC options.

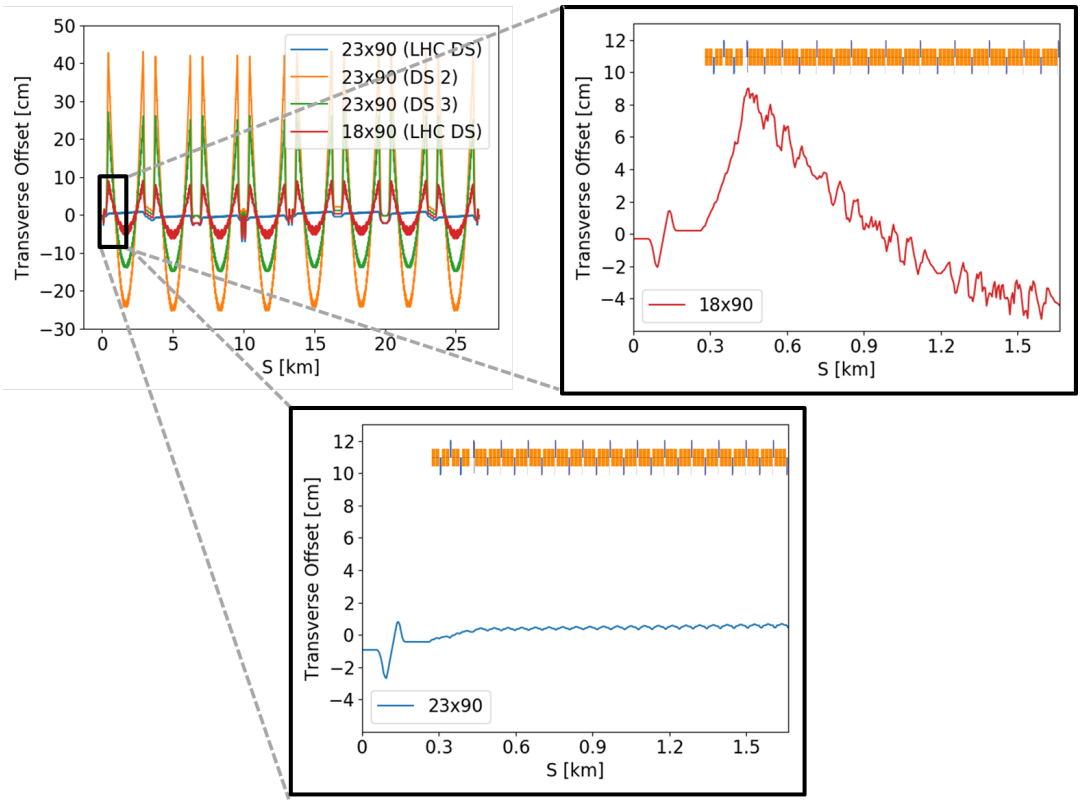

FIGURE 5.3: Transverse offset between LHC and the 23x90 and 18x90 HE-LHC options. The offset of the 18x90 and 23x90 with integrated LHC DS is zoomed for a half arc where the lattice is plotted as well. The dipoles and the quadrupoles are illustrated as orange and blue bars respectively.

The maximal possible offset compared to the LHC is assumed to be in the order of several cm [73]. This probably leads to the exclusion of lattices with a transverse offset above 10 cm. Assuming these tolerances one can conclude that only the 18x90 and the 23x90 with integrated LHC DS have an acceptable maximal offset relative to the LHC.

To conclude, a suitable arc cell and DS design for the HE-LHC results in a trade off between the offset to the LHC, energy reach and beam stay clear. With respect to these parameters, the 18x90 and the 23x90 arc design with integrated LHC DS are chosen for further study.

5.2 Baseline Lattices

At this design stage the 18x90 and 23x90 arc designs with integrated LHC DS are the best candidates for the HE-LHC. Therefore the optics for these lattices are matched

and further analysed. The optics parameters for these options are summarised in Tables 5.3 and 5.4. Both options are matched to a phase advance per cell of 90° in both planes. In order to fit the latest requirements, the beam separation 2018 is chosen for these designs (see Table 4.3). The layout of a cell is similar to the LHC cell which is shown in Figure 3.17.

For the latest version of the baseline lattices DS 1, instead of the LHC DS is integrated, as a using longer dipoles in the DS neighbouring IR1 and IR5 is found to be required in order to guarantee flexible optics matching [68]. In order to minimise the transverse offset, the ALGEA survey fitting algorithm is used. Due to a different DS, compared to Section 5.1, the cell length and the dipole length have changed for the 18x90 arc design. Using DS 1 with beam separation of 2018, instead of using the LHC DS with beam separation of 2017, leads to longer cells (137.33 m instead of 137.27 m) with shorter dipoles (13.94 m instead of 13.95 m). The differences between the LHC DS and DS 1 are negligible and have no significant impact on the survey.

The filling factor indicates how much space in a cell is filled with dipoles. The 18 cells design has a filling factor of 0.81 which is higher compared to 0.78 for the 23 cells design. To meet the target energy of 27 TeV the dipole field needs to be 15.85 T or 16.59 T for the 18 or 23 cells designs respectively. As the dipoles are responsible for the energy reach, only the 18 cells design meets the target energy of 27 TeV. A 23 cells design limits the centre of mass energy to about 26 TeV.

Quadrupole lengths are chosen to not exceed the gradient limit of 360 T/m [71]. The quadrupoles need to provide a gradient of about 335 T/m in both options. A 18 cells design requires smaller quadrupoles of 2.8 m compared to 3.5 m needed for the 23 cells design.

Cell Parameter	Unit	18x90	23x90
Phase Advance per Cell	°	90	90
Cell Length	m	137.33	106.9
Dipoles per Cell	–	8	6
Dipole Length	m	13.94	13.83
Bending Angle per Dipole	°	0.28	0.29
Filling Factor	–	0.81	0.78
Quadrupole Length	m	2.8	3.5
Quadrupole Strength	T/m	336	335
β_{max}/β_{min}	m	230/40	177/32
D_{max}/D_{min}	m	3.60/1.76	2.20/1.10
Aperture at 450 GeV	σ	7.51	8.78

TABLE 5.3: HE-LHC cell parameters for the 18x90 and the 23x90 lattice.

Ring Parameter	Unit	18x90	23x90
DS Type	–	DS 1	DS 1
Injection Energy	GeV	450	450
Required field for 13.5 TeV	T	15.85	16.59
c.o.m. Energy with 16 T Dipoles	TeV	27.24	26.01
Natural Horizontal Chromaticity at Inj. Energy	–	−70.72	−84.26
Natural Vertical Chromaticity at Inj. Energy	–	−72.62	−84.39
Natural Horizontal Chromaticity at Coll. Energy	–	−180.33	−192.98
Natural Vertical Chromaticity at Coll. Energy	–	−182.50	−184.94
Momentum Compaction	10^{-4}	5.84	3.54
Transition Energy	GeV	41.38	53.14
Horizontal Tune at Injection	–	50.28	62.28
Vertical Tune at Injection	–	48.31	59.31
Horizontal Tune at Collision	–	50.31	62.31
Vertical Tune at Collision	–	48.32	59.32
Horizontal IBS Growth Time at Inj. Energy	h	4.1	6.5
Longitudinal IBS Growth Time at Inj. Energy	h	4.1	3.3
Horizontal IBS Growth Time at Coll. Energy	h	22.7	30.6
Longitudinal IBS Growth Time at Coll. Energy	h	79.4	54.6

TABLE 5.4: HE-LHC ring parameters for the 18x90 and the 23x90 lattice.

The maxima of the beta functions and dispersion function depend on the cell length. As longer cells have higher optics functions the 18 cells design with a cell length of 137.33 m has a maximal beta function and dispersion function of 230 m and 3.6 m, whereas these optics functions reach only 177 m and 2.2 m for the 23 cells design respectively.

The natural chromaticity is smaller for the 18x90 lattice at injection and collision energy. At injection energy, it is about −72 for the 18 cells design and about −84 for the 23 cells design. At collision energy the natural chromaticities decrease to about −180 and −190 for the 18 and the 23 cells designs.

The momentum compaction of 5.84×10^{-4} is higher for a 18 cells design than 3.54×10^{-4} for a 23 cells design. Equation (3.33) shows that the transition energy is higher for smaller momentum compaction, namely 41.38 GeV or 53.14 GeV for the 18 or 23 cells design. The injection energy provided by the SPS is 450 GeV, which is above transition energy in both designs and therefore the synchronous phase remains unchanged over the acceleration process.

In the case of the 23 cells design the transverse integer tunes are $Q_x = 62$, $Q_y = 59$. This is larger than for the 18 cells design, where $Q_x = 50$, $Q_y = 48$. The fractional tunes are matched to the LHC working point at injection and collision.

Parameter	Unit	Injection	Collision
Normalised Emittance	μm	2.5	2.5
Protons per Bunch	10^{11}	2.2	2.2
Energy Spread $\Delta E/E$	10^{-4}	3.2	1.1
Longitudinal Bunch Length	cm	9.00	7.55

TABLE 5.5: Beam parameters at injection and collision energy, used for calculation of the intrabeam scattering calculations.

To calculate the intrabeam scattering growth times, the beam parameters have to be set properly. The beam properties used are summarised in Table 5.5 for injection and collision energy. At injection energy the horizontal (longitudinal) growth time for the 18x90 and 23x90 design is 4.1 h (4.1 h) and 6.5 h (3.3 h) respectively and 22.7 h (79.4 h) and 30.6 h (54.6 h) at collision energy. As these growth times at collision energy are greater than the fill time, the emittance growth due to intrabeam scattering is negligible. At injection energy however, these effects become non-negligible if the time the operating at this energy is in the same order of magnitude as the IBS growth times.

In addition to optics and design parameters, the calculated aperture per cell at 450 GeV injection energy is given in Table 5.3. 450 GeV is currently the maximal possible injection energy from the SPS. For a robust beam operation an aperture of 12 σ is targeted for the HL-LHC [74]. The goal for the HE-LHC is set to 10 σ [69],

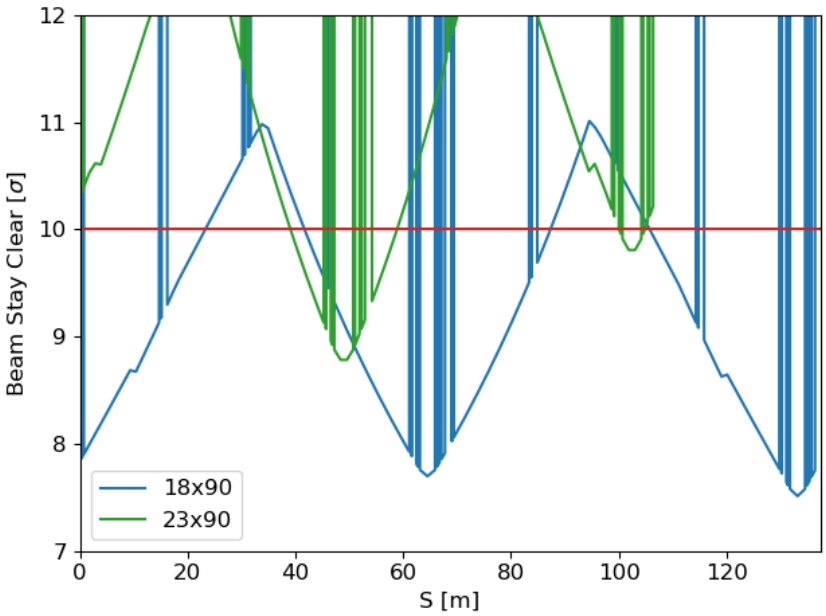

FIGURE 5.4: Minimum beam stay clear along a FODO cell of the HE-LHC 18x90 and 23x90 lattice at 450 GeV.

which is not achieved with 450 GeV injection energy as seen in Figure 5.4. The smallest beam stay clear is located at the quadrupoles as there the optics functions are at their maxima.

It is possible to meet the target of $10\,\sigma$ by injecting at higher energy. For the 18x90 lattice an injection energy of about 800 GeV is sufficient to meet the aperture goal, where about 600 GeV is enough for the 23x90 lattice [70] as shown in Figure 5.5. About 600 GeV can be achieved by the SPS if half of the normal conduncting magnets are replaced by superconducting ones [13].

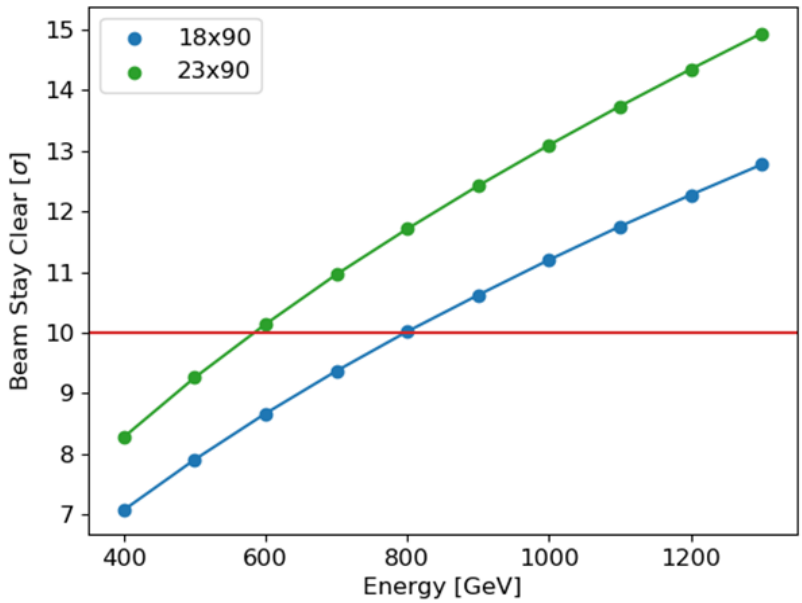

FIGURE 5.5: Beam stay clear dependence on the injection energy for the 18x90 and the 23x90 lattice.

Chapter 6

Studies at Injection Energy

At injection energy the main problem is reaching a sufficient beam stay clear. For the HE-LHC 10 σ aperture are targeted, which is not reached in the baseline FODO cells as shown in Chapter 5. The bottlenecks are found and solutions are given. All studies are performed at 450 GeV injection energy using the beam screen and the misalignment tolerances introduced in Section 3.3. 450 GeV injection energy is currently provided by the SPS, whereas higher injection energies require an upgrade.

6.1 Aperture of the Ring

The optics and the aperture for both beams for the 18x90 and the 23x90 lattice are given in Figures 6.1 and 6.2. IP1 is located at s = 0 m, for the baseline lattices using the beam separation of 2018. The smallest apertures in all dispersion suppressors as well as the aperture of a FODO cell are summarised in Table 6.1. The dispersion suppressors neighbouring IR1 are not included as the optics and therefore the aperture are identical for IR5 and IR1. Plots of the IRs can be found in Appendix A.

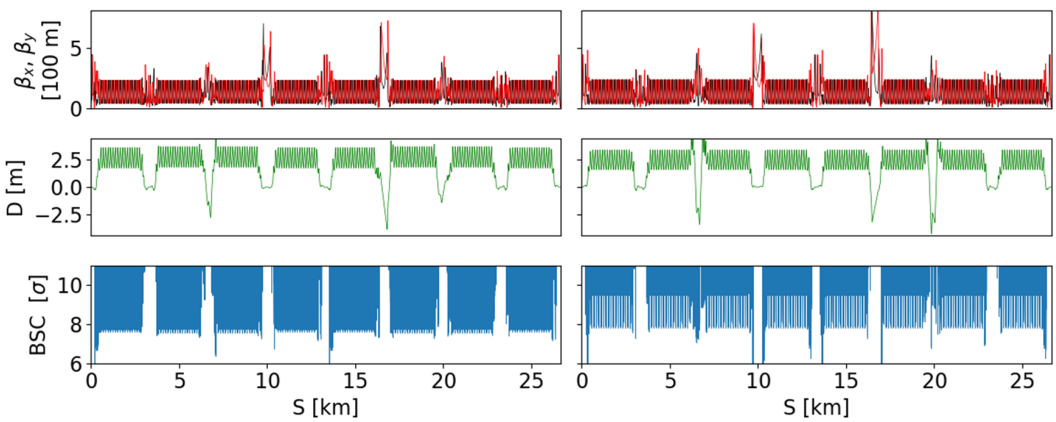

FIGURE 6.1: Beta functions, horizontal dispersion function and beam stay clear (BSC) for beam 1 (left) and beam 2 (right) for the 18x90 design at 450 GeV injection energy.

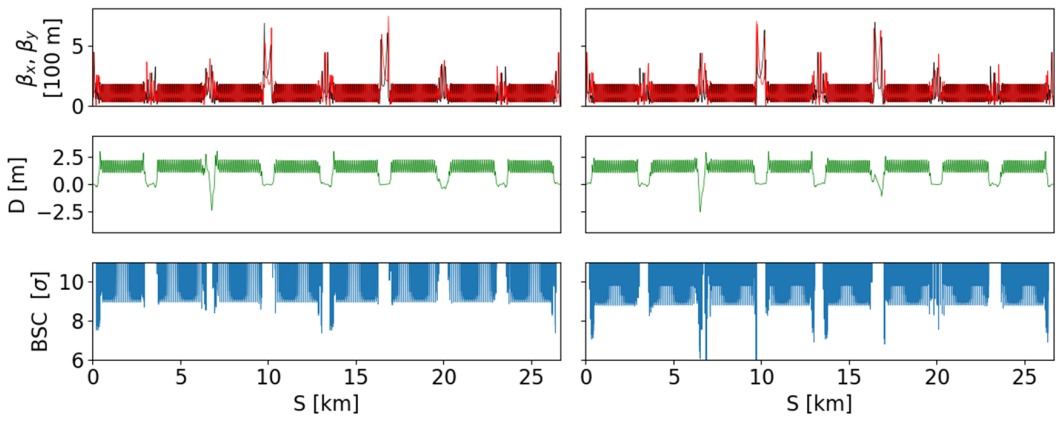

FIGURE 6.2: Beta functions, horizontal dispersion function and beam stay clear (BSC) for beam 1 (left) and beam 2 (right) for the 23x90 design at 450 GeV injection energy.

The cell length depends on the number of cells per arc. A design with more cells per arc requires smaller cells with, in general, fewer dipoles. Shorter cells have smaller beta functions and dispersion which can be seen by compaing Figures 6.1 and 6.2. As the aperture depends on the optics, approximated via equation (3.46), the 23 cells option has a larger beam stay clear as the optics functions are smaller, compared to the 18 cells design in the arcs, namely 8.78 σ compared to 7.51 σ, which is below the target of 10 σ [69].

While the optics functions are nearly identical over all arcs, peaks of the beta functions and the dispersion are located in the dispersion suppressors. In order to fulfill the optics requirements in the IR, the optics functions in the DS do not remain periodically which leads to these peaks, where the beam stay clear minima are located. In the case of the 18x90 lattice beam 1 the smallest beam stay clear is located in the DS right fom IP3 of about 6.35 σ, which is 1.16 σ smaller compared to the arcs. The minimum beam stay clear of 5.37 σ is located in the DS left from IP4 for beam 2 in the 18x90 lattice. Regarding the 23x90 design, the minimum beam stay clear of 7.51 σ for beam 1 is found to be in the DS right from IP5. The minimum beam stay clear in the 23x90 design for beam 2 is located in the DS left from IP4 of 5.26 σ. In some dispersion suppressors however, the minimum beam stay clear is not smaller than in the arc as the optics functions have no peaks there.

In both lattices the beam stay clear has one significant minimum in the dispersion suppressors neighbouriging IP5. This major decrease in aperture results from the required dispersion peak, which is located in the DS right from IP5 for beam 1, and in the DS left from IP5 for beam 2. Especially in the 23x90 lattice the location of the dispersion peak, left or right from the IP, coincides with the side of the smallest aperture.

Table 6.1 summarises only the minimum beam stay clear in the dispersion suppressors. In the presented optics however, the minimum aperture is loacted in IR3 for both beams in both lattices. Moreover the beam stay clear is smaller for beam 2 compared to beam 1 in this IR. Currently the IR3 optics from the LHC is used. Investigations for a suitable IR3 design which fulfils the HE-LHC requirements are ongoing [75].

The aperture for beam 1 is not exactly the same as for beam 2. This is the result of the asymmetric IR and ring design. In general, more minima of the aperture occur in beam 2 for both lattices.

In order to guarantee a stable beam the target of $10\,\sigma$ needs to be met over the ring and therefore the current aperture minima in the dispersion suppressors need to be improved. One attempt to mitigate these aperture bottlenecks is rematching the optics to minimise the optics peaks. In order to overcome the differences between beam 1 and beam 2 a more symmetric design of the IRs can be considered. A major redesign of the DS is not possible due to the negative effect on the survey.

DS Location	Minimum Aperture [σ]			
	18x90		23x90	
	Beam 1	Beam 2	Beam 1	Beam 2
Cell	7.51		8.78	
L. IP2	7.55	7.27	8.69	8.82
R. IP2	7.40	7.60	8.83	8.25
L. IP3	7.40	7.72	8.63	8.88
R. IP3	6.35	7.57	8.38	8.10
L. IP4	7.40	5.37	8.58	5.26
R. IP4	6.72	5.75	8.40	8.27
L. IP5	7.15	6.24	7.71	6.90
R. IP5	6.64	5.46	7.51	7.05
L. IP6	7.31	7.25	8.85	8.59
R. IP6	7.31	5.39	8.80	6.79
L. IP7	7.27	8.15	8.94	8.34
R. IP7	7.38	7.52	8.89	8.27
L. IP8	7.42	6.89	8.94	8.75
R. IP8	7.39	7.53	8.87	8.64

TABLE 6.1: Minimum apertures in the dispresion suppressors left (L) and (R) from all IPs at 450 GeV injection energy for the 18x90 and the 23x90 design for both beams.

6.2 Aperture Dependence on Phase Advance

Until now the FODO cells are matched to $\mu_x, \mu_y = 0.25 \times 2\pi$ phase advance which is beneficial for corrections and chromatic errors [76]. As the aperture depends not only on the optics but also on the phase advance, studies to enlarge the aperture by matching the cells to a different phase advance have been performed. For these studies only one FODO cell for beam 1 is matched and analysed for the 18x90 and the 23x90 design with the LHC DS using the 2017 beam separation. These cells are used for the following sections in this chapter.

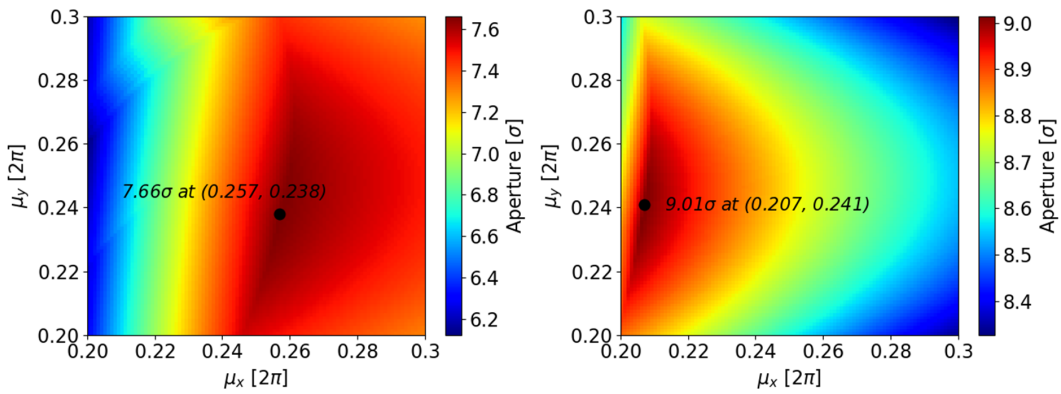

FIGURE 6.3: Aperture dependence on horizontal and vertical phase advance in case of a 18 (left) and a 23 (right) cells designs at 450 GeV.

In Figure 6.3 the dependence of the aperture on the phase advance at 450 GeV is shown. The optimal phase advance is found at $\mu_x = 0.257 \times 2\pi$, $\mu_y = 0.238 \times 2\pi$ for the 18 arc cells design which results in an aperture of $7.66\,\sigma$. Optimal phase advances for the 23 arc cell design are found to be at $\mu_x = 0.207 \times 2\pi$, $\mu_y = 0.241 \times 2\pi$ giving an aperture of $9.01\,\sigma$. The optimal phase advances improve the aperture by about $0.15\,\sigma$ or $0.23\,\sigma$ for the 18 or 23 cells designs.

The phase advance does not only have influence on the aperture, but also on the dynamic aperture which is reduced by resonance driving terms in the lattice. One attempt to mitigate these driving terms is to design a so called *resonance free lattice* [77]. This can be achieved by matching the horizontal and the vertical phase advance in a way that

$$k_1 n_x + k_2 n_y = k N_c \quad \text{with} \quad k_1 \neq k_2 \tag{6.1}$$

is fulfilled, where k_1, k_2, k, n_x and $n_y \in \mathbb{N}$ and N_c is the number of cells (FODO cells plus two irregular DS cells) per arc. The constants k_1 and k_2 define the order of the

resonance which is cancelled whereas n_x, n_y are related to the phase advances by

$$\mu_x = \frac{n_x}{N_c} 2\pi \quad \text{and} \quad \mu_y = \frac{n_y}{N_c} 2\pi \,. \tag{6.2}$$

Before studying the efficiency of a resonance free design on the dynamic aperture, it is essential to study the effect on the beam stay clear. Therefore, the required phase advances for the two cell options and the resulting aperture are summarised in Table 6.2.

18 Regular Arc Cells $N_c = 20$					23 Regular Arc Cells $N_c = 25$				
n_x	n_y	μ_x	μ_y	Aperture [σ]	n_x	n_y	μ_x	μ_y	Aperture [σ]
–	–	90.0	90.0	7.51	–	–	90.0	90.0	8.78
5	4	90.0	72.0	7.53	6	5	86.4	72.0	8.65
4	5	72.0	90.0	6.16	5	6	72.0	86.4	8.82
6	4	108.0	72.0	7.31	7	5	100.8	72.0	8.43
4	6	72.0	108.0	6.18	5	7	72.0	100.8	8.65
6	5	108.0	90.0	7.49	7	6	100.8	86.4	8.63
5	6	90.0	108.0	7.34	6	7	86.4	100.8	8.74

TABLE 6.2: Phase advances and the resulting aperture for resonance free lattices for the 18 and the 23 cells design of the HE-LHC at 450 GeV injection energy.

In the case of the 18 cells design a larger horizontal than vertical phase advance is found to have a positive effect on the beam stay clear compared to a larger vertical than horizontal phase advance. The only increased beam stay clear with respect to the baseline, where $\mu_x, \mu_y = 90°$, however, is found at $\mu_x = 90°$, $\mu_y = 72°$. Matching the cells to these phase advances increases the beam stay clear by $0.02\,\sigma$ to $7.53\,\sigma$. All other resonance free options decrease the beam stay clear compared to the baseline.

Contrarily to the 18 cells design, a larger vertical than horizontal phase advance results in a larger beam stay clear compared to a larger horizontal than vertical phase advance. Matching the 23x90 cells to 72.0° horizontal and 86.4° vertical phase advance improves the aperture by $0.04\,\sigma$ compared to the nominal design where both phase advances are matched to 90°. Using $\mu_x = 72.0°$, $\mu_y = 86.4°$ results in $8.82\,\sigma$ beam stay clear.

Even though the beam stay clear improves by only $0.02\,\sigma$ or $0.04\,\sigma$ in case of the 18 or 23 cells designs, studies [78, 79] have shown that a resonance free lattice created improves the dynamic aperture. With respect to latest results [80] the dynamic aperture including all arc dipole errors at 450 GeV is $1.7\,\sigma$ in the 18x90 lattice and $2.8\,\sigma$ in a 23x90 design, which is not sufficient. A possible solution can be a resoncance free lattice where the cells are matched to the phase advances found in this study.

Regarding the beam stay clear, phase advances are found which have a positive impact. Due to the promising results for one cell, matching resonance free lattices need to be further investigated.

6.3 Combined Function Dipoles

Dipoles are named *combined function dipoles* if they provide an additional quadrupole field. Combined function dipoles are used in for example the Proton Synchrotron (PS) at CERN [81]. The current dipole design has a negligible quadrupole component at injection energy of ± 2.23 units. Moreover this study assumes the feasibility of two different dipole types. The effect of dipoles with controlled quadrupole field on the aperture is discussed here to explore ways to improve the physical aperture.

Similar to b_2 errors the sign of the additional quadrupole field per dipole can be positive or negative depending if the beam travels in an inner or an outer arc. This means, if a certain combination of quadrupole fields is beneficial in an inner cell, the aperture in a cell located in an outer arc can be worse. Therefore the effect of these additional fields has to be considered simultaneously in inner and outer arcs. Quadrupole fields of ± 50 to ± 500 units are applied to every dipole in a cell separately. This means that in one cell each dipole can either provide positive or a negative additional quadrupole component. An example for combining additional quadrupole fields in the dipoles is given in Figure 6.4 for FODO cells with six (left) or eight (right) dipoles. The dipoles or quadrupoles are illustrated as orange or blue bars respectively, where a defocusing quadrupole is located negatively in an imaginary vertical axis. Table 6.3 summarises the results for these combined function dipoles at 450 GeV. The cells are matched to 90° phase advance in both transverse

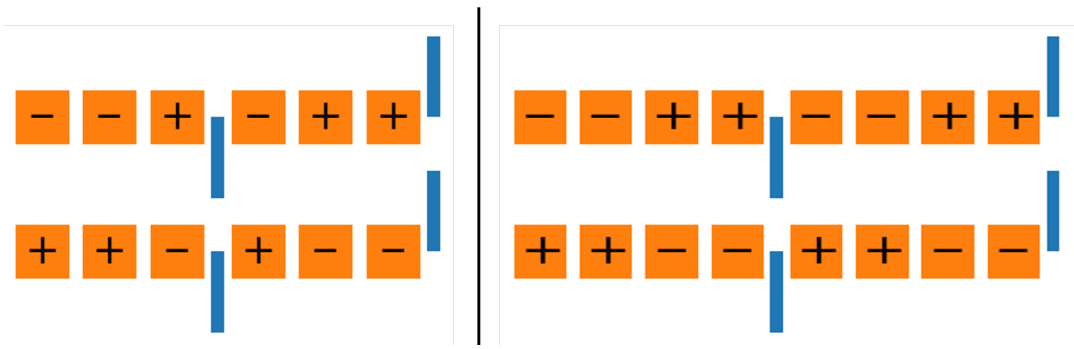

FIGURE 6.4: Example of combined function dipoles in two FODO cells, for an inner (top) and the resulting outer (bottom) aperture. These combinations of additional quadrupole fields in the dipoles of 450 units in case of the 23x90 lattice (left) and of 500 units in case of the 18x90 lattice (right) are illustrated.

Quadrupole Field [10^{-4}]	Aperture [σ]			
	18x90		23x90	
	Inner Arc	Outer Arc	Inner Arc	Outer Arc
0	7.31	7.31	8.78	8.78
50	7.56	7.56	8.79	8.79
100	7.70	7.70	8.86	8.86
150	7.94	7.94	8.96	8.96
200	8.11	8.11	9.13	9.13
250	8.36	8.36	9.60	9.35
300	8.73	8.73	9.39	9.36
350	8.62	8.62	9.60	9.45
400	8.80	8.80	9.89	9.71
450	8.92	8.99	9.82	9.82
500	9.53	9.62	9.44	9.44

TABLE 6.3: Resulting aperture when using combined function dipoles at 450 GeV with 90° phase advance in both transverse planes. The quadrupole component is applied in each dipole seperately and changes sign from an inner to an outer arc.

planes. A plot of the results is shown in Figure 6.5.

The optimal additional quadrupole field in the dipoles, with respect to inner and outer arcs, is found at 400 units to 450 units for the 23x90 lattice, where three quadrupole components are positive and negative respectively. The location of the

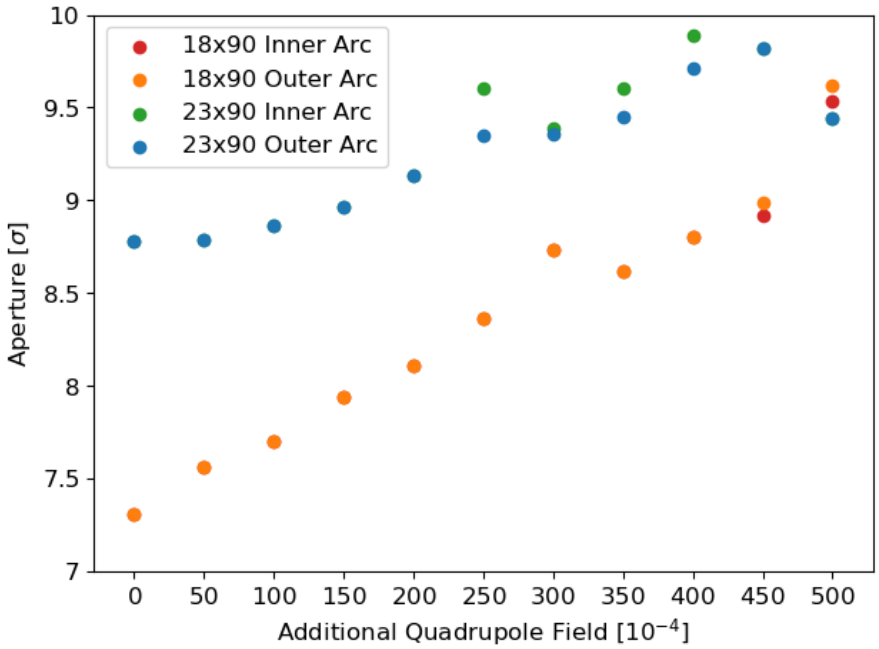

FIGURE 6.5: Aperture results for combined function dipoles.

positve and negative additional quadrupole fields is shown in the left plot of Figure 6.4 for 450 units. Applying quadrupole fields lower than 400 units leads to a significant decrease of the beam stay clear. With 500 units of additional quadrupole fields the aperture decreases again.

Using the 18x90 design, the beam stay clear improves monotonically with higher additional quadrupole fields. Therefore it is benefical for the beam stay clear to apply high additional quadrupole fields. If applying 500 units, the best combination in an inner and outer arc is shown in the right plot of Figure 6.4.

In case of the 23x90 design, the resulting beam stay clear while applying additional quadrupole components in the dipoles is identical for the inner and outer aperture up to 200 units. For the 18x90 design this limit is at 400 units. After this limit the quadrupole fields of the dipoles improve one beam stay clear more than the other.

Identical quadrupole components in a cell, meaning only positive or negative in the same aperture, do not have a positive effect on the beam stay clear. Especially quadrupole fields higher than 150 units defocuse the beam in a way that the beam stay clear equals zero.

6.4 Combined Function Dipoles at Optimal Phase Advance

In the previous Section 6.3 it was assumed that two different dipole types would be used in order to apply positve and negative quadrupole fields in one cell. In this section, however, the same additional quadrupole field in all dipoles in a cell located in an inner arc or outer arc is assumed. Quadrupole field components from -100×10^{-4} to $+100 \times 10^{4}$ are analysed. A smaller range compared to the previous section is chosen, because applying same signed quadrupole fields in the same cell above 100 units leads to $0\,\sigma$ beam stay clear.

In Section 6.2 it is presented that the phase advance has a non-negligible impact on the aperture. The same study is now performed using combined function dipoles. 90° is chosen as the average phase advance in both planes. A considered constraint is that the phase advance over the whole ring is unchanged. This means if $\mu_x = x$ in an inner arc with only positive quadrupole fields (for example $b_2 = +10 \times 10^{-4}$), $\mu_x = \pi - x$ in the outer arc with only negative quadrupole fields (for example $b_2 = -10 \times 10^{-4}$), respectively for μ_y.

Table 6.4 summarises the best aperture while taking into account the phase advance as well as the quadrupole field constraint from one arc to another. Applying an identical quadrupole component to all dipoles in a cell reduces the beam stay clear in one

arc while enlarging it in the other. The most beneficial quadrupole component and phase advance, however, is found to be $\pm$ 26 units in the case of a 18 cells design and $\pm$ 77 units for a 23 cells design. This results in minimum aperture of $6.74\,\sigma$ or $8.61\,\sigma$ respectively. Even though increasing the beam stay clear by $0.23\,\sigma$ or $0.36\,\sigma$ in the outer arc, only the smallest aperture is significant as the target of $10\,\sigma$ has to be met over the full ring. With respect to baseline designs, where split-function magnets are used, no beam stay clear enlargement is found.

	18 Cells			23 Cells		
	Inner Arc	Outer Arc	BL	Inner Arc	Outer Arc	BL
b_2 [10^{-4}]	+ 26	- 26	0	+ 77	- 77	0
μ_x [2π]	0.21	0.29	0.25	0.20	0.30	0.25
μ_y [2π]	0.28	0.22	0.25	0.25	0.25	0.25
Aperture [σ]	6.74	7.74	7.51	8.61	9.14	8.78

TABLE 6.4: Resulting aperture by varying the phase advance using combined function dipoles, compared to the baseline (BL) at 90° phase advance in both planes using split function dipoles.

Chapter 7

Studies at Collision Energy

At collision energy the quadrupole errors in the main dipoles are no longer negligible. Contrary to injection energy, the beam stay clear at collision energy is sufficient due to a smaller emittance and not affected by these errors. However, other consequences of present quadrupole errors are studied.

For these studies the 18x90 and 23x90 arc designs with integrated LHC DS using beam separation 2017 are used, as the errors introduced in Section 3.6 refer to the 2017 beam separation.

7.1 Effect of Quadrupole Errors

Theory

Dipoles with an additional systematic b_2 component have a focusing effect which needs to be corrected with the quadrupoles in the cell. The quadrupole component in all cell dipoles needs to be compensated with all cell quadrupoles which leads to

$$\sum_{MB} L_{MB}\, k_{MB}\, \beta_{z,MB} \;=\; \sum_{MQ} L_{MQ}\, \Delta k_{MQ}\, \beta_{z,MQ}\,, \tag{7.1}$$

where z is one of the transverse coordinates x or y, L_{MB} and L_{MQ} refer to the dipole and quadrupole lengths respectively, k_{MB} is the additional quadrupole field provided by one dipole due to the systematic b_2 error and $\beta_{z,MB}$ and $\beta_{z,MQ}$ refer to the beta functions at the centre of a dipole and quadrupole respectively in an error free FODO cell. Δk_{MQ} refers to the additional required quadrupole gradients due to present b_2 errors. As one cell contains only one focusing and one defocusing quadrupole, equation (7.1) splits and simplifies to

$$\Delta k_{MQF} \;=\; \frac{\sum_{MB}\, k_{MB}\, L_{MB}\, \beta_{x,MB}}{L_{MQ}\, \beta_{x,MQ}}\,, \qquad \Delta k_{MQD} \;=\; \frac{\sum_{MB}\, k_{MB}\, L_{MB}\, \beta_{y,MB}}{L_{MQ}\, \beta_{y,MQ}}\,. \tag{7.2}$$

As the HE-LHC FODO cells are symmetric it follows that $\Delta k_{MQF} = -\Delta k_{MQD}$. This means that with present b_2 errors the focusing quadrupole gradient needs to be increased while the defocusing quadrupole gradient decreases. The quadrupole component per dipole k_{MB} is given as [65]

$$k_{MB} = \theta \frac{b_2}{R_{ref}} \tag{7.3}$$

with the bending angle per dipole θ and the b_2 at a reference radius R_{ref}.

From equations (7.2) it can be seen that the required additional quadrupole gradient increases linearly with increasing b_2 error. In case of the HE-LHC the present b_2 errors are ± 46.84 units in the dipoles at a reference radius at 16.7 mm.

MAD-X Computation

Systematic quadrupole errors in the arc dipoles result in stronger main quadrupole gradients. The quadrupoles need to compensate for the focusing effect induced by quadrupole errors in the dipoles. Depending on the sign of the errors either the horizontal or the vertical focusing quadrupole strength has to be increased. The feasible quadrupole gradient is set to 360 T/m which cannot be exceeded.

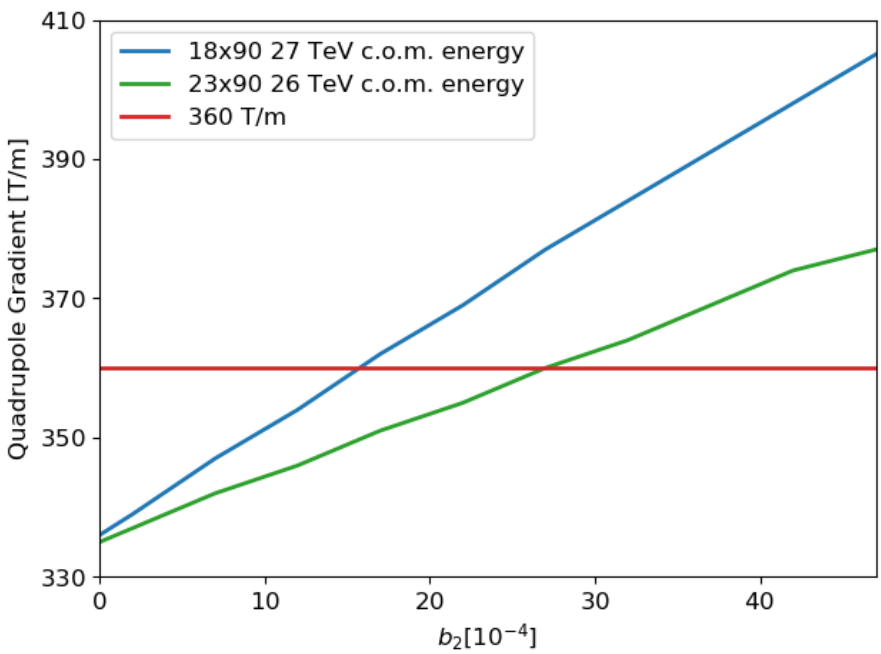

FIGURE 7.1: Effect of quadrupole errors in the arc dipoles for 18x90 and 23x90 arc designs.

In Figure 7.1 the required quadrupole gradient versus present quadrupole error is shown. The required field increases almost linearly with the errors. These errors have a larger impact on the 18x90 lattice as there one cell contains eight dipoles wheras a FODO cell in case of the 23x90 lattice is made of only six dipoles. Additionally, the dipole filling factor is higher in a 18 cells design than in the 23 cells design, which increases the impact of the errors in the dipoles.

The quadrupoles used in the 23x90 lattice are longer, namely 3.5 m instead of 2.8 m as in case of the 18x90 lattice. Due to longer quadrupoles the 23x90 lattice can accommodate larger b_2 errors before the gradient of the main quadrupoles is exceeded.

Currently ± 46.84 units of systematic normal quadrupole errors at collision energy are expected from the dipole design [66]. The needed quadrupole gradients to correct these errors are summarised in Table 7.1. Depending on the sign either the horizontally focusing or defocusing quadrupole gradient increases in order to correct for the b_2 errors in the dipoles. In case of the 23x90 lattice a quadrupole gradient of 377 T/m needs to be provided. For the 18x90 lattice the required gradient is 405 T/m. In both lattices the quadrupoles exceed their limits.

To summarise, quadrupole errors of 27 units in the arc dipoles can be corrected without lengthening of the quadrupoles in case of the 23x90 design. On the other hand, the 18 cells design can only handle up to 16 units. The required quadrupole enlargement is studied in the next section.

b_2 [10^{-4}]	Quadrupole Gradient [T/m]	
	18x90 27 TeV Collision Energy	23x90 26 TeV Collision Energy
0	336	335
$\pm$ 46.84	405	377

TABLE 7.1: Required quadrupole gradient with present quadrupole errors in the dipoles.

7.2 Correction of Quadrupole Errors

In order to not exceed the feasible gradient field of 360 T/m the quadrupole length needs to be lengthened. The required quadrupole lenghts as well as the resulting parameters are summarised in Table 7.2.

The quadrupoles in the 18x90 lattice need to be lengthened by 0.35 m, but only by 0.17 m in the 23x90 lattice in order to correct for the expected ± 46.84 units of b_2 error.

In the 23 cells design the additional 0.17 m per quadrupole leads to a reduction of the dipole length to 13.77 m. As the energy reach depends strongly on the dipoles installed in the FODO cells, this shortening leads to a 0.11 TeV lower center of mass energy of 25.90 TeV with respect to a b_2 error free lattice. Regarding the 18x90 design the quadrupoles can be enlarged without shortening the dipoles as additional drift spaces are located in the FODO cell. As a result the center of mass energy remains unchanged at 27.24 TeV.

In order to not decrease the energy reach in the 23x90 design the quadrupole errors in the dipoles need to be reduced below 27 units. The enlargement of the quadrupoles in the 18x90 design does not have any impact on the energy reach.

		18x90	23x90
Quadrupole Gradient [T/m]	Uncorrected	405	377
	Corrected	360	360
Quadrupole Length [m]	Uncorrected	2.8	3.5
	Corrected	3.15	3.67
Dipole Length [m]	Uncorrected	13.94	13.83
	Corrected	13.94	13.77
c.o.m. Energy [TeV]	Uncorrected	27.24	26.01
	Corrected	27.24	25.90

TABLE 7.2: Parameters before and after correction of quadrupole errors in the dipoles.

Chapter 8

Performance

The evolution of beam parameters over a physics fill are studied. The baseline scenario as well as alternative performance options are presented. Time $t = 0$ indicates the start of proton-proton collisions. In all scenarios the beam is assumed to have a Gaussian charge distribution. These results are simulated by a PYTHON routine, which is used to simulate HL-LHC physics fill as well [44, 82, 83, 84], based on the original code implemented in [85].

In this routine, the beam intensity evolution is evaluated considering proton burn-off with a total cross-section of 126 mb [26] at collision energies of 27 TeV and 26 TeV. The emittance evolution takes intrabeam scattering and synchrotron radiation damping into account. The luminous region is derived including crab cavity RF curvature [86]. Time pile-up and line pile-up densities are evaluted exactly at the interaction point. The longitudinal bunch length σ_s is kept constant at 7.55 cm. Crab cavities compensate the full crossing angle of 330 µrad, which is kept constant over the entire fill.

8.1 Baseline

The performance at 27 TeV and 26 TeV centre of mass energies are shown in Figure 8.1. All results are summarised in Table 8.1. The beta function β^* at the collision point, is constant at 45 cm.

With 2.2×10^{11} protons per bunch (ppb) the initial instantaneous luminosity $\mathcal{L}$ equals $15 \times 10^{34}\,\mathrm{cm}^{-2}\mathrm{s}^{-1}$ or $14 \times 10^{34}\,\mathrm{cm}^{-2}\mathrm{s}^{-1}$ for 27 TeV or 26 TeV centre of mass energy. The number of events per bunch crossing (pile-up μ) is initially 430 or 410. As the beams collide the protons burn off which leads to a decay of the instantaneous luminosity, the pile-up and the proton bunch population. The line pile-up and time pile-up densities, ϱ_s and ϱ_t show an identical behaviour over time. At time $t = 0$, about 3.3 events per mm as well as about 980 to 945 events per ns occur, the higher value refering to the higher centre of mass energy of 27 TeV. At the end of the fill, where $t = 5.25$ h or $t = 5.39$ h one bunch contains only about 0.7×10^{11}

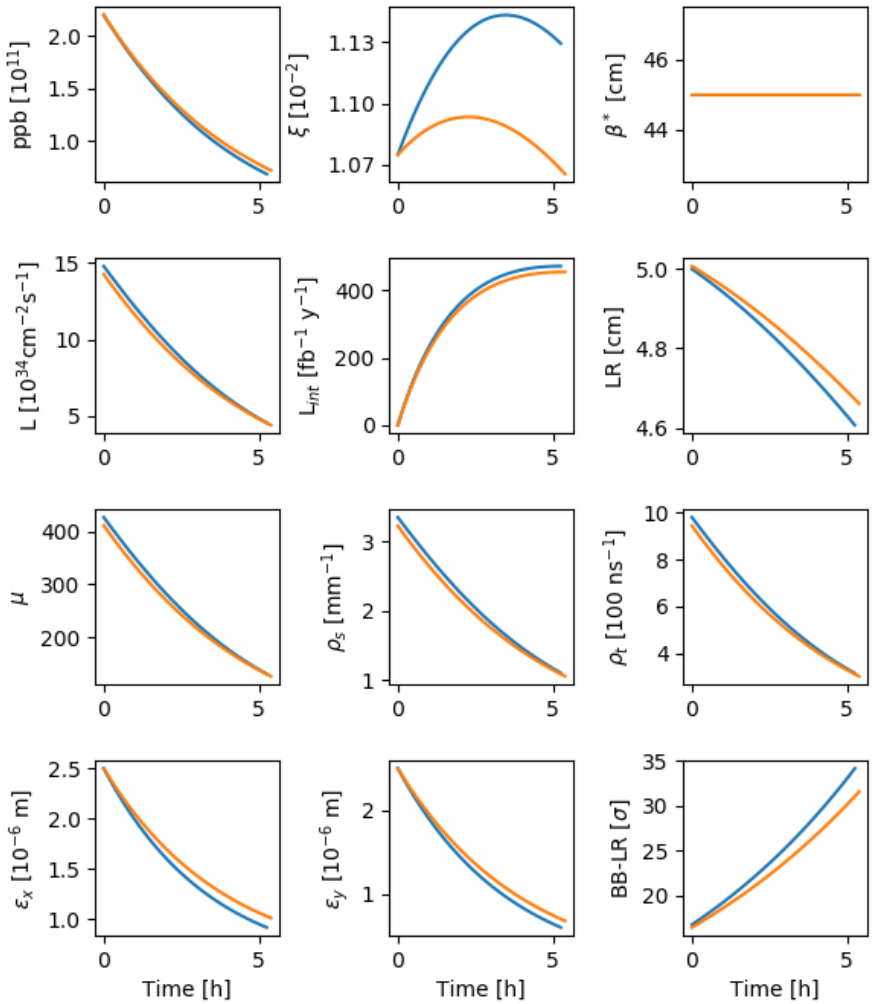

FIGURE 8.1: Baseline performance of the HE-LHC at 27 TeV (blue line) and 26 TeV (orange line) collision energy. LR refers to the luminous region and BB-LR to the beam-beam long-range separation.

protons. The instantaneous luminosity as well as the pile-up reach their minimum of $4.7 \times 10^{34}\,\mathrm{cm}^{-2}\mathrm{s}^{-1}$ or $4.4 \times 10^{34}\,\mathrm{cm}^{-2}\mathrm{s}^{-1}$ and 130 for both energies respectively. At this stage about 1.1 collisions per mm, and about 315 to 330, depending on the energy, collisions per ns take place. Moreover the luminous region (LR) decreases from 5.0 cm to 4.6 cm or 4.7 cm. The beam-beam long range (BB-LR) increases from about $16\,\sigma$ to about $34\,\sigma$ or $31\,\sigma$ for the two energies. After one year of operation, assuming 160 days of physics with a turn around time of 5 h and an availabilty of 75 % the integrated luminosity reaches about $470\,\mathrm{fb}^{-1}$ or $455\,\mathrm{fb}^{-1}$ assuming 27 TeV or 26 TeV centre of mass energy.

The maximum of the beam-beam parameter ξ_{bb} is about 1.09×10^{-2} or 1.14×10^{-2} for 27 TeV or 26 TeV centre of mass energy per interaction point. At both energies the beam-beam tune shift is in the order of the assumed acceptable limit of 1.00×10^{-2}

to 1.5×10^{-2} per interaction point [87, 88, 89]. Nevertheless, one possible attempt to mitigate this effect is choosing a suitable levelling technique.

To summarise the two baseline options of 27 TeV and 26 TeV centre of mass energy, all discussed performance parameters increase for higher energy. Therefore about 7 % higher instantaneous luminosity and a 3 % higher integrated luminosity is reached while colliding at 27 TeV centre of mass energy.

Parameter	Unit	27 TeV		26 TeV	
		I	F	I	F
$\mathcal{L}$	$10^{34}\mathrm{cm}^{-2}\mathrm{s}^{-1}$	15	4.7	14	4.4
$\mathcal{L}_{int}$	$\mathrm{fb}^{-1}\mathrm{y}^{-1}$	–	470	–	455
ppb	10^{11}	2.2	0.69	2.2	0.72
β^*	cm	45	45	45	45
LR	cm	5.0	4.6	5.0	4.7
BB-LR	σ	16.795	34.127	16.485	31.542
μ	–	430	130	410	130
ϱ_s	mm^{-1}	3.35	1.10	3.23	1.05
ϱ_t	$100\,\mathrm{ns}^{-1}$	980	315	945	300
ϵ_x	µm	2.5	0.9	2.5	1.0
ϵ_y	µm	2.5	0.6	2.5	0.7
$\xi_{bb,max}$	10^{-2}	1.14		1.09	
t_{fill}	h	5.25		5.39	

TABLE 8.1: Initial (I) and final (F) performance parameters of the HE-LHC base line (BL) at 27 TeV and 26 TeV.

8.2 β^* Levelling

To boost the performance the option of β^* levelling is discussed for 27 TeV centre of mass energy with a minimum β^* of 25 cm. This minimum β^* is used in the previous HE-LHC baseline [26, 90] and is therefore assumed feasible.

The luminosity is kept constant at three different scenarios, namely at $\mathcal{L} = 20 \times 10^{34}\,\mathrm{cm}^{-2}\mathrm{s}^{-1}$ (blue line), $\mathcal{L} = 15 \times 10^{34}\,\mathrm{cm}^{-2}\mathrm{s}^{-1}$ (orange line) and $\mathcal{L} = 10 \times 10^{34}\,\mathrm{cm}^{-2}\mathrm{s}^{-1}$ (green line). This goal is reached by stepwise reduction of β^* which is described in Chapter 2. A levelling step of 2 % is assumed. This means that if the initial luminosity has decayed by 2 % β^* is reduced in order to shift the luminostiy to the initial value, until the minimum β^* is reached. Figure 8.2 shows the physics fill for these luminosity levelling scenarios. All initial and final values of the studied parameters are summarised in Table 8.2.

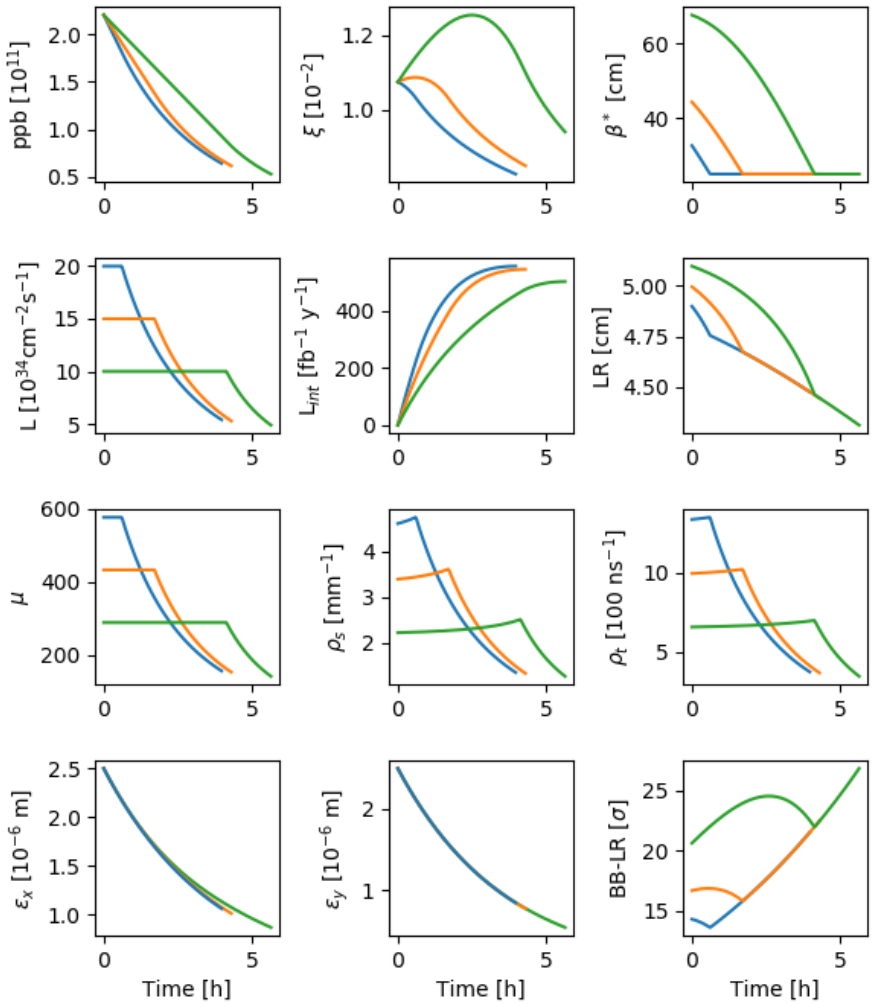

FIGURE 8.2: Performance while levelling the luminosity at 20×10^{34} (blue line), 15×10^{34} (orange line) and 10×10^{34} (green line) considering a levelling of 2% with a minimum β^* of 25 cm.

The initial proton bunch population is 2.2×10^{11} in every scenario. During the levelling process the decay of the ppb shows a linear instead of an exponential behaviour as seen in Figure 8.2. After the levelling time this linear behaviour becomes exponential as the protons burn off without reduction of β^*. The lower the levelling time is the fewer protons remain in one bunch before the beam gets dumped.

To level at a smaller instantaneous luminosity a higher initial β^* is required in order to not exceed this luminosity target. After every levelling step the beam is squeezed. This is achieved by reducing β^* until the smallest beta function at the collision point is reached. In these scenarios this limit is assumed to be 25 cm which is kept constant after the levelling time.

Although the instantaneous luminosity is levelled as a figure of merit in the simulations, the pile-up is levelled as well through the strong correlation between these parameters (see equation (3.41)). Performing collisions while using a levelling scheme, where the instantaneous luminosity is constant 575, 430 or 290 collisions occur in order of decreasing levelled instantaneous luminosity. Regarding the pile-up densities a slight growth is visible before the levelling time is reached. At this point, where β^* has its minimum the pile-up density peak is located in every scenario. Afterwards, the pile-up and the pile-up densities decay.

The BB-LR is chosen in order to keep the crossing angle constant. When the minimum β^* is reached, the BB-LR increases monotonously. In case of levelling to a constant luminosity of $\mathcal{L} = 20 \times 10^{34}\,\mathrm{cm}^{-2}\mathrm{s}^{-1}$ and $\mathcal{L} = 15 \times 10^{34}\,\mathrm{cm}^{-2}\mathrm{s}^{-1}$ the BB-LR is smaller than $16.795\,\sigma$ which is below the limit of about $16.8\,\sigma$ at 27 TeV collision energy with β^* of 45 cm [91].

Moreover the levelling process has an impact on the integrated luminosity. On one hand, operation at a lower levelled instantaneous luminosity leads to an increased levelling time and therefore the number of events stays constant for a longer period, which is beneficial for detection and analysis. On the other hand, a lower levelled instantaneous luminosity decreases the integrated luminosity. This means that the number of events per year is lower with respect to a scenario with higher targeted instantaneous luminosity. The integrated luminosity per year is 555 fb^{-1}, 545 fb^{-1} or 500 fb^{-1} in order of decreasing levelled luminosity.

Parameter	Unit	$\mathcal{L} = 20$		$\mathcal{L} = 15$		$\mathcal{L} = 10$	
		I	F	I	F	I	F
$\mathcal{L}$	$10^{34}\mathrm{cm}^{-2}\mathrm{s}^{-1}$	20	5.39	15	5.29	10	4.88
$\mathcal{L}_{int}$	$\mathrm{fb}^{-1}\mathrm{y}^{-1}$	–	555	–	545	–	500
ppb	10^{11}	2.2	0.64	2.2	0.61	2.2	0.53
β^*	cm	33	25	44	25	68	25
LR	cm	4.9	4.8	5.0	4.4	5.1	4.3
BB-LR	σ	14.31	13.64	16.68	22.47	20.61	26.80
μ	–	575	155	430	150	290	140
ϱ_s	mm^{-1}	4.62	1.35	3.40	1.33	2.23	1.27
ϱ_t	$100\,\mathrm{ns}^{-1}$	1330	375	995	370	660	350
ϵ_x	µm	2.5	1.1	2.5	1.0	2.5	0.9
ϵ_y	µm	2.5	0.8	2.5	0.8	2.5	0.5
$\xi_{bb,max}$	10^{-2}	1.07		1.09		1.25	
t_{lev}	h	0.60		1.70		4.14	
t_{fill}	h	3.98		4.31		5.65	

TABLE 8.2: Initial (I) and final (F) performance parameters of the HE-LHC levelled scenarios at 27 TeV with a minimum β^* of 25 cm. The levelled instantaneous luminosity is 20, 15 or 10 $\times 10^{34}\,\mathrm{cm}^{-2}\mathrm{s}^{-1}$.

The emittance decreases mostly as a function of time, as intrabeam scattering effects are negligible, which is already discussed in Chapter 5. Depending on the fill time the final horizontal (vertical) emittance is about 1.1 µm (0.8 µm), 1.0 µm (0.8 µm) or 0.9 µm (0.5 µm) for 3.98 h, 4.31 h or 5.65 h fill times. The fill time increases with decreasing levelled instanteneous luminosity. Therefore a scenario with a levelled instanteneous luminosity of $10 \times 10^{34}\,\mathrm{cm}^{-2}\mathrm{s}^{-1}$ has the longest fill time.

If levelling to an instantaneous luminosity of $20 \times 10^{34}\,\mathrm{cm}^{-2}\mathrm{s}^{-1}$ the beam-beam parameter decreases continuously as the protons burn off faster compared to the other levelling options. In case of the other two levelling options, the beam-beam parameter increases. The maximum tune shift is 1.07×10^{-2}, 1.09×10^{-2} or 1.25×10^{-2} in order of decreasing levelled instantaneous luminosity.

8.2.1 Dependence on Levelling Step

Until now β^* is reduced if the instanteneous luminosity has decreased by 2 %. Nevertheless the impact of the levelling percentage has to be studied as well. For this, a scenario with levelled instanteneous luminosity at $10 \times 10^{34}\,\mathrm{cm}^{-2}\mathrm{s}^{-1}$ is taken as an example. While reducing the levelling stepsize from 10 % to 1 %, the number of levelling steps increases significantly, which leads to operation with a tremendous

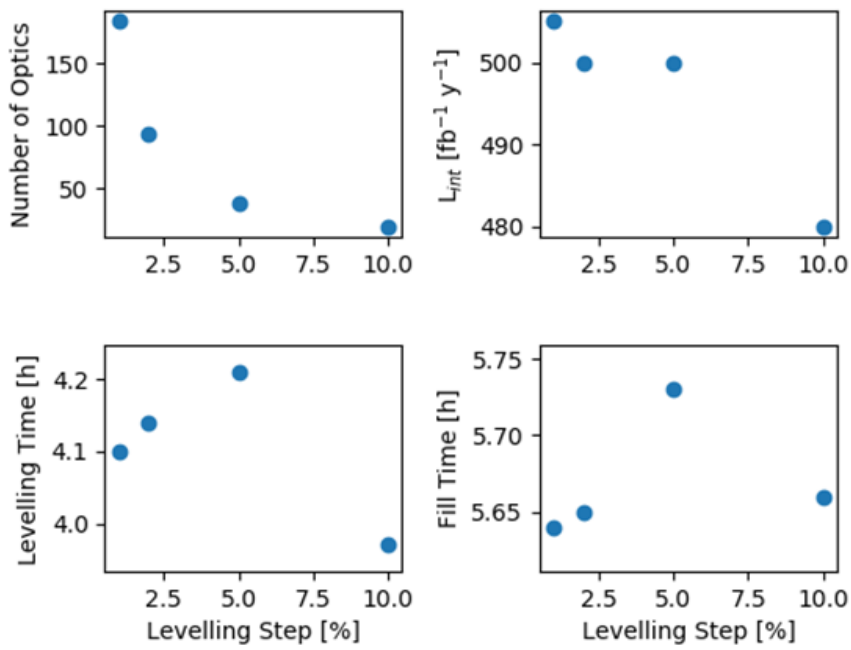

FIGURE 8.3: Impact of luminosity steps from on performance from 1 % to 10 % on integrated luminosity, number of optics, fill and levelling time while levelling the instantaneous luminosity to $\mathcal{L} = 10 \times 10^{34}\,\mathrm{cm}^{-2}\mathrm{s}^{-1}$ with a minimum β^* of 25 cm.

amount of different β^* and therefore required optics [92], which is shown in Figure 8.3 and summarised in Table 8.3.

The number of optics required for operation with a 1 % step is 10 times higher compared to operating with 10 % levelling. Regarding a levelling of 10 % the reached integrated luminosity is 480 $\mathrm{fb}^{-1}\mathrm{y}^{-1}$ which is 20 to 25 $\mathrm{fb}^{-1}\mathrm{y}^{-1}$ lower with respect to all other levelling options. Even though smaller levelling steps have a positive impact of the integrated luminosity, the number of required optics increases dramatically. One goal of levelling is to keep the pile-up constant over a long time. A levelling of 5 % results in the longest levelling time of 4.21 h, whereas a significant shorter levelling time of 3.97 h is achieved using 10 % levelling.

Regarding the levelling steps a trade off between the number of required optics, the levelling time and the reached integrated luminosity has to be made. Accurate and efficient commissioning of about 100 optics is a great challenge [92]. A levelling step between 2 % and 5 % seems to provide a good balance between integrated luminosity and number of required optics.

Parameter	Unit	10 %	5 %	2 %	1 %
Number of Optics	–	19	38	93	184
Levelling Time	h	3.97	4.21	4.14	4.10
Filling Time	h	5.66	5.73	5.65	5.64
Integrated Luminosity	$\mathrm{fb}^{-1}\mathrm{y}^{-1}$	480	500	500	505

TABLE 8.3: Impact of levelling steps on performance aspects.

8.2.2 Dependence on Penalty Step

The time required to change the optics, which is necessary while performing β^* levelling, is assumed to be 0 s. In simulations performed for the HL-LHC [82], it is

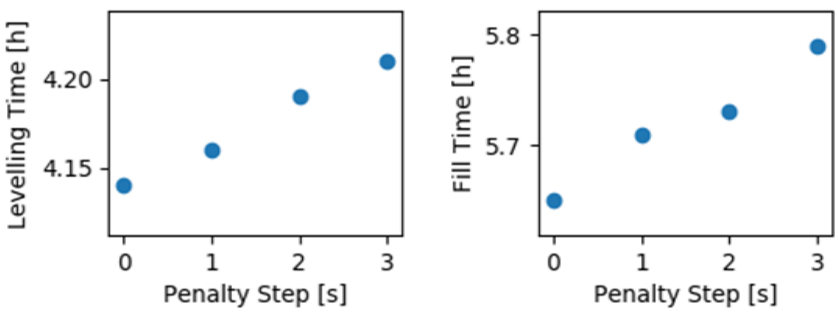

FIGURE 8.4: Impact of penalty steps of 0 s to 3 s on fill and levelling time while levelling the instantaneous luminosity to $10 \times 10^{34}\ \mathrm{cm}^{-2}\mathrm{s}^{-1}$ with a minimum β^* of 25 cm.

assumed that changing from one optics to another lasts 3 s. This is simualted by a penalty step, where the instantaneous luminosity is set to 0. The effects of 0 s to 3 s long penalty steps for the HE-LHC are discussed in this section. For these simulations the instantaneous luminosity is levelled to $10 \times 10^{34}\,\mathrm{cm}^{-2}\mathrm{s}^{-1}$ using a levelling step of 2 %. The results are summarised in Table 8.4 and shown in Figure 8.4.

The time in levelling and the fill time increase with increasing penalty step. A penalty step of up to 3 s has a negligible impact on the integrated luminosity. This means, assuming a pessimistic penalty step of 3 s does not have great impact on the HE-LHC performance.

Parameter	Unit	0 s	1 s	2 s	3 s
Levelling Time	h	4.14	4.16	4.19	4.21
Filling Time	h	5.65	5.71	5.73	5.79
Integrated Luminosity	$\mathrm{fb}^{-1}\mathrm{y}^{-1}$	500	499	496	494

TABLE 8.4: Impact of penalty steps on performance parameters.

8.3 β^* Levelling using ATS

Using the ATS scheme [93], β^* can be reduced by a factor 4. This means, that the initial β^* of 45 cm is assumed to be squeezed to 15 cm. Combining an ATS scheme with levelling is studied in this section with minimum β^* of 15 cm. The crossing angle and the longitudinal bunch size are kept constant at 330 µrad and 7.55 cm respectively. A luminosity levelling to $\mathcal{L} = 20 \times 10^{34}\,\mathrm{cm}^{-2}\mathrm{s}^{-1}$ (blue line), $\mathcal{L} = 15 \times 10^{34}\,\mathrm{cm}^{-2}\mathrm{s}^{-1}$ (orange line) and $\mathcal{L} = 10 \times 10^{34}\,\mathrm{cm}^{-2}\mathrm{s}^{-1}$ (green line) are studied. All results are shown in Figure 8.5 and summarised in Table 8.5.

The initial proton bunch population of 2.2×10^{11} decays to about 0.57×10^{11}, 0.52×10^{11} or 0.42×10^{11} in decreasing levelled luminosity order. The horizontal (vertical) emittance decays from 2.5 µm (2.5 µm) to about 1.1 µm (1.0 µm), 1.0 µm (0.8 µm) or 0.8 µm (0.5 µm) for 3.47 h 4.11 h or 5.82 h fill times.

Assuming a minimum β^* of 15 cm (instead of 25 cm) has negligible impact on the pile-up and the pile-up densities, which decrease with decreasing levelled luminosity. Moreover the behaviours of these parameters remain unchanged. In addition, the initial β^* is identical for the two minimum β^*.

The beam-beam long range is only above $16.8\,\sigma$ in case of a levelling to an instantaneous luminosity of $10 \times 10^{34}\,\mathrm{cm}^{-2}\mathrm{s}^{-1}$. In case of the other two levelling options,

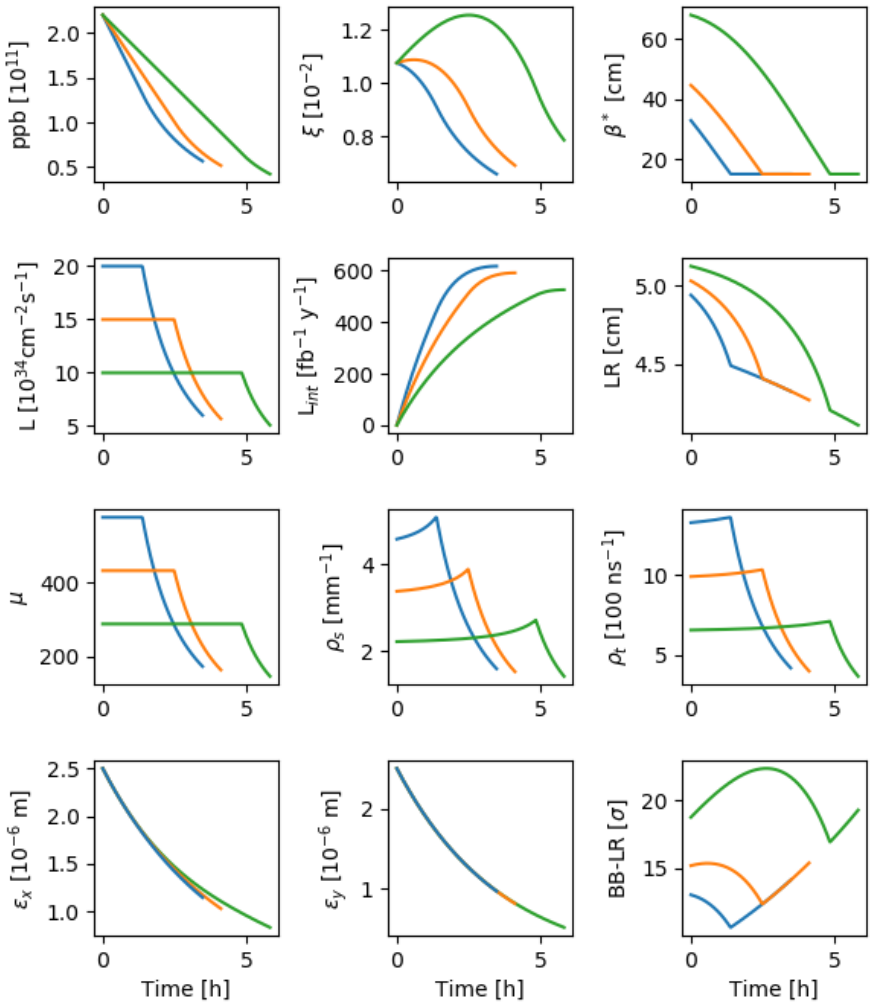

FIGURE 8.5: Performance while levelling the luminosity at 20×10^{34} (blue line), 15×10^{34} (orange line) and 10×10^{34} (green line) considering a levelling step of 2% using ATS scheme with a minimum β^* of 15 cm.

this beam-beam long range is smaller. At the smallest levelled luminosity the beam-beam tune shift is the greatest compared to the other levelling options. The maximum of the beam-beam parameter is 1.07×10^{-2}, 1.09×10^{-2} or 1.25×10^{-2} in order of decreasing levelled instantaneous luminosity.

Levelling up to $\beta^* = 15$ cm results in a larger integrated luminosity compared to the baseline or to levelling with a minimum β^* of 25 cm. With respect to results achieved using a minimum β^* of 25 cm the integrated luminosity is 12 %, 8 % or 5 % higher in order of decreasing instantaneous luminosity. Due to the smaller β^* the time in levelling increases by 127 %, 45 % or 17 % respectively. Even though all levelling times increase for smaller minimum β^*, the fill time increase only while levelling at 10×10^{34} cm^{-2}s^{-1}. In the other two levelling options a smaller fill time

is observed.

Parameter	Unit	$\mathcal{L} = 20$		$\mathcal{L} = 15$		$\mathcal{L} = 10$	
		I	F	I	F	I	F
$\mathcal{L}$	$10^{34}\mathrm{cm}^{-2}\mathrm{s}^{-1}$	20	6.01	15	5.69	10	5.1
$\mathcal{L}_{int}$	$\mathrm{fb}^{-1}\mathrm{y}^{-1}$	–	620	–	590	–	525
ppb	10^{11}	2.2	0.57	2.2	0.52	2.2	0.42
β^*	cm	33	15	45	15	68	15
LR	cm	4.9	4.3	5.0	4.3	5.1	4.1
BB-LR	σ	13.05	14.14	15.20	15.40	18.78	19.30
μ	–	575	173	435	165	290	145
ϱ_s	mm^{-1}	4.59	1.59	3.38	1.52	2.22	1.41
ϱ_t	$100\,\mathrm{ns}^{-1}$	1325	420	990	400	655	370
ϵ_x	µm	2.5	1.1	2.5	1.0	2.5	0.8
ϵ_y	µm	2.5	1.0	2.5	0.8	2.5	0.5
$\xi_{bb,max}$	10^{-2}	1.07		1.09		1.25	
t_{lev}	h	1.36		2.48		4.83	
t_{fill}	h	3.47		4.11		5.82	

TABLE 8.5: Initial (I) and final (F) performance parameters of the HE-LHC levelled scenarios at 27 TeV with a minimum β^* of 15 cm. The levelled instantaneous luminosity is 20, 15 or 10 $\times 10^{34}$ $\mathrm{cm}^{-2}\mathrm{s}^{-1}$.

8.4 Constant Divergence

In these simulations the divergerce $\sigma_{z'}$, which is the ratio between the normalised emittance ϵ_n and the beta function at the interaction point β^* described through

$$\sigma_{z'} = \sqrt{\frac{\epsilon_n}{\beta^*}} = \sqrt{\frac{\epsilon}{\gamma_{rel}\,\beta_{rel}\,\beta^*}} \tag{8.1}$$

is kept constant, with the relativistic Lorentz factors γ_{rel} and β_{rel}. z is a place holder for x and y, the transverse coordinates. The crossing angle χ is constant at 330 µrad. From

$$\text{BB-LR} = \frac{\chi}{\sigma_{z'}} \tag{8.2}$$

follows that the beam-beam long range (BB-LR) is constant as well if the crossing angle and the divergence are constant. The results are shown in Figure 8.6 and summarised in Table 8.6.

The instantaneous luminosity increases slightly until the maximum is reached after 0.61 h or 0.33 h for the 27 TeV and the 26 TeV option respectively. At the end of the fill the instantaneous luminosity has decayed to $5.8 \times 10^{34}\,\mathrm{cm}^{-2}\mathrm{s}^{-1}$ and

5.5×10^{34} cm^{-2}s^{-1}. The pile-up shows an identical behaviour like the instantaneous luminosity. The number of events decreases from 425 to 166 at 27 TeV and from 410 to 160 at 26 TeV. The peak of the pile-up is located at the exact time as the peak of the instantaneous luminosity, where the pile-up reaches 435 and 415 respectively. During operation at 27 TeV about 3.35 collisions per mm and about 980 collisions per ns occur at the start of the fill. The peak values of the pile-up densities are 3.48 collisions per mm and 1010 collisions per ns. In case of colliding at 26 TeV initially 3.22 collisions per mm and 945 collisions per ns take place. At its maximum the pile-up densities reach 3.27 collisions per mm and 955 collisions per ns at 26 TeV

β^* is computed in order to compensate for the decreased normalised emittance. Therefore these two parameters show an identical behaviour. The initial β^* decreases from 45 cm to about 13 cm. The horizontal and vertical emittances decay

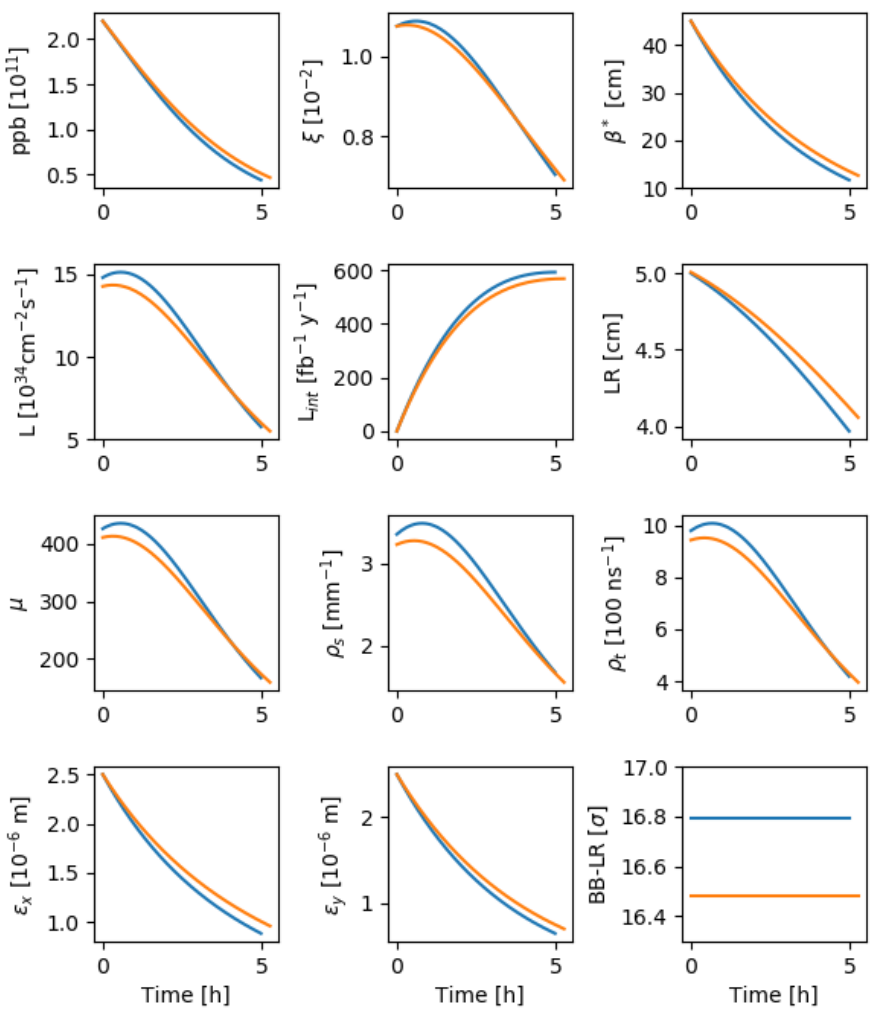

FIGURE 8.6: HE-LHC performance during constant divergence at 27 TeV (blue line) and 26 TeV (orange line) collision energy.

from initial 2.5 µm in both planes to about 1.0 µm horizontally and to about 0.7 µm vertically. Using an ATS scheme a minimum β^* of about 15 cm seems feasible, which is about 2 cm higher than the minimum β^* reached in these simulations. Improved simulations need to be investigated in order to not undercut this limit. The number of required optics at 27 TeV and 26 TeV collision energy is 160 and 155 respectively and accurate commissioning of over 100 optics is a great challenge. In case of 27 TeV collision energy with a fill time of 4.99 h and 160 different β^*, one can conclude that the optics needs to be changed every 2 minutes. One attempt to reduce the number of optics is to operate using the same optics longer, which then leads to a non-constant divergence which effects the beam-beam long range separation.

The beam-beam parameter does not increase significantly over the filll. It does not exceed 1.1×10^{-2} per interaction point and is therefore in the order of the maximal acceptable beam-beam tune shift of 1.0×10^{-2} to 1.5×10^{-2} per interaction point.

One major advantage of this performance technique is the possibility of higher integrated luminosity while keeping the crossing angle and the beam-beam long range separation constant. With respect to the baseline scenarios the integrated luminosity is increased by 25 % for both collision energies. Further studies to increase the integrated luminosity are currently ongoing. For example, the performance can be improved by reducing the β^* twice as fast as in the results presented in this thesis.

Parameter	Unit	27 TeV		26 TeV	
		I	F	I	F
$\mathcal{L}$	$10^{34}\mathrm{cm}^{-2}\mathrm{s}^{-1}$	15	5.8	14	5.5
$\mathcal{L}_{int}$	$\mathrm{fb}^{-1}\mathrm{y}^{-1}$	–	590	–	570
ppb	10^{11}	2.2	0.44	2.2	0.46
β^*	cm	45	12	45	13
LR	cm	5.0	4.0	5.0	4.1
BB-LR	σ	16.795	16.795	16.485	16.485
μ	–	425	166	410	160
ϱ_s	mm^{-1}	3.35	1.69	3.22	1.56
ϱ_t	$100\,\mathrm{ns}^{-1}$	980	420	945	395
ϵ_x	µm	2.5	0.9	2.5	1.0
ϵ_y	µm	2.5	0.6	2.5	0.7
$\xi_{bb,max}$	10^{-2}	1.09		1.08	
t_{fill}	h	4.99		5.27	

TABLE 8.6: Initial (I) and final (F) performance parameters for constant divergence at 27 TeV and 26 TeV.

Chapter 9

Conclusion

Great effort is put into exploring the merits of the HE-LHC, a possible successor of the HL-LHC. Various arc cell and dispersion suppressor options are studied in order to best meet the following requirements:

- A minimum beam stay clear of $10\,\sigma$ must be reached over the ring.
- The offset between the LHC and the HE-LHC must be kept as small as possible.
- 27 TeV centre of mass energy is targeted for collision energy.

In order to generate various lattice options fast and easy, a lot of work is put into the development of ALGEA. This tool enables a HE-LHC lattice generation for both beams while taking into account constrainst like minimum inter-element distances, positions of the interaction points, naming and powering conventions. Using the survey fitting algorithm of ALGEA the geometry offset to the LHC is minimised. Studying different arc cell and dispersion suppressor options has led to conclude on two HE-LHC baseline lattices, namely 18 and 23 cells per arc designs using the LHC dispersion suppressor, with a maximal offset to the LHC of about 9 cm and about 1 cm respectively. The offset peak is located in the first regular arc cell which is part of the dispersion suppressor. In the baseline lattices, all FODO cells are matched to 90° phase advance in both transverse planes.

Injecting in the HE-LHC from the SPS with 450 GeV limits the aperture to $7.51\,\sigma$ or $8.78\,\sigma$ in a regular FODO cell respectively for the 18 and the 23 cells option. The bottleneck in both options, however is found to be in the dispersion suppressor as there the optics functions are, in general, greater compared to the arc.

Different approaches to meet the target of $10\,\sigma$ at 450 GeV by applying additional quadrupole fields in the arc dipoles have been tested. It has been found that a phase advances of $\mu_x = 0.257 \times 2\pi$, $\mu_y = 0.238 \times 2\pi$ or $\mu_x = 0.207 \times 2\pi$, $\mu_y = 0.241 \times 2\pi$ per FODO cell enlarge the beam stay clear by $0.15\,\sigma$ or $0.23\,\sigma$ for the 18 or 23 cells design. Before concluding on new phase advances however, the whole ring needs to be matched and analysed. Combined function dipoles, which provide an additional quadrupole field of about ± 450 b_2 units lead to sufficient beam stay clear.

However such magnet design is challenging and studies to confirm the feasibility are required. The beam stay clear inceases with higher injection energy. An injection energy of 600 GeV could be achieved by a small SPS upgrade, which results in a sufficient HE-LHC beam stay clear for the 23x90 lattice. In case of the 18x90 lattice about 800 GeV injection energy are required to reach the target of $10\,\sigma$ beam stay clear.

Even though the 23x90 design is the most similar to the 23x90 LHC lattice, it comes along with the disadvantage of only reaching 26 TeV centre of mass energy. This implies a loss of 1 TeV with respect to the target energy of 27 TeV which can be achieved using the 18x90 design. With present quadrupole errors in the arc dipoles of $\pm 46.84 \times 10^{-4}$ the energy reach is reduced to 25.9 TeV in case of the 23 cells per arc design. In order to avoid reducing the centre of mass energy below 26 TeV these errors must not be greater than $\pm 27 \times 10^{-4}$. Regarding the 18 cells per arc design the quadrupoles in the FODO cells can be enlarged without shortening the dipoles due to additional drift spaces in the cell. As a result the current quadrupole errors in the dipoles do not have any impact on the energy reach for the 18x90 design.

With the current baseline parameters and a constant β^* of 45 cm an instantaneous luminosity of 15×10^{34} cm^{-2}s^{-1} or 14×10^{34} cm^{-2}s^{-1} is achieved assuming a centre of mass energy of 27 TeV or 26 TeV. The inital pile-up then results in about 430 or 410 events respectively for the two designs. After one year of operation the integrated luminosity results in about 470 fb^{-1}, respectively 455 fb^{-1}.

First estimates on alternative scenarios are studied, where a β^* levelling is considered with minimum of the beta function is assumed at 25 cm or 15 cm, if an achromatic telescopic squeezing technique is used simultaneously with the levelling. A levelling at 10×10^{34} cm^{-2}s^{-1} keeps the pile-up at a constant level for the time while not changing the performance parameters dramatically compared to the baseline. A levelling of 5 % seems to be a reasonable trade off between the integrated luminosity of 500 fb^{-1}y^{-1} and 38 required optics. The most promising scenario however, is operating at a constant beam divergence at the interaction point, where the crossing angle and the beam-beam long range separation remain constant, while squeezing β^*. This leads to an integrated luminosity of 590 fb^{-1} or 570 fb^{-1} per year for 27 TeV or 26 TeV collision energy, which is about 25% more compared to the baseline scenarios. This can be improved further by, for example, reducing the β^* 2 times faster.

The work presented in this thesis highlights the realisation possibility of the HE-LHC. Optimisations in order to overcome various weak points are summarised. To conclude, the HE-LHC is a feasible possible successor of the HL-LHC, operating at an unprecedented energy frontier.

Appendix A

Interaction Region Optics

As the focus of this thesis is on the arcs the optics of the interaction regions are summarised in the appendix for beam 1 and beam 2. The arc optics in combination with the right dispersion suppression scheme are essential for the optics in the IRs. All IR optics are taken from the matched 23x90 HE-LHC design. In this optics the new HE-LHC IR design is integrated in IR1, IR3, IR5 and IR6. All other IR designs are taken from the LHC.

Interaction Regions 1 and 5

The main IRs are designed for the HE-LHC [94] and integrated in the lattice. As the beta function at the interaction point is different for injection and collision the optics changes as well. Therefore, only these IRs need different matching for injection and collision.

Injection

A β^* of 11 m is targeted at the interaction point [94]. The dispersion peak in beam 2 results in an aperture bottleneck and needs to be optimised.

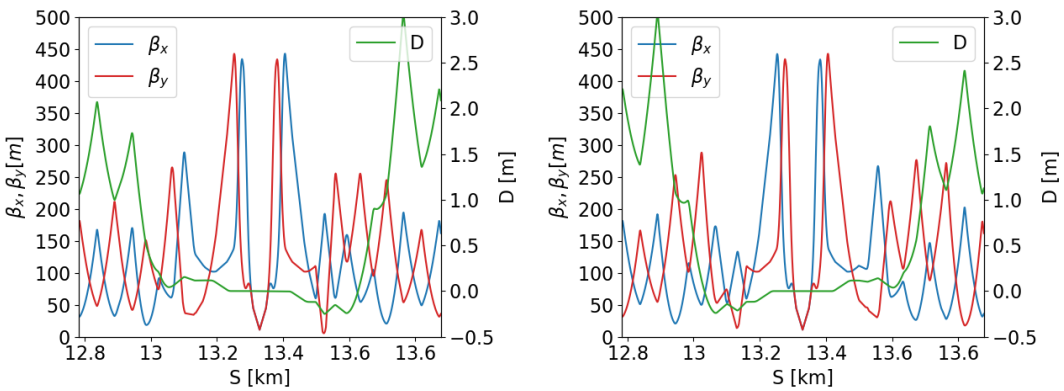

(A) Beam 1 (B) Beam 2

FIGURE A.1: Main experiments optics at injection energy of 450 GeV.

Collision

At collision energy, which is in case of the 23x90 design 26 TeV, the beta function at the IP is 45 cm. In order to reach a β^* that small, the beta function in the final focus triplet is blown up to several km [94]. The *final focus triplet* are the three quadrupoles nearest to the IP.

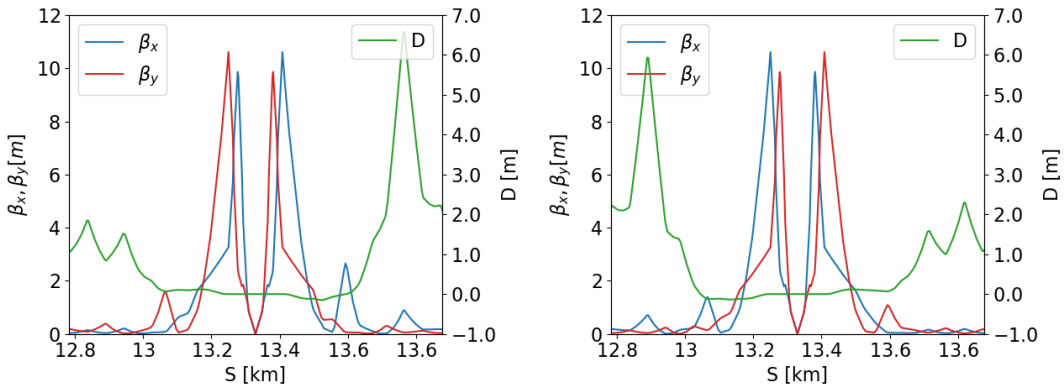

(A) Beam 1 (B) Beam 2

FIGURE A.2: Main experiments optics for beam 1 (left) and beam 2 (right) at collision energy of 26 TeV.

Interaction Region 2

The LHC optics is integrated [95]. Beam 1 is injected clockwise.

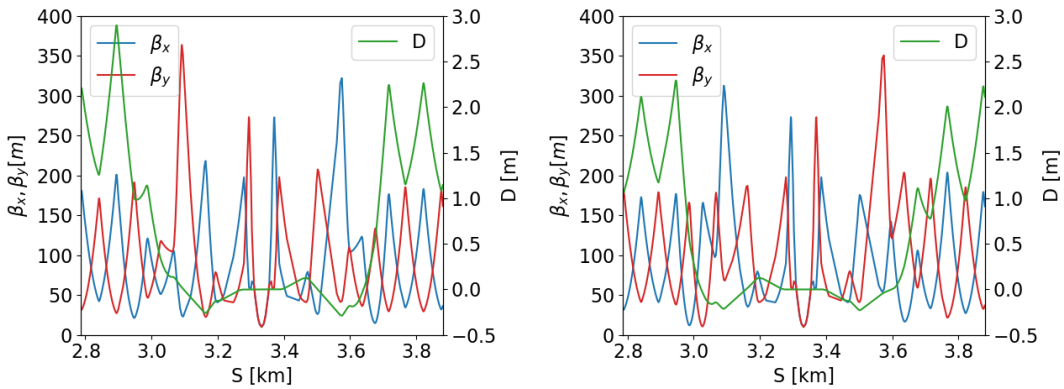

(A) Beam 1 (B) Beam 2

FIGURE A.3: Integrated interaction region 2 optics from LHC for beam 1 (left) and beam 2 (right).

Interaction Region 3

The LHC optics is integrated [95]. Currently a redesign of IR3 is ongoing to fit the HE-LHC requirements [75].

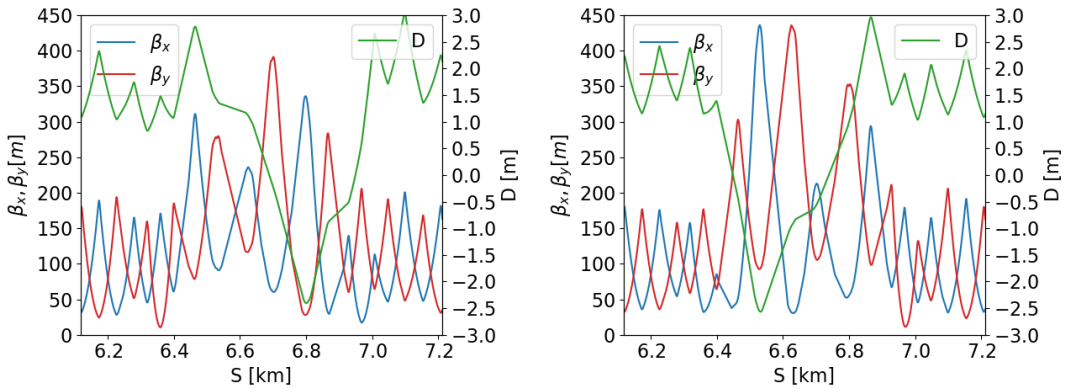

(A) Beam 1 (B) Beam 2

FIGURE A.4: Integrated interaction region 3 optics from LHC for beam 1 (left) and beam 2 (right).

Interaction Region 4

Compared to the LHC, this design introduces an additional quadrupole on either side of the RF region [96]. This IR can compensate for tune mismatches and is therefore designed more flexible compared to other IRs.

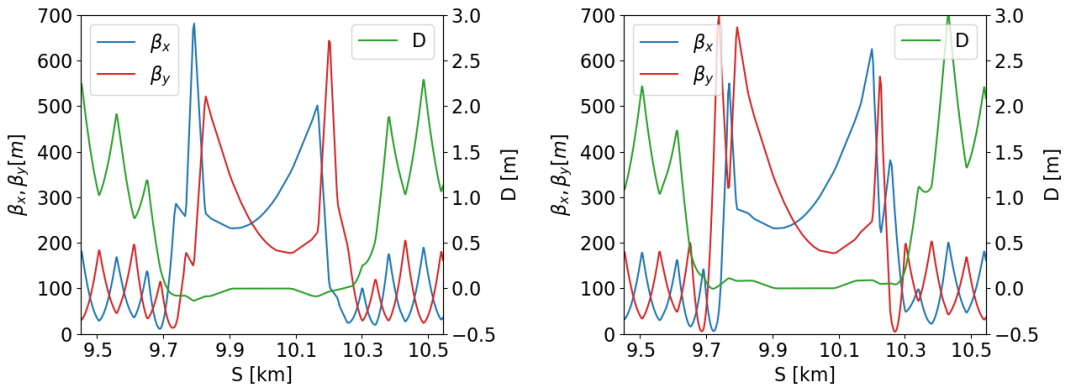

(A) Beam 1 (B) Beam 2

FIGURE A.5: HE-LHC optics of the RF interaction region for beam 1 (left) and beam 2 (right).

Interaction Region 6

In general IR6 is difficult to match as only four quadrupoles are located in between the dispersion suppressors [97]. Additionally, a dispersion in the order of 20 cm to 30 cm is required [97]. This constraint is not yet fulfilled for beam 2 and therefore further development is ongoing.

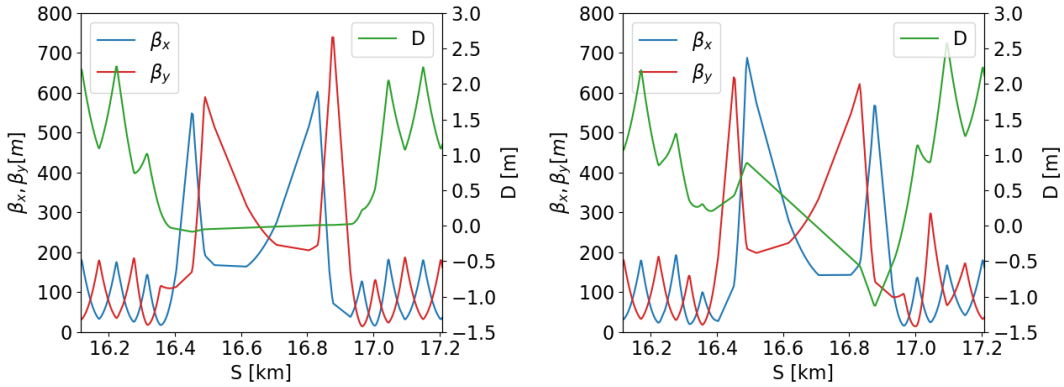

(A) Beam 1 (B) Beam 2

FIGURE A.6: Beam dump for beam 1 (left) and beam 2 (right).

Interaction Region 7

The LHC optics is integrated [95]. Currently, investigations are put into an appropriate design of IR7 [75, 98]. The current beam separation is 280 mm, which is 30 cm more compared to the arc.

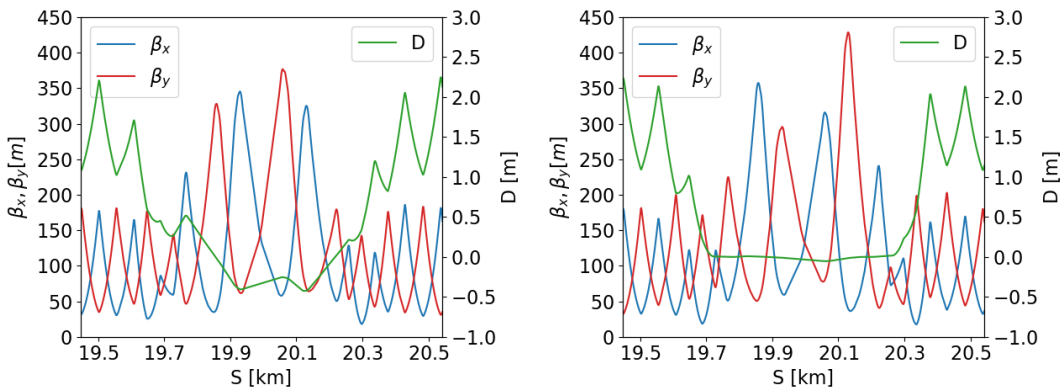

(A) Beam 1 (B) Beam 2

FIGURE A.7: Integrated interaction region 7 optics from LHC for beam 1 (left) and beam 2 (right).

Interaction Region 8

The LHC optics is integrated [95]. Beam 2 is injected counter clockwise.

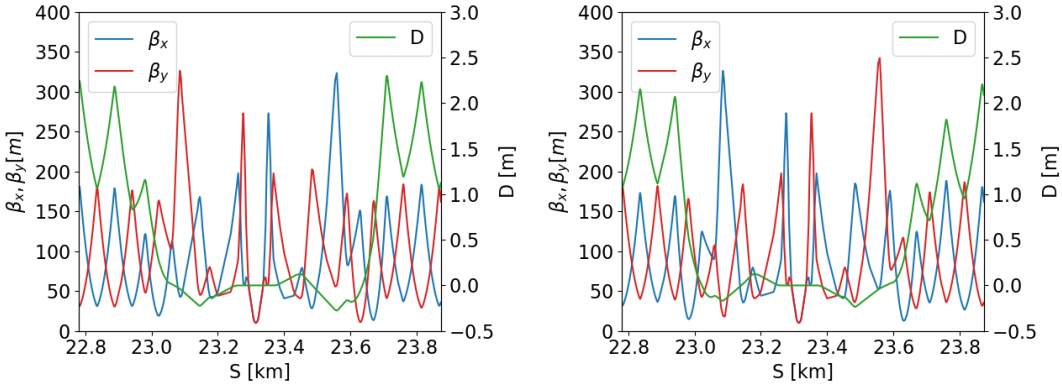

(A) Beam 1 (B) Beam 2

FIGURE A.8: Integrated LHC interaction region 8 for beam 1 (left) and beam 2 (right).

List of Figures

2.1 CERN complex and accelerator chain . . . 3
2.2 Schematic drawing of the HE-LHC and FCC . . . 4
2.3 Schematic layout of the FCC-hh . . . 5

3.1 Transverse coordinate system for linear optics . . . 8
3.2 Visualisation of an ideal dipole and a quadrupole field . . . 9
3.3 Emittance . . . 14
3.4 Design orbit, closed orbit and betatron oscillation. . . . 15
3.5 Illustration of the RF voltage . . . 17
3.6 Synchronous particle before and after transition energy . . . 18
3.7 Illustration of the luminous region of two colliding bunches . . . 20
3.8 Schematic plot of crossing beams . . . 21
3.9 Example of levelled instantaneous luminosity and pile-up . . . 22
3.10 Two colliding bunches with crab cavities . . . 24
3.11 Adiabtic damping . . . 24
3.12 Achromatic telescopic squeezing . . . 25
3.13 Beam screen 2018 . . . 26
3.14 Beam screen misalignment tolerances . . . 26
3.15 Schematic plot of a FODO cell . . . 27
3.16 LHC ring layout . . . 29
3.17 LHC FODO cell . . . 30
3.18 Schematic plot of the LHC dispersion suppressor . . . 32
3.19 Survey of the ring . . . 34

4.1 Schematic plot of the HE-LHC DS1 . . . 40
4.2 Schematic plot of the HE-LHC DS2 . . . 41
4.3 Schematic plot of the HE-LHC DS3 . . . 41
4.4 Illustration of the parameters for survey fitting . . . 42
4.5 Survey fitting . . . 43
4.6 Sequence output of ALGEA . . . 44

5.1 Aperture dependence on cell length . . . 46
5.2 Transverse offset of six lattices . . . 48
5.3 Transverse offset of the 18x90 and 23x90 lattice . . . 49
5.4 Beam stay clear along a FODO cell . . . 52
5.5 Beam stay clear dependence on energy . . . 53

6.1 Optics functions and aperture for beam 1 and 2 for 18x90 design 55
6.2 Optics functions and aperture for beam 1 and 2 for 23x90 design 56
6.3 Aperture dependence on phase advance 58
6.4 Example of combined function dipoles in two FODO cells 60
6.5 Aperture results for combined function dipoles 61

7.1 Effect of quadrupole errors in the arc dipoles 66

8.1 Baseline performance 70
8.2 Levelling performance 72
8.3 Impact of luminosity steps 74
8.4 Impact of penalty steps 75
8.5 Levelling performance using ATS 77
8.6 Performace at constant divergence 79

A.1 Main experiments optics at injection energy 83
A.2 Main experiments optics at collision energy 84
A.3 Optics for interaction region 2 84
A.4 Optics for interaction region 3 85
A.5 Optics of the RF interaction region 4 85
A.6 Beam dump optics in interaction region 6 86
A.7 Optics for interaction region 7 86
A.8 Optics for interaction region 8 87

List of Tables

2.1 FCC-hh, HE-LHC, HL-LHC and LHC key parameters at collision energy 6

3.1 LHC cell design parameters 32
3.2 LHC ring design parameters 33
3.3 Input parameters for aperture calculation 35

4.1 Location of interaction points for the HE-LHC 37
4.2 Required drift spaces between elements 38
4.3 Beam separation 38

5.1 Arc cell options, 18 - 23 cells 45
5.2 Arc cell options, 24 - 32 cells 46
5.3 HE-LHC cell parameters for the 18x90 and the 23x90 lattice 50
5.4 HE-LHC ring parameters for the 18x90 and the 23x90 lattice 51
5.5 Beam parameters 52

6.1 Minimum aperture in the dispersion suppressors 57
6.2 Phase advances and aperture for resonance free lattices 59
6.3 Resulting aperture when using combined function dipoles 61
6.4 Resulting aperture by varying the phase advance using combined function dipoles 63

7.1 Required quadrupole gradient with present quadrupole errors 67
7.2 Parameters before and after correction of quadrupole errors 68

8.1 Performance parameters baseline scenarios 71
8.2 Performance parameters using levelling with minimum β^* of 25 cm . . 73
8.3 Impact of levelling steps 75
8.4 Impact of penalty steps 76
8.5 Performance parameters using levelling with minimum β^* of 15 cm . . 78
8.6 Performance parameters with constant divergence 80

Bibliography

[1] CERN. *LHC*. URL: http://lhcathome.web.cern.ch/ (Accessed July 18, 2018).

[2] CERN. URL: https://home.cern/ (Accessed June 13, 2018).

[3] CERN. *HL-LHC*. URL: http://hilumilhc.web.cern.ch/ (Accessed July 18, 2018).

[4] CERN. *Compact Linear Collider Study*. URL: http://clic-study.web.cern.ch/ (Accessed June 13, 2018).

[5] L. LINSSEN et al. *Physics and Detectors at CLIC: CLIC Conceptual Design Report*. arXiv:1202.5940. CERN-2012-003. ANL-HEP-TR-12-01. DESY-12-008. KEK-Report-2011-7 (2012). URL: http://cds.cern.ch/record/1425915.

[6] CERN. *Future Circular Collider Study*. URL: https://fcc.web.cern.ch/Pages/default.aspx (Accessed June 13, 2018).

[7] M. BENEDIKT. *Future Circular Collider Study - Status and Plans*. Presented at FCC Week 2018, Amsterdam. URL: https://indico.cern.ch/event/656491/contributions/2932205/attachments/1628761/2595133/180409_FCC-Amsterdam_Statuspresentation_V2.pdf.

[8] O. BRÜNING et al. *High Energy LHC Document prepared for the European HEP Strategy Update*. CERN-ATS-2012-237 (2012). URL: https://cds.cern.ch/record/1471002.

[9] Y. CAI et al. *HE-LHC Optics Development*. ICFA Beam Dyn. Newsl. **72**. 141-151 (2017). URL: https://cds.cern.ch/record/2315726.

[10] G. APOLLINARI et al. *High-Luminosity Large Hadron Collider (HL-LHC): Technical Design Report V.0.1*. CERN Yellow Reports: Monographs (2017). URL: http://cds.cern.ch/record/2284929.

[11] A. J. ATSMA. *Algea*. URL: http://www.theoi.com/Daimon/Algea.html (Accessed June 13, 2018).

[12] CERN. *LHC Complex*. URL: https://wic.web.cern.ch/content/lhc-complex (Accessed July 18, 2018).

[13] CERN. *The 300 GeV programme*. (1972). URL: https://cds.cern.ch/record/104068.

[14] CERN. *Restarting the LHC: Why 13 Tev?* URL: https://home.cern/about/engineering/restarting-lhc-why-13-tev (Accessed Aug. 16, 2018).

[15] KEK. *SUPERKEKB*. URL: http://www-superkekb.kek.jp/ (Accessed July 18, 2018).

[16] KEK. *High Energy Accelerator Research Organisation*. URL: https://www.kek.jp/en/ (Accessed July 18, 2018).

[17] KEK. *Letter of Intent for KEK Super B Factory Part III: Accelerator Design*. KEK Report 2004-4 (2004). URL: http://www-superkekb.kek.jp/documents/LoI_accelerator.pdf.

[18] UNIVERSITY OF LIVERPOOL. *It's the Universe but not as we know it: Future Circular Collider Week*. URL: https://www.liverpool.ac.uk/physics/news/stories/title,955047,en.html (Accessed June 19, 2018).

[19] CERN. *LEP Design Report (1984)*. URL: https://cds.cern.ch/record/102083.

[20] O. BRÜNING et al. *LHC Design Report*. CERN Yellow Reports: Monographs (2004). URL: https://cds.cern.ch/record/782076.

[21] R. MARTIN et al. *Interaction Region Design driven by Energy Deposition*. Physical Review Accelerator and Beams **20**. DOI: 10.1103/PhysRevAccelBeams.20.081005 (2017). URL: https://link.aps.org/doi/10.1103/PhysRevAccelBeams.20.081005.

[22] F. BURKART et al. *Conceptual Design Considerations for the 50 TeV FCC Beam Dump Insertion*. Proceedings of IPAC (2016). CERN-ACC-2016-232. TUPMR047. URL: https://cds.cern.ch/record/2207393.

[23] J. MOLSON et al. *Simulation of the FCC-hh Collimation System*. Proceedings of IPAC (2016). TUPMR054. URL: https://cds.cern.ch/record/2304772.

[24] J. MOLSON et al. *Status of the FCC-hh Collimation System*. Proceedings of IPAC (2017). CERN-ACC-2017-109. MOPAB001. URL: https://cds.cern.ch/record/2289720.

[25] A. CHANCÉ et al. *Updates on the Optics of the Future Hadron-Hadron Collider FCC-hh*. CERN-ACC-2017-0055, TUPVA002. 4 (2017). URL: https://cds.cern.ch/record/2281130.

[26] F. ZIMMERMANN. *HE-LHC CDR* (2018). Unpublised.

[27] F. BORDRY. *CERN Hadron Colliders*. Presented by F. Zimmermann at the 31st HE-LHC Design meeting. URL: https://indico.cern.ch/event/739469/contributions/3052466/attachments/1675225/2689288/180627-Performance_CERN-hadron-colliders-ISC11-MBE-FZI.pdf.

[28] E. METRAL et al. *Update of the HL-LHC Operational Scenarios for Proton Operation*. CERN-ACC-NOTE-2018-0002 (2018). URL: https://cds.cern.ch/record/2301292.

[29] O. BRÜNING et al. *Future Circular Collider Study FCC-he BaselineParameters*. CERN-ACC-2017-0019 (2017). URL: https://cds.cern.ch/record/2260408.

[30] S. TURNER. *CAS - CERN Accelerator School : 5th Advanced Accelerator Physics Course*. CERN-95-06 (1995). URL: https://cds.cern.ch/record/254747.

[31] S. RUSSENSCHUCK. *Design of Accelerator Magnets (2005)*. URL: https://cds.cern.ch/record/865932.

[32] D. W. KERST. *Acceleration of Electrons by Magnetic Induction*. Physical Review **58**. DOI: 10.1103/PhysRev.58.841 (1940). URL: https://link.aps.org/doi/10.1103/PhysRev.58.841.

[33] S.Y. LEE. *Accelerator Physics*. Third Edition. World Scientific (2012).

[34] M. SCHENK et al. *MD2190: Q" Stabilization During Injection*. CERN-ACC-NOTE-2018-0003 (2018). URL: https://cds.cern.ch/record/2302465.

[35] E. D. COURANT, H. S. SNYDER. *Theory of the Alternating-Gradient Synchrotron*. Annals of Physics **3**, 1 (1958).

[36] E. HAMISH MACLEAN. *Modelling and Correction of the Non-Linear Transverse Dynamics of the LHC from Beam-Based Measurements*. CERN-THESIS-2014-135 (2014). PhD thesis. URL: https://cds.cern.ch/record/1951379.

[37] S. R. MANE et al. *Spin-Polarized Charged Particle Beams in High-Energy Accelerators*. Reports on Progress in Physics **68** (2005). URL: http://stacks.iop.org/0034-4885/68/i=9/a=R01.

[38] R. CALAGA et al. *Alternative Working Point(s) for the LHC*. CERN-ATS-2011-148 (2011). URL: https://cds.cern.ch/record/1382056.

[39] E.M. MCMILLAN. *The Synchrotron–A Proposed High Energy Particle Accelerator*. Physical Review **68**, 143 (1945).

[40] V.I. VEKSLER. *A new Method of Accelerating Relativistic Particles*. Comptes Rendus (Dokaldy) de l'Academie Sciences de l'URSS **43**, 329-331, (1944).

[41] A. HUSCHAUER et al. *Working Point and Resonance Studies at the CERN Proton Synchrotron*. CERN-THESIS-2012-212 (2012). Master thesis. URL: https://cds.cern.ch/record/1501943.

[42] W. HERR et al. *Concept of Luminosity (2006)*. URL: https://cds.cern.ch/record/941318.

[43] R. CALAGA. *Crab Cavities for the LHC Upgrade*. Chamonix 2012 Workshop on LHC Performance, 363-372 (2012). URL: https://cds.cern.ch/record/1493034.

[44] L. E. MEDINA MEDRANO et al. *Effective Pile-Up Density as a Measure of the Experimental Data Quality for High-Luminosity LHC Operational Scenarios*. CERN-ACC-2018-0003 (2018). URL: https://cds.cern.ch/record/2301928.

[45] A. PIWINSKI. *Intra-Beam-Scattering*. Proceedings of the 9th International Conference on High Energy Accelerators Stanford, USA (1974). URL: https://cds.cern.ch/record/400720.

[46] A. WOLSKI. *Space Charge, Intrabeam Scattering and Touschek Effects*. URL: http://uspas.fnal.gov/materials/12MSU/DampingRings-Lecture6.pdf (Accessed June 11, 2018).

[47] J.D. BJORKEN, S.K. MTINGWA. *Intrabeam Scattering*. Particel Accelerators **13**. FERMILAB-PUB-82-47-THY (1982). URL: https://cds.cern.ch/record/140304.

[48] W. HERR. *Luminosity and Beam-Beam Effects in the LHC*. (2000). URL: https://cds.cern.ch/record/487337.

[49] J. P. KOUTCHOUK. *Luminosity Optimization and Leveling*. Proceedings of Chamonix Workshop 324 - 347 (2010). URL: https://espace.cern.ch/acc-tec-sector/Chamonix/Chamx2010/papers/JPK_9_04.pdf.

[50] M. SOLFAROLI CAMILLOCCI. *LHC Nominal Cycle (2016)*. URL: https://cds.cern.ch/record/2294513.

[51] KEK. *KEK-B*. URL: https://www.kek.jp/en/Research/IPNS/Belle/ (Accessed June 18, 2018).

[52] K. HOSOYAMA et al. *Development of the KEK-B Superconducting Crab Cavity*. (2008). URL: https://accelconf.web.cern.ch/accelconf/e08/papers/thxm02.pdf.

[53] F. ZIMMERMANN. *CERN System of Accelerators*. Presented at CAS 2007, Pisa. URL: https://ab-dep-abp-frankz-lectures.web.cern.ch/ab-dep-abp-frankz-lectures/Pisa/lecture2-Pisa.pdf (Accessed July 17, 2018).

[54] S. FARTOUKH. *An Achromatic Telescopic Squeezing (ATS) Scheme for the LHC Upgrade*. URL: https://cds.cern.ch/record/1382077.

[55] J.B. JEANNERET et al. *Geometrical Aperture in LHC at Injection*. LHC-Project-Note-66 (1996). URL: https://cds.cern.ch/record/692065.

[56] R. KERSEVAN. *New Beam Screen Design Proposal*. Presented at FCC-hh General Design Meeting, Mar. 2018. URL: https://indico.cern.ch/event/715957/contributions/2943304/attachments/1621496/2580644/FCC-hh_Meeting_22Mar2018_.pdf.

[57] H. GROTE et al. *The MAD-X Program*. CERN (2015). URL: http://mad.web.cern.ch/mad/releases/5.02.05/madxuguide.pdf.

[58] CERN. *Sixtrack*. URL: http://sixtrack.web.cern.ch/SixTrack/ (Accessed June 13, 2018).

[59] B.J. HOLZER. *Beam Optics and Lattice Design for Particle Accelerators*. arXiv:1303.6514 (2013). URL: https://cds.cern.ch/record/1533020.

[60] CERN. *ATLAS*. URL: https://atlas.cern/ (Accessed June 14, 2018).

[61] CERN. *ALICE*. URL: http://aliceinfo.cern.ch/ (Accessed June 14, 2018).

[62] CERN. *CMS*. URL: https://cms.web.cern.ch/ (Accessed June 14, 2018).

[63] CERN. *LHCb*. URL: lhcb.cern.ch/ (Accessed June 14, 2018).

[64] CERN. *LHC Optics Web: LHC Run I Protons Optics*. URL: http://abpdata.web.cern.ch/abpdata/lhc_optics_web/www/pprun1/ (Accessed July 17, 2018).

[65] O. BRÜNING et al. *Field Quality Specification for the LHC Main Dipole Magnets*. CERN-LHC-Project-Report-501 (2001). URL: https://cds.cern.ch/record/522049.

[66] S. IZQUIERDO BERMUDEZ. *Private communication*. Nov. 2017.

[67] CERN. *MAD-X*. URL: http://mad.web.cern.ch/mad/ (Accessed June 18, 2018).

[68] L. V. RIESEN-HAUPT. *Private communication*. May 2018.

[69] R. BRUCE. *Private communication*. May 2018.

[70] J. KEINTZEL. *Arc cell options for the HE-LHC*. (2018). URL: https://cds.cern.ch/record/2624282.

[71] D. SCHÖRLING. *Other Magnet Parameters*. Presented at FCC Week 2018, Amsterdam. URL: https://indico.cern.ch/event/656491/contributions/2920305/attachments/1628231/2596868/Schoerling_OtherMagnets_2018.pdf.

[72] K. ARTOOS et al. *Transport and Installation of Cryo-Magnets in CERN's Large Hadron Collider Tunnel*. CERN-TS-2004-013 (2004). URL: https://cds.cern.ch/record/1069103.

[73] V. MERTENS. *Private communication*. Mar. 2018.

[74] R. BRUCE et al. *Parameters for Aperture Calculations at Injection for HL-LHC*. CERN-ACC-2016-0328 (2016). URL: https://cds.cern.ch/record/2237427.

[75] T. RISSELADA. *Private communication*. July 2018.

[76] S. FARTOUKH. *The Right Optics Concept for the Right Dimension of the High Luminosity LHC Project*. ICFA Beam Dyn.Newsl. **71** 116-135 (2016), CERN-ACC-2016-0085. URL: https://cds.cern.ch/record/2161774.

[77] A. VERDIER. *Resonance Free Lattices for A.G. Machines*. CERN-SL-99-018-AP (1999). URL: https://cds.cern.ch/record/387152.

[78] F. SCHMIDT et al. *Correction of the Systematic b3 Error with the Resonance-Free Lattice in the LHC*. CERN-LHC-Project-Report-401 (2000). URL: https://cds.cern.ch/record/462631.

[79] F. SCHMIDT et al. *Optimisation of the LHC Dynamic Aperture via the Phase Advance of the Arc Cells*. CERN-LHC-Project-Report-297 (1999). URL: https://cds.cern.ch/record/386688.

[80] M. HOFER et al. *Integrated HE-LHC Optics and its Performance*. Proceedings of IPAC (2018). URL: http://ipac2018.vrws.de/papers/mopmk002.pdf.

[81] J. P. BURNET et al. *Fifty years of the CERN Proton Synchrotron: Volume 1*. CERN Yellow Reports: Monographs (2011). URL: https://cds.cern.ch/record/1359959.

[82] L. MEDINA MEDRANO et al. *Performance and Operational Aspects of HL-LHC Scenarios*. CERN-ACC-2016-240, TUPMW035 (2016). URL: https://cds.cern.ch/record/2207385.

[83] L. MEDINA MEDRANO et al. *Studies on Luminous Region, Pile-Up and Performance for HL-LHC Scenarios*. CERN-ACC-2017-135, TUPIK089 (2017). URL: https://cds.cern.ch/record/2289694.

[84] L. MEDINA MEDRANO et al. *Assessment of the Performance of High Luminosity LHC Operational Scenarios: Integrated Luminosity and Effective Pile-Up density*. Canadian Journal of Physics **0**. DOI: 10.1139/cjp-2018-0291 (2018). URL: https://doi.org/10.1139/cjp-2018-0291.

[85] R. TOMÁS et al. *HL-LHC Alternatives*. Proceedings of RLIUP: Review of LHC and Injector Upgrade Plans (2013). URL: https://cds.cern.ch/record/1977364.

[86] Y. SUN et al. *Beam Dynamics aspects of Crab Cavities in the CERN Large Hadron Collider*. Physical Review Accelerator and Beams **12**, 101002 (2009). URL: https://cds.cern.ch/record/1216155.

[87] T. PIELONI et al. *Colliding High Brightness Beams in the LHC*. MOP250. Proceedings of HB Beijing, China (2012). URL: https://accelconf.web.cern.ch/accelconf/HB2012/papers/mop250.pdf.

[88] X. BUFFAT et al. *Probing the Behaviour of High Brightness Bunches in Collision at 6.5 TeV and the Interplay with an External Source of Noise (MD1433)*. CERN-ACC-NOTE-2017-0030 (2017). URL: https://cds.cern.ch/record/2261037.

[89] S. FURUSETH. *Head-On Beam-Beam Interactions in High-Energy Hadron Colliders. GPU-Powered Modelling of Nonlinear Effects*. Master Thesis. CERN-THESIS-2017-279 (2017). URL: https://cds.cern.ch/record/2299580.

[90] CERN. *CERN repository: //afs/cern.ch/eng/lhc/optics/HELHC/V0.2*. Nov. 2017.

[91] C. TAMBASCO. *Update HE-LHC Beam-Beam Studies*. Presented at HE-LHC General Design Meeting, Jul. 2018. URL: https://indico.cern.ch/event/747676/contributions/3092210/attachments/1695642/2731315/HELHC_31_july_2018.pdf.

[92] F. CARLIER. *Optics Measurements and Correction Challenges for the HL-LHC*. CERN-ACC-2017-0088 (2017). URL: https://cds.cern.ch/record/2290899.

[93] S. FARTOUKH. *Achromatic Telescopic Squeezing Scheme and Application to the LHC and its Luminosity Upgrade*. Physical Review Accelerator and Beams **16**. DOI: 10.1103/PhysRevSTAB.16.111002 (2013). URL: https://link.aps.org/doi/10.1103/PhysRevSTAB.16.111002.

[94] L. v. Riesen-Haupt et al. *Experimental Interaction Region Optics for the High Energy LHC*. Proceedings of IPAC (2018). URL: http://ipac2018.vrws.de/papers/mopmk006.pdf.

[95] CERN. *LHC Optics Web Home*. URL: cern.ch/lhcoptics (Accessed July 05, 2018).

[96] P. Martinez Mirave et al. *Optics for RF Acceleration Section for the High Energy Large Hadron Collider*. Proceedings of IPAC (2018). URL: http://ipac2018.vrws.de/papers/mopmk001.pdf.

[97] W. Bartmann. *Private communication*. Jan. 2018.

[98] M. Crouch. *Private communication*. July 2018.